

**STRUCTURAL AND MECHANISTIC INSIGHTS INTO REGULATION  
OF RGS17 AND PLC $\epsilon$**

by

**Monita Sieng**

**A Dissertation**

*Submitted to the Faculty of Purdue University*

*In Partial Fulfillment of the Requirements for the degree of*

**Doctor of Philosophy**



Department of Chemistry

West Lafayette, Indiana

August 2019

**THE PURDUE UNIVERSITY GRADUATE SCHOOL**  
**STATEMENT OF COMMITTEE APPROVAL**

Dr. Angeline M. Lyon, Chair

Department of Chemistry and Biological Sciences

Dr. Chittaranjan Das

Department of Chemistry

Dr. Nicholas Noinaj

Department of Biological Sciences

Dr. Mathew Tantama

Department of Chemistry

**Approved by:**

Dr. Christine Hrycyna

Head of the Graduate Program

*To the Sieng Dynasty*

## ACKNOWLEDGMENTS

First and foremost, I would like to thank my advisor Dr. Angeline M. Lyon for being the best mentor I could ever ask for. Thank you for allowing me to join your lab and supporting me throughout my graduate school career. With your guidance, I was able to grow as a student, scientist, and individual. I would also like to thank my committee members, Dr. Nicholas Noinaj, Dr. Chittaranjan Das, and Dr. Mathew Tantama for all their advice and support.

Secondly, I would like to thank the members of the Lyon Lab. I am extremely fortunate to be able to spend my years in graduate school alongside such an amazing and supporting group of people. Thanks to you all, I was able to get through graduate school in a comfortable and encouraging environment. I will miss all our lab happy hours, celebrations, and birthday cookie cakes!

I would also like to thank all the friends I have made in graduate school, Brianna, Elissia, Mavreen, Moises, Saadia, and Yan. Moving away from home for the first time was definitely difficult, but you guys made it a wonderful experience! Thanks for being my second family! I would especially like to thank my roommate Saadia. I will miss spending every Sunday cooking, drinking wine, and having long meaningful talks about life with you!

Finally, I would like to thank the Sieng Dynasty and my boyfriend, Michael Le, for their unwavering love and support. Thank you for always picking up my Facebook/Skype calls and taking the time to visit me on countless occasions. I would not be where I am today without all of you and I am eternally grateful! Being away from you all was the hardest obstacle I had to face in graduate school, but you guys taught me that distance is just a test of how far love can travel. Thank you again, this one is for you!

## TABLE OF CONTENTS

LIST OF TABLES .....	8
LIST OF FIGURES .....	9
LIST OF ABBREVIATIONS.....	11
ABSTRACT.....	14
CHAPTER 1. INTRODUCTION .....	15
1.1 Regulator of G Protein Signaling Proteins.....	16
1.2 Regulator of G Protein Signaling 17.....	19
1.2.1 Inhibition of RGS17 .....	19
1.2.2 Regulation of RGS17.....	20
1.3 Phospholipase C.....	21
1.4 Phospholipase C $\epsilon$ .....	23
1.4.1 Regulation of PLC $\epsilon$ .....	24
1.5 References.....	26
CHAPTER 2. HIGH-RESOLUTION STRUCTURE OF RGS17 SUGGESTS A ROLE FOR CA <sup>2+</sup> IN PROMOTING THE GTPASE ACTIVATING PROTEIN ACTIVITY BY RZ SUBFAMILY MEMBERS.....	35
2.1 Abstract.....	35
2.2 Introduction.....	35
2.3 Results.....	37
2.3.1 Crystal Structure of RGS17 Bound to Calcium.....	37
2.3.2 RGS17 Binds Ca <sup>2+</sup> and Mg <sup>2+</sup> in Solution .....	42
2.3.3 RGS17 Has Higher Affinity for Ca <sup>2+</sup> than Mg <sup>2+</sup> .....	45
2.3.4 RGS17 Binds Cations with Higher Affinity than RGS4 or RGS2 .....	47
2.3.5 Calcium Enhances Interactions Between RGS17 and Activated G $\alpha_o$ .....	50
2.3.6 Ca <sup>2+</sup> Increases the GTPase Activity of RGS17. ....	52
2.3.7 Calcium Alters the Binding Mechanism Between RGS17 and Activated G $\alpha_o$ .....	53
2.4 Discussion.....	54
2.5 Experimental Procedures .....	57

2.5.1	RGS17 Expression and Purification .....	57
2.5.2	Crystallization of RGS17.....	58
2.5.3	Data Collection, Processing, and Refinement .....	59
2.5.4	Nuclear Magnetic Resonance .....	59
2.5.5	Differential Scanning Fluorimetry.....	60
2.5.6	AlphaScreen Method for the RGS17–Gα <sub>o</sub> Interaction .....	61
2.5.7	GTP Hydrolysis Assays.....	61
2.5.8	Isothermal Titration Calorimetry.....	62
2.6	Acknowledgments.....	62
2.7	Conflict of Interest .....	62
2.8	Author Contributions .....	63
2.9	References.....	63
CHAPTER 3. RAP1A ALLOSTERICALLY ACTIVATES PHOSPHOLIPASE C <sub>ε</sub> VIA ITS C-TERMINAL RA2 DOMAIN .....		68
3.1	Abstract.....	68
3.2	Introduction.....	68
3.3	Results.....	70
3.3.1	The Two RA Domains of PLC <sub>ε</sub> Have Different Roles in Stability and Basal Activity .....	70
3.3.2	Mutations on the RA2 Domain Surface Do Not Alter Activity or Stability .....	72
3.3.3	Residues on the Surface of RA2 Are Required for Rap1A-dependent Activation....	75
3.3.4	Mutation of the RA2 Domain Does Not Change the Affinity for Rap1A <sup>G12V</sup> ·GTP .	77
3.3.5	Rap1A <sup>G12V</sup> ·GTP Binding Induces Conformational Changes in PLC <sub>ε</sub> .....	79
3.4	Discussion.....	83
3.5	Experimental Procedures .....	86
3.5.1	Protein Expression, Purification, and Mutagenesis of PLC <sub>ε</sub> Variants .....	86
3.5.2	Expression and Purification of Rap1A <sup>G12V</sup> ·GTP.....	86
3.5.3	Differential Scanning Fluorimetry.....	87
3.5.4	PLC <sub>ε</sub> Basal Activity Assays .....	87
3.5.5	Rap1A <sup>G12V</sup> ·GTP-dependent Activation of PLC <sub>ε</sub> Variants .....	88
3.5.6	AlphaScreen Binding Assay .....	88

3.5.7	Formation and Isolation of the Rap1A <sup>G12V</sup> ·GTP-EF3-COOH Complex .....	89
3.5.8	SAXS Data Collection and Analysis .....	89
3.5.9	Statistical Methods.....	92
3.6	Acknowledgments.....	92
3.7	Conflict of Interest .....	92
3.8	Author Contributions .....	92
3.9	References.....	92
CHAPTER 4. CONCLUSIONS AND FUTURE PERSPECTIVES .....		97
4.1	Conclusions.....	97
4.1.1	Ca <sup>2+</sup> is a Positive Regulator of RGS17 .....	97
4.1.2	Rap1A Allosterically Regulates PLCε Activity .....	97
4.2	Future Perspectives .....	98
VITA.....		100
PUBLICATION.....		101

## LIST OF TABLES

Table 2.1 RGS17 Data Collection and Refinement Statistics.....	39
Table 2.2 Thermal Stability of RGS17 .....	45
Table 2.3. Steady-state Kinetic Parameters for RGS17 and RGS4 GTPase Activity.....	53
Table 3.1. Basal Activity and Melting Temperature ( $T_m$ ) of PLC $\epsilon$ Variants .....	72
Table 3.2. Rap1A-dependent Activity and IC <sub>50</sub> Values of PLC $\epsilon$ Variants.....	77
Table 3.3 SAXS Structural Parameters of PLC $\epsilon$ Variants.....	83
Table 3.4. SAXS Data Collection and Analysis Parameters .....	90

## LIST OF FIGURES

Figure 1.1. G protein-coupled receptor (GPCR) signaling mechanism.....	15
Figure 1.2. Regulator of G protein Signaling (RGS) mechanism.....	17
Figure 1.3. Domain architecture of RGS subfamilies.....	18
Figure 1.4. Phospholipase C (PLC) signaling mechanism .....	21
Figure 1.5. Domain architecture of PLC subfamilies .....	22
Figure 1.6. Regulation of PLC $\epsilon$ .....	25
Figure 2.1. Crystal structure of RGS17 in complex with Ca <sup>2+</sup> .....	38
Figure 2.2. Superposition of RGS17 and 1ZV4.....	40
Figure 2.3. The crystallographic RGS17 dimer coordinates four Ca <sup>2+</sup> ions.....	41
Figure 2.4. RGS17 binds Ca <sup>2+</sup> in solution .....	43
Figure 2.5. RGS17 binds Mg <sup>2+</sup> in solution .....	44
Figure 2.6. RGS17 is not significantly thermally stabilized by the addition of CaCl <sub>2</sub> or MgCl <sub>2</sub> . ..	45
Figure 2.7. RGS17 binds Ca <sup>2+</sup> with higher affinity than Mg <sup>2+</sup> .....	46
Figure 2.8. RGS4 binds Ca <sup>2+</sup> weakly but does not bind Mg <sup>2+</sup> .....	48
Figure 2.9. <sup>1</sup> H- <sup>15</sup> N spectra of RGS2 in the presence of CaCl <sub>2</sub> or MgCl <sub>2</sub> .....	49
Figure 2.10. CaCl <sub>2</sub> enhances the binding of activated G $\alpha_o$ by RGS17, but not RGS4 .....	51
Figure 2.11. Ca <sup>2+</sup> increases RGS17-stimulated GTP hydrolysis .....	52
Figure 2.12. ITC characterization of RGS17-G $\alpha_o$ in the absence (Left) and presence (Right) of saturating levels of Ca <sup>2+</sup> .....	54
Figure 2.13. Model of RGS17 bound to activated G $\alpha_i$ .....	57
Figure 3.1. The PLC $\epsilon$ RA domains have different roles in stability and basal activity.....	71
Figure 3.2. Mutation of conserved, hydrophobic residues on the RA2 domain do not alter activity or stability .....	74
Figure 3.3. Residues in the RA2 domain contribute to Rap1A-dependent activation.....	76

Figure 3.4. The PLC $\epsilon$ RA2 mutants are not defective in binding Rap1A <sup>G12V</sup> ·GTP.....	78
Figure 3.5. Characterization of PLC $\epsilon$ EF3-COOH.....	80
Figure 3.6. Rap1A <sup>G12V</sup> ·GTP induces conformational changes in PLC $\epsilon$ EF3-COOH .....	81
Figure 3.7. Model of by Rap1A-dependent activation of PLC $\epsilon$ .....	85
Figure 3.8. Representative UV, size exclusion chromatography (SEC)-SAXS scattering and integrated intensity and $R_g$ as a function of individual frames chromatograms for PLC $\epsilon$ EF3-COOH and the Rap1A <sup>G12V</sup> ·GTP–EF3-COOH complex .....	90

## LIST OF ABBREVIATIONS

ADP	Adenosine diphosphate
AH	Amphipathic helix
Ala (A)	Alanine
Asn (N)	Asparagine
ATP	Adenosine triphosphate
Ca <sup>2+</sup>	Calcium
cAMP	Cyclic adenosine monophosphate
CHAPS	3-[(3-cholamidopropyl)dimethylammonio]-1-propanesulfonate
CRE	cAMP response elements
CREB	cAMP response element-binding protein
CSP	Chemical shift perturbation
CTD	Distal C-terminal domain
DAG	Diacylglycerol
DEP	Disheveled/Eg110/pleckstrin domain
D <sub>max</sub>	Maximum interparticle distances
DSF	Differential scanning fluorimetry
DTT	Dithiothreitol
EDTA	Ethylenediaminetetraacetic acid
EGTA	Ethylene glycol-bis(β-aminoethyl ether)-N,N,N',N'-tetraacetic acid
Epac	Exchange protein directly activated by cAMP
GAP	GTPase activating protein
GDP	Guanosine diphosphate
GEF	Guanine exchange factor
GGL	G protein γ-like
Gln (D)	Glutamine
Glu (E)	Glutamic acid
Go Loco	Gα <sub>i/o</sub> loco
GPCR	G protein-coupled receptor

GRB2	Growth factor receptor-bound protein 2
GTP	Guanosine triphosphate
HEPES	4-(2-hydroxyethyl)-1-piperazineethanesulfonic acid
HSQC	Heteronuclear single quantum coherence
HTS	High throughput screening
IC <sub>50</sub>	Maximal Inhibitory concentration 50%
Ile (I)	Isoleucine
IP <sub>3</sub>	Inositol 1,4,5-triphosphate
IPTG	Isopropyl β-D-1-thiogalactopyranoside
ITC	Isothermal calorimetry
K <sub>D</sub>	Dissociation constant
Leu (L)	Leucine
Lys (K)	Lysine
mAKAP	muscle-specific A kinase anchoring protein
Mg <sup>2+</sup>	Magnesium
NMR	Nuclear magnetic resonance
NSD	Normal spatial discrepancy
OD	Optical density
pCys	Poly-cysteine string
PDZ	Psd-95/DlgA/ZO1 domain
PEG	Polyethylene glycol
PI <sub>4</sub> P	Phosphatidylinositol-4-phosphate
PIP <sub>2</sub>	Phosphatidylinositol 4,5-bisphosphate
PH	Pleckstrin homology
Phe (F)	Phenylalanine
PKC	Protein kinase C
PKD	Protein kinase D
PLC	Phospholipase C
ppm	Parts per million
PTB	Phosphotyrosine binding domain
RA	Ras association

RBD	Raf-like Ras binding domain
$R_g$	Radius of gyration
RGS	Regulator of G protein signaling
RH	RGS homology
r.m.s.d	Root mean square deviation
RTK	Receptor tyrosine kinase
SAXS	Small angle X-ray scattering
S.D.	Standard deviation
SEC	Size exclusion chromatography
S.E.M.	Standard error of the mean
Ser (S)	Serine
SH2/3	Src homology
SHC	Src homology and collagen
SOS	Son of sevenless
$T_m$	Melting temperature
Tyr (Y)	Tyrosine
Val (V)	Valine
$V_c$	Volume of correlation
$V_p$	Porod volume

## ABSTRACT

Author: Sieng, Monita. PhD

Institution: Purdue University

Degree Received: August 2019

Title: Structural and Mechanistic Insights into Regulation of RGS17 and PLC $\epsilon$

Committee Chair: Angeline M. Lyon

Recent advances in structural biology and biochemistry have identified proteins downstream of G protein-coupled receptors (GPCRs) as promising drug targets. These proteins are highly regulated to ensure proper physiological responses from extracellular stimuli. Dysregulation of these signaling enzymes can have detrimental consequences, including cardiovascular disease and cancer. Understanding how these proteins are regulated from a structural and biochemical standpoint can therefore be exploited to develop new therapeutics.

In this work, the molecular mechanism of regulation of two different proteins downstream of GPCRs is investigated. The first protein, Regulator of G Protein Signaling 17 (RGS17), is involved in numerous processes throughout the body, including the development and progression of lung cancer. This work presents the crystal structure of RGS17 bound to Ca<sup>2+</sup>. Ca<sup>2+</sup> was found to bind to the same site as the predicted G $\alpha$  binding surface and increases interactions between RGS17 and G $\alpha_o$ . Therefore, Ca<sup>2+</sup> positively regulates RGS17, supporting a mechanism in which Ca<sup>2+</sup> increases the GTPase activating function of the RZ-family of RGS proteins to ultimately downregulate Ca<sup>2+</sup> signaling.

The second protein, phospholipase C $\epsilon$  (PLC $\epsilon$ ), has been implicated in cardiac hypertrophy through its production of second messengers. This process is regulated by the small GTPase Rap1A. This work presents insight into the molecular mechanism of Rap1A-dependent activation of PLC $\epsilon$ , in which four conserved, hydrophobic residues on the surface of the RA2 domain of PLC $\epsilon$  play an essential role. Furthermore, small angle X-ray scattering studies show that binding of Rap1A induces conformational changes in PLC $\epsilon$ , resulting in a more compact activated complex. This supports a mechanism in which Rap1A is an allosteric activator of PLC $\epsilon$ , inducing conformational changes in PLC $\epsilon$  that increase lipid hydrolysis by relieving autoinhibitory interactions and/or by promoting interactions with the cell membrane.

## CHAPTER 1. INTRODUCTION

Signaling cascades mediated by G protein-coupled receptors (GPCRs) regulate a majority of physiological functions in the human body. GPCRs are made up of seven transmembrane helices and serve as cellular sensors that are classically activated by external stimuli to elicit specific physiological responses (1). The general signaling paradigm of GPCRs begins with an external stimulus, in the form of a ligand, binding to its cognate receptor (Figure 1.1) (1,2). Binding of the ligand stabilizes the receptor in an active conformation and allows the receptor to bind a heterotrimeric G protein (1,2). Heterotrimeric G proteins are GTPases made up of an  $\alpha$ ,  $\beta$ , and  $\gamma$  subunit that serve as molecular switches to turn on or off specific signaling pathways (2). In the inactive state, the  $G\alpha$  subunit is bound to GDP and interacts with  $G\beta\gamma$ , which is an obligate heterodimer (2). Activated GPCRs function as guanine exchange factors (GEF) for G proteins, facilitating the exchange of GDP for GTP on the  $G\alpha$  subunit, and resulting in the dissociation of  $G\alpha$  subunit from  $G\beta\gamma$  (1). Both the  $G\alpha$  and  $G\beta\gamma$  subunits interact with downstream effector enzymes to elicit intracellular responses to the external stimuli (1,2).

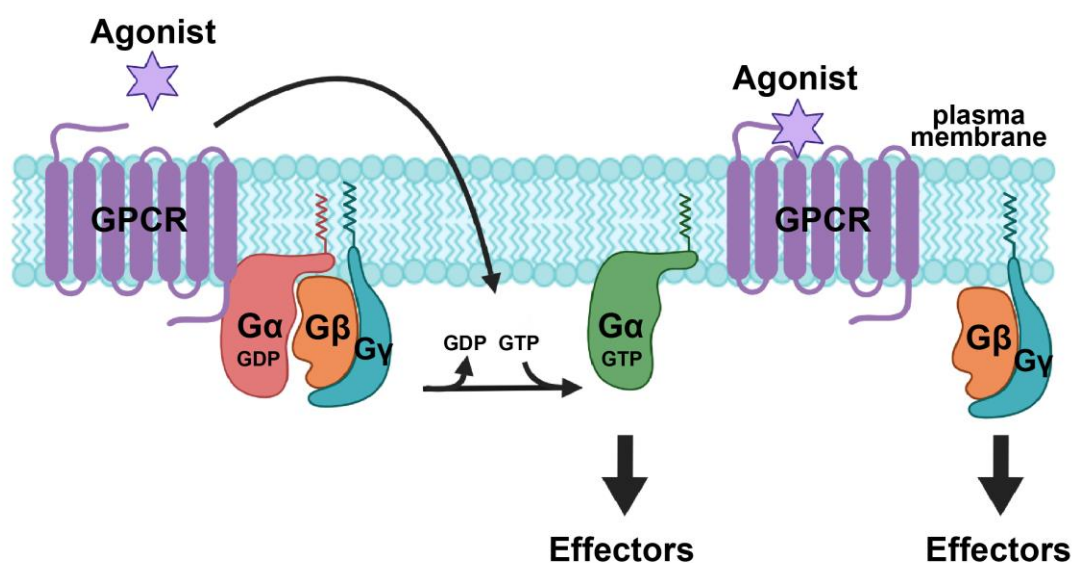


Figure 1.1. G protein-coupled receptor (GPCR) signaling mechanism. GPCRs are coupled to heterotrimeric G proteins made up of a  $G\alpha$ ,  $G\beta$ , and  $G\gamma$  subunit. In the inactive state, the  $G\alpha$  subunit is bound to GDP. Binding of an agonist to the GPCR causes a conformational change in the receptor and subsequent exchange of GDP for GTP on the  $G\alpha$  subunit. This leads to the dissociation of the  $G\alpha$  and  $G\beta\gamma$  subunits, which regulate downstream effector enzymes.

Due to their link to a wide range of diseases, GPCRs are popular pharmaceutical targets, making up ~30% of FDA approved drugs (3-6). However, the development of drugs that target GPCRs is becoming more challenging due to the limited structural information resulting from the inherent instability of GPCRs and off-target effects. Since signal transduction pathways are made up of a complex network of proteins that communicate with one another to convert an external signal to an internal response, a potential alternative would be to target the players in the signaling cascade downstream of GPCRs.

### 1.1 Regulator of G Protein Signaling Proteins

Regulator of G protein signaling (RGS) proteins function as GTPase activating proteins (GAP) to facilitate the rapid turn off of GPCR signaling pathways (7). By themselves, activated  $G\alpha$  subunits intrinsically hydrolyze GTP to GDP at a physiologically unfeasible slow rate (2). This led to the discovery of RGS proteins from the *Sst2p* gene in *Saccharomyces cerevisiae* (8,9). RGS proteins accelerate the rate of GTP hydrolysis up to 1,000-fold, resulting in the reassociation of the  $G\alpha$  and  $G\beta\gamma$  subunits and termination of the signal cascade (Figure 1.2) (7). Although there are 21  $G\alpha$  subunits divided into four main classes ( $G\alpha_s$ ,  $G\alpha_i$ ,  $G\alpha_q$ ,  $G\alpha_{12/13}$ ), RGS proteins only have GAP activity towards the  $G_i$  and  $G_q$  subfamilies (7,10-13).

There are twenty RGS proteins that are categorized into four subfamilies based on sequence similarity (RZ, R4, R7, and R12) (7,10,11). All the subfamilies share a conserved RH (RGS homology) domain that serves as the  $G\alpha$  binding site and is required for stimulating GTP hydrolysis. The subfamilies differ in the presence of extra domains flanking the RH domain that contribute to subcellular localization and  $G\alpha$  specificity and affinity (Figure 1.3) (7,10,11,14,15). The RH domain is made up of nine alpha helices that form two subdomains, the terminal and bundle subdomains (14,15). The terminal subdomain is made up of  $\alpha 1$ ,  $\alpha 2$ ,  $\alpha 3$ ,  $\alpha 8$  and  $\alpha 9$ , while the bundle subdomain is made up of  $\alpha 4$ - $\alpha 7$ . The base of the bundle subdomain, along with loops from  $\alpha 7$  and  $\alpha 8$  form the  $G\alpha$  binding site (14-16). The mechanism of RGS-stimulated GTP hydrolysis requires the RGS protein to bind the switch regions of the  $G\alpha$  subunit. This binding reduces the flexibility of the switch regions on the  $G\alpha$  subunit and stabilizes the transition state. This interaction is dependent upon a highly conserved asparagine or serine residue that interacts with the catalytic glutamine residue of  $G\alpha$  (10,14,16-18).

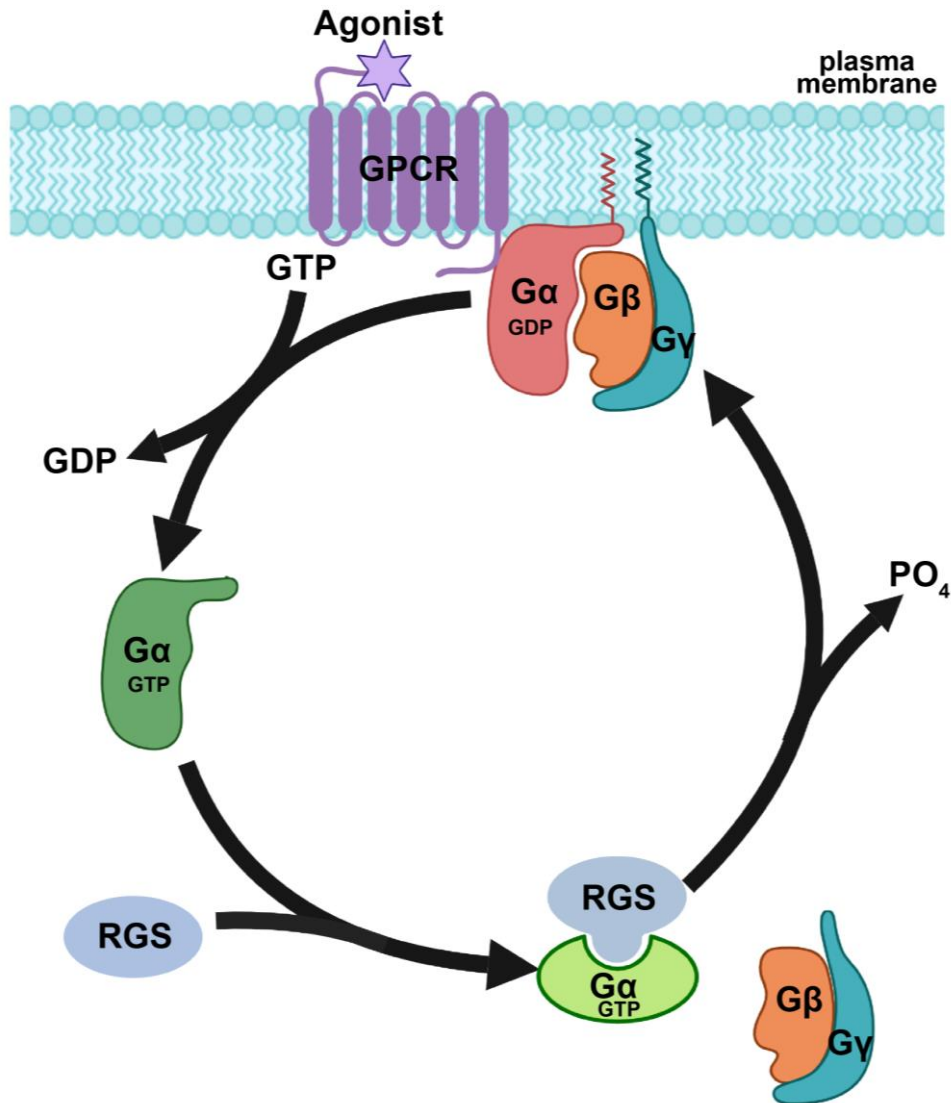


Figure 1.2. Regulator of G protein Signaling (RGS) mechanism. GPCR signaling is terminated by hydrolysis of GTP on G $\alpha$ . This process is stimulated by RGS proteins that accelerate the rate of GTP hydrolysis. Upon binding of RGS proteins, GTP is hydrolyzed, resulting in the release of PO<sub>4</sub> and reassociation of G $\alpha$  with G $\beta\gamma$ .

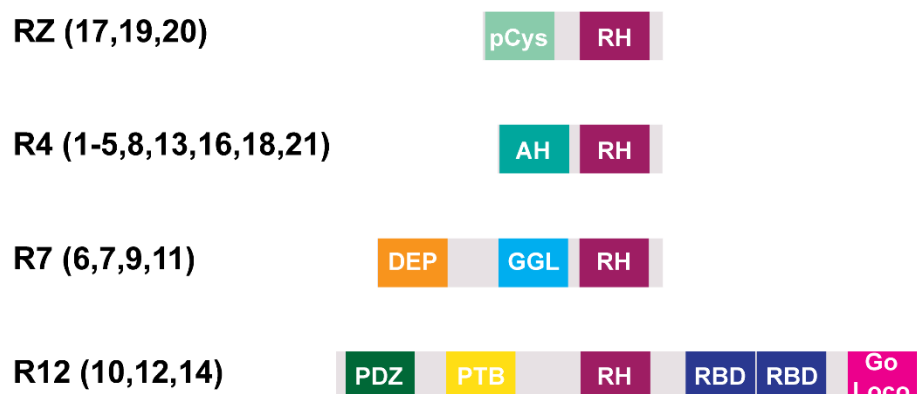


Figure 1.3. Domain architecture of RGS subfamilies. There are twenty RGS proteins split into four subfamilies. Domain abbreviations: pCys (poly-cysteine string), RH (RGS homology), AH (amphipathic helix), DEP (disheveled/Egl10/pleckstrin domain), GGL (G protein  $\gamma$ - like), PDZ (Psd-95/DlgA/ZO1 domain), PTB (phosphotyrosine binding domain), RBD (Raf-like Ras binding domain), Go Loco ( $G\alpha_{i/o}$  loco).

RGS proteins are regulated by additional domains that dictate interactions with specific proteins and/or localization. Of the four subfamilies, the R4 and RZ are the simplest and function mainly as inhibitors of G protein signaling (19). The most extensively studied RGS family is the R4 family, which contain an N-terminal amphipathic  $\alpha$ -helical region (11). The RZ family contains a short N-terminal cysteine-rich region that can be post-translationally modified to regulate localization and trafficking (12,19-20). The R7 and R12 families are more complex and contain additional domains that allow them to interact with G proteins and other signaling proteins, thereby integrating multiple aspects of G protein signaling (19). The R7 subfamily contains an N-terminal DEP (disheveled/Egl10/pleckstrin) and GGL (G protein  $\gamma$  subunit-like) domains that contribute to membrane localization (10,11,19). Finally, the R12 subfamily contains a PDZ (Psd-95/DlgA/ZO1), PTB (phosphotyrosine binding), RBD (Raf-like Ras binding domain), and Go Loco ( $G\alpha_{i/o}$ -Loco) interaction domains which are responsible for downstream signaling (10,11,19).

Due to their ability to interact with activated  $G\alpha_o$ ,  $G\alpha_i$ ,  $G\alpha_z$ , and  $G\alpha_{q/11}$ , RGS proteins regulate signaling cascades downstream of numerous receptors, including the D2 dopamine,  $\mu$  opioid, and 5-HT<sub>1A</sub> serotonin receptors (21-24). As a result, a growing number of studies have linked RGS proteins to a wide range of diseases caused by impaired signaling. Previous studies have shown patients with schizophrenia have decreased mRNA levels of RGS4 (25). Other studies have shown increased expression of RGS9 in patients with Parkinson's disease (26). Knock

out/down studies of RGS proteins have also implicated certain isoforms in specific physiological conditions including hypertension (RGS2), hypotension (RGS5), anxiety, depression, and alcoholism (RGS6), and cancer (RGS17) (27-32). Therefore, the ability of RGS proteins to negatively regulate GPCR signaling makes them potential drug targets.

## 1.2 Regulator of G Protein Signaling 17

One member of the RGS family that is a potential therapeutic target for lung cancer is RGS17 (31,32). RGS17 is a member of the RZ subfamily and was discovered in 1999 as a  $G\alpha_o$  interaction partner in yeast (33,34). Although RGS17 is ubiquitously expressed, it is mainly found in the central nervous system, with the highest expression localized to the cerebellum, nucleus accumbens, parahippocampal gyrus, and putamen (12,34,35, 36). It has been found to interact with  $G\alpha_{i1-3}$ ,  $G\alpha_o$ , and  $G\alpha_z$ , but preferentially binds to  $G\alpha_i$  and  $G\alpha_o$ . Thus, RGS17 is a potent regulator of cAMP and  $Ca^{2+}$  signaling through its inhibition of  $G\alpha_{i/o}$  (12,34).

Although normal RGS17 expression is mainly localized to the brain, studies have shown increased levels of RGS17 in tumor cells of other tissues and organs (31,32). In a genome-wide linkage study, a major susceptibility locus for lung cancer was identified on chromosome 6q23-25, corresponding to RGS17 (31,37). Therefore, RGS17 was identified as a potential marker for familial lung cancer. This was supported by studies that showed an ~8-fold increase in expression of RGS17 in lung cancer tumors (31,37,38). Furthermore, knockdown of RGS17 by RNA interference (RNAi) in a mouse xenograft model of cancer resulted in a 59-75% decrease in tumor volume (31,38). The mechanistic role of RGS17 in lung cancer is attributed to its GAP activity toward  $G\alpha_i$  and  $G\alpha_o$ , and the subsequent increase in cAMP, resulting in activation of the PKA-CREB pathway (38). Overexpression of RGS17 decreased  $G\alpha_{i/o}$  signaling, which in turn decreased inhibition of adenylyl cyclase (38). This caused an accumulation of cAMP, which increased PKA activity and phosphorylation of cAMP response element-binding protein (CREB). Phosphorylated CREB can then bind to cAMP response elements (CRE) to promote the transcription of genes involved in growth and migration (38).

### 1.2.1 Inhibition of RGS17

The proliferative effect of RGS17 in lung cancers has been attributed to its interaction with  $G\alpha_{i/o}$ , which results in the accumulation of cAMP (38). Therefore, targeting the protein-protein

interaction between RGS17 and  $G\alpha_{i/o}$  with small molecule inhibitors could be a potential therapeutic strategy. Using structure-based drug design guided by the crystal structure of RSG4-bound to  $G\alpha_{i1}$  (39) and high throughput screening (HTS), six compounds that inhibit RGS17- $G\alpha$  binding with micromolar affinity have been identified (31,40). However, the inhibitors did not exhibit high specificity for RGS17- $G\alpha$  inhibition and/or contained potentially reactive functional groups, limiting their usefulness (40). More studies are being done to identify specific and nonreactive inhibitors using HTS of small molecule chemical libraries, however, this method is time consuming (41-46).

### 1.2.2 Regulation of RGS17

In order to develop specific and potent inhibitors of RGS17, more studies are needed to elucidate its regulation. Currently, the only known mechanisms of RGS17 regulation are post-translational modifications and degradation (12,47,48). RGS17 contains an N-terminal cysteine-rich region that can be heavily palmitoylated to promote membrane localization (12,20). Additionally, RGS17 contains six casein kinase and three protein kinase C recognition motifs that can be potentially phosphorylated (47,49). It was also found that Y137 can be phosphorylated, however, the specific kinase and functional consequences of phosphorylation are not known (49). In addition to palmitoylation and phosphorylation, RGS17 can also be sumoylated by SUMO1, 2, and 3, with K90 and K121 being the likely sites (49-51). Sumoylation of RGS17 has been suggested to alter the function of RGS17 as a protein scaffold or effector antagonist (49,51). RGS17 can also be ubiquitinated on K147, but the role of ubiquitination is unclear (49). In addition, RGS17 may also be regulated by other protein-protein interactions. For example, some RZ and R4 subfamily members are regulated by  $Ca^{2+}$ /calmodulin, in which binding  $Ca^{2+}$ /calmodulin relieves inhibition by  $PIP_3$  (52,53). Therefore, further structural studies illustrating the regulation of RGS17 can be used to exploit specific interactions as targets for new therapeutic approaches.

### 1.3 Phospholipase C

Phospholipase C (PLC) enzymes are downstream effectors of many GPCR signaling pathways. They hydrolyze the inner membrane lipid phosphatidylinositol 4,5-bisphosphate (PIP<sub>2</sub>) to produce the second messengers diacylglycerol (DAG) and inositol 1,4,5-triphosphate (IP<sub>3</sub>). These second messengers activate protein kinase C and promote intracellular calcium (Ca<sup>2+</sup>) release (Figure 1.4) (54-58). This allows PLC enzymes to regulate numerous signal transduction pathways involving cell growth, development, and differentiation (59).

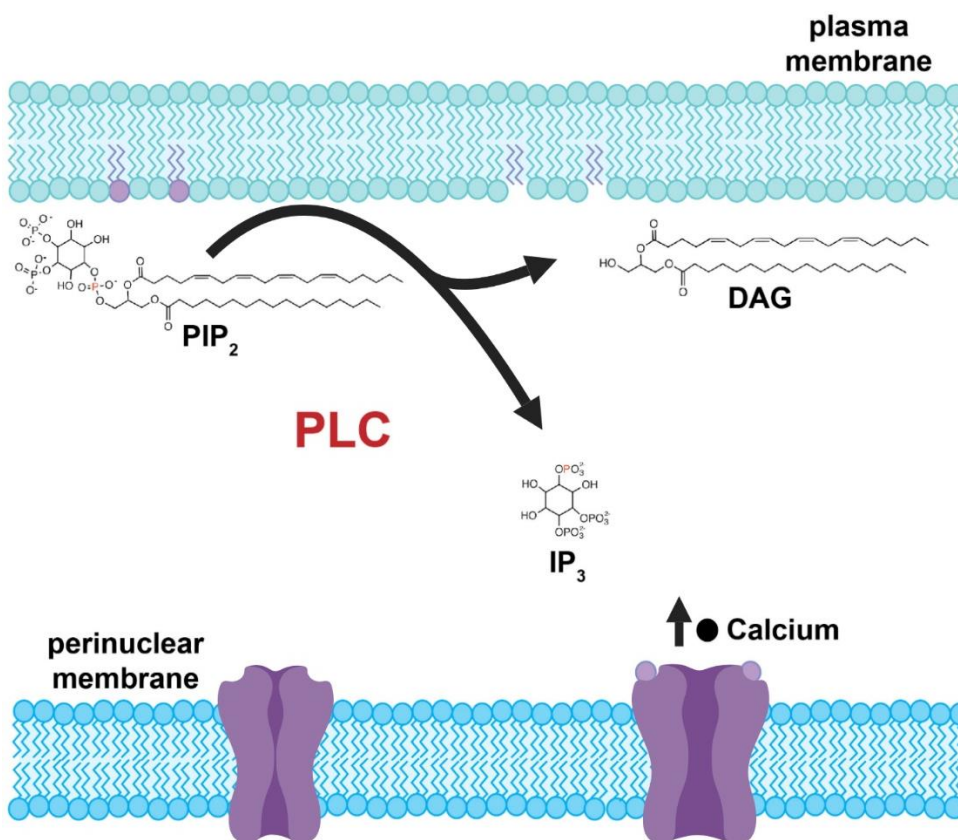


Figure 1.4. Phospholipase C (PLC) signaling mechanism. PLC enzymes hydrolyze the inner membrane lipid phosphatidylinositol 4,5-bisphosphate (PIP<sub>2</sub>) into the second messengers diacylglycerol (DAG) and inositol 1,4,5-triphosphate (IP<sub>3</sub>). DAG goes on to activate other proteins such as protein kinase C (PKC), while IP<sub>3</sub> binds to intracellular IP<sub>3</sub> receptors to release calcium.

Thirteen mammalian PLC isozymes have been identified that are divided into six subfamilies (PLC $\beta$ , PLC $\epsilon$ , PLC $\gamma$ , PLC $\eta$ , PLC $\delta$ , PLC $\zeta$ ) (54-58,60). The PLC superfamily shares conserved

core domains thought to be required for efficient lipase activity, and includes a pleckstrin homology (PH) domain, EF-hands, the catalytic TIM barrel domain, and a C2 domain. The mechanism of PIP<sub>2</sub> hydrolysis by these enzymes involves an acid/base catalyzed reaction, wherein the active site forms a covalent inositol 1,2-cyclic phosphodiester intermediate, and releases DAG. The intermediate is subsequently hydrolyzed to release IP<sub>3</sub>. This mechanism requires two conserved histidine residues in the TIM barrel, as well as Ca<sup>2+</sup>, which is coordinated by four acidic residues (57,58).

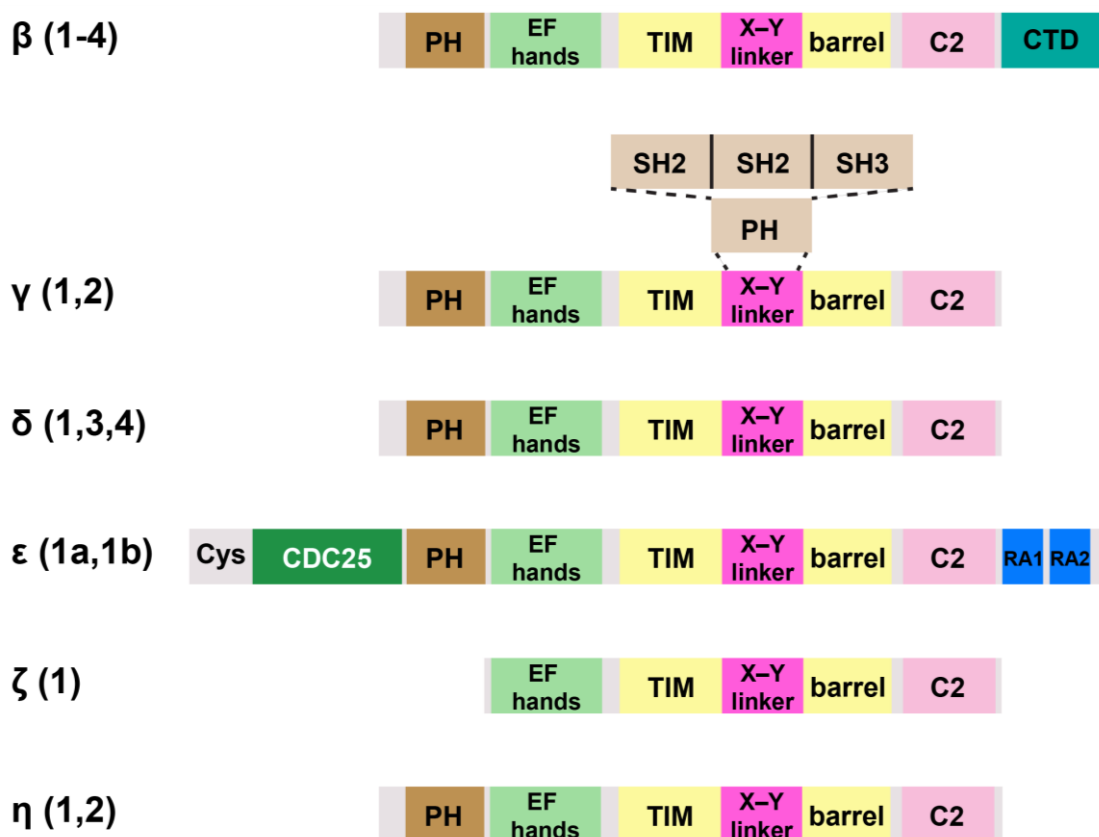


Figure 1.5. Domain architecture of PLC subfamilies. There are thirteen members of PLC proteins split into six subfamilies. Domain abbreviations: pleckstrin homology (PH), C-terminal domain (CTD), Src homology (SH2/3), Ras association (RA).

Although all PLCs hydrolyze PIP<sub>2</sub>, they are differentially controlled by the presence or absence of regulatory domains that typically flank the conserved core (54-58) (Figure 1.5). PLCβ contains proximal and distal C-terminal domains (CTDs) that are involved in basal and Gα<sub>q</sub>-dependent activation. Gβγ and Rac also activate PLCβ through binding to the core domains (57-

59, 61-65). PLC $\gamma$  contains a large insert in the X-Y linker that contains a split PH domain involved in receptor tyrosine kinase (RTK) binding. This results in RTK-dependent phosphorylation of PLC $\gamma$ , leading to its activation (57,58,66). PLC $\delta$  lacks additional regulatory domains and is regulated by PIP<sub>2</sub> and Ca<sup>2+</sup> (57,58,67). The PLC $\delta$  PH domain is required for membrane binding through its ability to bind PIP<sub>2</sub> with high specificity and affinity (67). PLC $\zeta$  lacks the PH domain and additional regulatory domains, but contains a positively charged X-Y linker that may promote membrane association (58,68). PLC $\eta$  contains a C-terminal extension of unknown function but has been reported to be activated by G $\beta\gamma$  (58,69). Finally, PLC $\epsilon$  contains an N-terminal CDC25 domain and two C-terminal Ras association (RA) domains. Its regulation is also more complex, as it is activated downstream of GPCRs and RTKs through direct interactions with the G $\beta\gamma$  heterodimer and the small GTPases Ras, Rap, and Rho (56, 70-79).

Due to their involvement with various signaling cascades, PLCs are linked to numerous physiological disorders (80). PLC $\beta$ 1 and PLC $\gamma$ 1 are both highly expressed in the brain, and contribute to the regulation of synaptic plasticity and cortical development (59,80-83). Knock out and knock in studies in mice of PLC $\beta$ 1 and PLC $\gamma$ 1, respectively, displayed an epilepsy phenotype (84,85). PLC $\delta$ 4 and PLC $\zeta$  are both highly expressed in sperm, and knock out studies in male mice resulted in reduced fertility (59,86,87). PLC $\epsilon$  is ubiquitously expressed and has been linked to cardiac hypertrophy, skin inflammation, and cancer development and progression (59,70,88-90). Although dysregulation of PLC enzymes expression or activity has been implicated in a wide range of physiological disorders, the molecular mechanisms by which they are activated are still not well understood.

#### 1.4 Phospholipase C $\epsilon$

PLC $\epsilon$  is the most recently discovered member of the PLC family. A yeast two-hybrid screen for binding partners of Ras in *C. elegans* resulted in the discovery of PLC210 (60). The mammalian ortholog, PLC $\epsilon$ , is expressed in various tissues and almost all cell types (58,78,91,92). PLC $\epsilon$  is present as two splice forms, PLC $\epsilon$ 1a and PLC $\epsilon$ 1b, and are the largest PLC isozymes with molecular weights of 260 and 230 kDa, respectively (93). In addition to the core domains, PLC $\epsilon$  also contains regulatory domains at the N- and C-termini. At the N-terminus, there is a CDC25 domain that is a guanine nucleotide exchange factor (GEF) for the small GTPase Rap1A (71,94,95).

GEFs catalyze the exchange of GDP for GTP on GTPases, converting them to the active state (71,94-96). At the C-terminus, there are two Ras association (RA1 and RA2) domains that bind to Rap1A, Ras and muscle-specific A-kinase anchoring protein (mAKAP $\beta$ ) (70-79,97). Currently, the only high-resolution structural information available is of the PLC $\epsilon$  RA domains alone and the RA2 domain in complex with H-Ras (98). Based on the NMR structures of the RA domains, both RA1 and RA2 have similar ubiquitin-like folds. However, only the RA2 domain binds to activated small G proteins (98).

Although PLC $\epsilon$  is ubiquitously expressed, it is expressed at highest levels in the heart, where it regulates the development and function of cardiomyocytes (59). More specifically, PLC $\epsilon$  is linked to cardiovascular disease through its role in promoting cardiac hypertrophy (70,99). Cardiac hypertrophy is caused by an increase in cardiomyocyte size, resulting in abnormal enlargement of the heart muscle in response to hormonal and mechanical stimuli from physiological stress (99). Although cardiac hypertrophy is an adaptive response, prolonged stress on the heart, coupled with the increase in heart size, can lead to congestive heart failure (99). Studies have shown that knock-down of PLC $\epsilon$  by siRNA reduces agonist-induced cardiac hypertrophy in rat ventricular myocytes (70). Therefore, PLC $\epsilon$  is a therapeutic target for the treatment of cardiac hypertrophy. However, designing small molecule inhibitors to specifically inhibit PLC $\epsilon$  may be difficult, given the conservation of the PLC active site. Therefore, more structural information is required to develop small molecules that target the interactions unique to PLC $\epsilon$ .

#### 1.4.1 Regulation of PLC $\epsilon$

PLC $\epsilon$  is regulated through direct interactions with G proteins that are activated by signaling pathways emanating from GPCRs and RTKs (56,70-79,97) (Figure 1.6). PLC $\epsilon$  can be activated downstream of G<sub>12/13</sub>-coupled receptors via interactions with RhoA (72). For example, thrombin activates G $\alpha_{12/13}$ , stimulating RhoGEFs that activate RhoA (79,92). RhoA-dependent activation requires an insertion within the TIM barrel domain, but its binding site is unknown (72,73). PLC $\epsilon$  can also be activated downstream of RTKs, including the epidermal growth factor receptor (EGFR) (79,91). Binding of EGF stimulates the receptor, culminating in the activation of H-Ras, which in turn binds to the PLC $\epsilon$  RA2 domain and stimulates lipase activity (58,91).

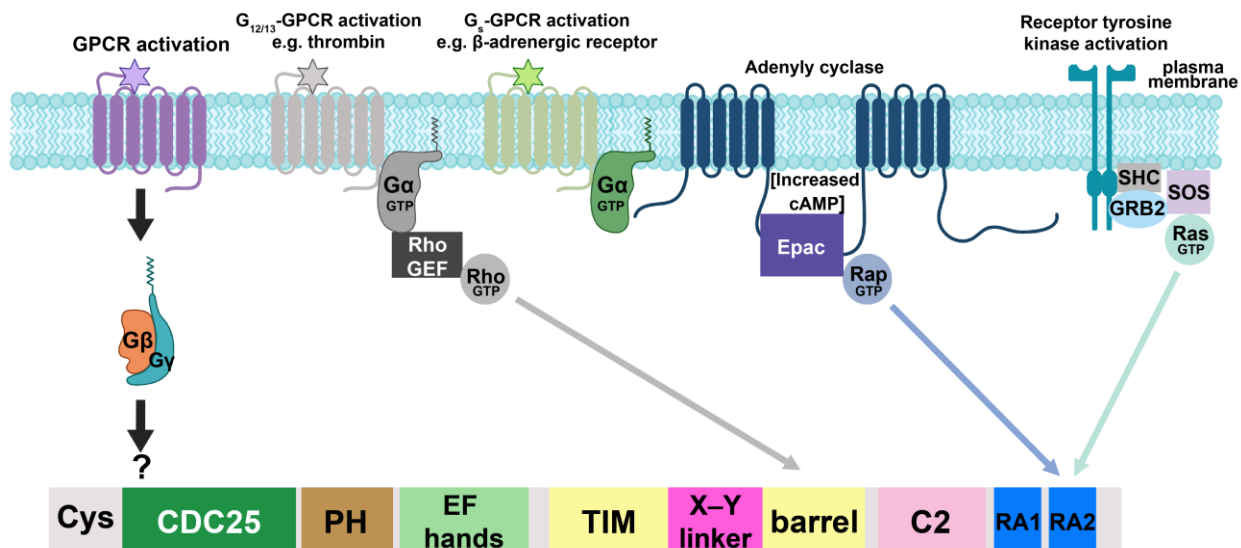


Figure 1.6. Regulation of PLC $\epsilon$ . PLC $\epsilon$  acts downstream of GPCRs coupled to G $_q$ , G $_{12/13}$ , G $_s$ , and receptor tyrosine kinases (RTK) through interaction with G $\beta\gamma$  and small G proteins, Rho, Rap, and Ras. Abbreviations: exchange protein activated by cAMP (Epac), cyclic AMP (cAMP), Src homology and Collagen (SHC), growth factor receptor-bound protein 2 (GRB2), Son of Sevenless (SOS).

The best characterized pathway of PLC $\epsilon$  activation is mediated by the small GTPase Rap1A. Activation of  $\beta$ -adrenergic receptors by epinephrine leads to the accumulation of cyclic AMP (cAMP), which activates Epac (exchange protein directly activated by cAMP), a guanine nucleotide exchange factor for Rap1A (56,70,100-102). Rap1A·GTP then binds to the RA2 domain of PLC $\epsilon$ , translocating the complex to the perinuclear membrane (56,70,75,103). The PLC $\epsilon$  CDC25 domain can further stimulate lipase activity by activating Rap1A, which in turn binds to the RA2 domain. PI $_4$ P is then hydrolyzed to generate a local pool of DAG, which activates PKC (70,76,100-104). PKC, in turn, phosphorylates protein kinase D (PKD), ultimately increasing the expression of genes involved in cardiac hypertrophy (101,102).

Taken together, PLC $\epsilon$  is a bifunctional regulator of cellular processes as an activator and effector of Rap1A (56,71). While it is known that Rap1A activates PLC $\epsilon$  at the perinuclear membrane through direct interactions between Rap1A and the PLC $\epsilon$  RA2 domain, the molecular details underlying the process are unknown (70,75,76,97,101,102). PLC $\epsilon$  has low basal activity and resides primarily in the cytoplasm (56). Binding of Rap1A to the PLC $\epsilon$  RA2 domain translocates PLC $\epsilon$  to the perinuclear membrane, increasing lipase activity (75,79). This activation could be due to conformational changes within PLC $\epsilon$  that release autoinhibition and/or enhance

membrane association (98). Due to the lack of biochemical and structural data, further studies are needed in order to elucidate the exact mechanism by which PLC $\epsilon$  is activated by Rap1A and vice versa. Knowledge of these mechanisms will facilitate the development of small molecules targeting the interactions between these proteins and potentially serve as lead compounds for the treatment of cardiac hypertrophy.

## 1.5 References

1. Weis, W.I., Kobilka, B.K. (2018). The molecular basis of G protein-coupled receptor activation. *Ann Rev Biochem.*, **87**, 897-919.
2. Oldham, W. M., and Hamm, H. E. (2008). Heterotrimeric G protein activation by G-protein-coupled receptors. *Nat Rev Mol Cell Biol.*, **9**, 60-71.
3. Wise, A., Gearing, K., Rees, S. (2002). Target Validation of G-protein Coupled Receptors. *Drug Discov. Today*, **7**, 235–246.
4. Knox, C., Law, V., Jewison, T., et al. (2011). DrugBank 3.0: A Comprehensive Resource for “Omics” Research on Drugs. *Nucleic Acids Res.*, **39**, D1035–D1041.
5. Garland, S. (2013). Are GPCRs Still a Source of New Targets? *J Biomol Screen.*, **18**(9), 947-966.
6. Sriram, K., Insel, P.A. (2017). G Protein-Coupled Receptors as Targets for Approved Drugs: How Many Targets and How Many Drugs? *Mol Pharmacol.*, **93**, 251-258.
7. De Vries, L., Zheng, B., Fischer, T., Elenko, E., and Farquhar, M. G. (2000). The Regulator of G Protein Signaling Family. *Annu Rev Pharmacol Toxicol.*, **40**, 235-271.
8. Dohlman, H. G., Apaniesk, D., Chen, Y., Song, J., and Nusskern, D. (1995). Inhibition of G-protein signaling by dominant gain-of-function mutations in Sst2p, a pheromone desensitization factor in *Saccharomyces cerevisiae*. *Mol Cell Biol.*, **15**, 3635-3643.
9. Koelle, M. R., and Horvitz, H. R. (1996). EGL-10 regulates G protein signaling in the *C. elegans* nervous system and shares a conserved domain with many mammalian proteins. *Cell*, **84**, 115-125.
10. Ross, E. M., and Wilkie, T. M. (2000). GTPase-activating proteins for heterotrimeric G proteins: regulators of G protein signaling (RGS) and RGS-like proteins. *Annu Rev Biochem.*, **69**, 795-827.
11. Woodward, G.E., Jardin, I., Berna-Erro, A., Salido, G.M., Rosado, J.A. (2015). Regulators of G-protein-signaling proteins: negative modulators of G-protein coupled receptor signaling. *Int Rev Cell Mol Biol.*, **317**, 1937-6448.

12. Nunn, C., Mao, H., Chidiac, P., and Albert, P. R. (2006). RGS17/RGSZ2 and the RZ/A family of regulators of G-protein signaling. *Semin Cell Dev Biol.*, **17**, 390-399.
13. Berman, D. M., Wilkie, T. M., and Gilman, A. G. (1996). GAIP and RGS4 are GTPase-activating proteins for the Gi subfamily of G protein alpha subunits. *Cell*, **86**, 445-452.
14. Tesmer, J. J., Berman, D. M., Gilman, A. G., and Sprang, S. R. (1997). Structure of RGS4 bound to AlF<sub>4</sub><sup>-</sup>-activated G<sub>i</sub>α<sub>1</sub>: stabilization of the transition state for GTP hydrolysis. *Cell*, **89**, 251-261.
15. Popov, S., Yu, K., Kozasa, T., and Wilkie, T. M. (1997). The regulators of G protein signaling (RGS) domains of RGS4, RGS10, and GAIP retain GTPase activating protein activity in vitro. *Proc Natl Acad Sci U S A*, **94**, 7216-7220.
16. Tesmer, J. J. (2009). Structure and function of regulator of G protein signaling homology domains. *Prog Mol Biol Transl Sci.*, **86**, 75-113.
17. Natochin, M., McEntaffer, R. L., and Artemyev, N. O. (1998). Mutational analysis of the Asn residue essential for RGS protein binding to G-proteins. *J Biol Chem.*, **273**, 6731-6735.
18. Posner, B. A., Mukhopadhyay, S., Tesmer, J. J., Gilman, A. G., and Ross, E. M. (1999). Modulation of the Affinity and Selectivity of RGS Protein Interaction with GαSubunits by a Conserved Asparagine/Serine Residue†. *Biochemistry*, **38**, 7773-7779.
19. Hollinger, S., Helper, J.R. (2002). Cellular Regulation of RGS Proteins: Modulators and Integrators of G Protein Signaling. *Pharmacol Rev.*, **54**, 527-559.
20. De Vries, L., Elenko, E., Hubler, L., Jones, T. L., and Farquhar, M. G. (1996). GAIP is membrane-anchored by palmitoylation and interacts with the activated (GTP-bound) form of G alpha i subunits. *Proc Natl Acad Sci U S A*, **93**, 15203-15208.
21. Clark, M.J., Harrison, C., Zhong, H., Neubig, R.R., Traynor, J.R. (2003). Endogenous RGS protein action modulates mu-opioid signaling through Galphao. Effects on adenylyl cyclase, extracellular signal-regulated kinases, and intracellular calcium pathways. *J Biol Chem.*, **278**(11), 9418-25.
22. Talbot, J.N., Roman, D.L., Clark, M.J., Roof, R.A., Tesmer, J.J., Neubig, R.R., Traynor, J.R. (2010). Differential modulation of mu-opioid receptor signaling to adenylyl cyclase by regulators of G protein signaling proteins 4 or 8 and 7 in permeabilized C6 cells is Galpha subtype dependent. *J Neurochem.*, **112**(4), 1026-34.
23. Ghavami, A., Hunt, R.A., Olsen, M.A., Zhang, J., Smith, D.L., Kalgaonkar, S., Rahman, Z., Young, K.H. (2004). Differential effects of regulator of G protein signaling (RGS) proteins on serotonin 5-HT<sub>1A</sub>, 5-HT<sub>2A</sub>, and dopamine D<sub>2</sub> receptor mediated signaling and adenylyl cyclase activity. *Cell Signal*, **16**(6), 71121.

24. Talbot, J.N., Jutkiewicz, E.M., Graves, S.M., Clemans, C.F., Nicol, M.R., Mortensen, R.M., Huang, X., Neubig, R.R., Traynor, J.R. (2010). RGS inhibition at G(alpha)i2 selectively potentiates 5-HT1A-mediated antidepressant effects. *Proc Natl Acad Sci U S A*, **107**(24), 11086-91.
25. Mirnics, K., Middleton, F.A., Stanwood, G.D., Lewis, D.A., Levitt, P. (2001). Disease-specific changes in regulator of G protein signaling 4 (RGS4) expression in schizophrenia. *Mol Psychiatry*, **6**(3), 293-301.
26. Tekumalla, P.K., Calon, F., Rahman, Z., Birdi, S., Rajput, A.H., Hornykiewicz, O., Di Paolo, T., Bedard, P.J., Nestler, E.J. (2001). Elevated levels of DeltaFosB and RGS9 in striatum in Parkinson's disease. *Biol Psychiatry*, **50**(10), 813-6.
27. Heximer, S.P., Knutsen, R.H., Sun, X., Kaltenbronn, K.M., Rhee, M.H., Peng, N., Oliveiras-dos-Santos, A., Penninger, J.M., Muslin, A.J., Steinberg, T.H., Wyss, J.M., Mecham, R.P., Blumer, K.J. (2003). Hypertension and prolonged vasoconstrictor signaling in RGS2-deficient mice. *J Clin Invest.*, **111**(4), 445-52.
28. Cho, H., Park, C., Hwang, I.Y., Han, S.B., Schimel, D., Despres, D., Kehrl, J.H. (2008). Rgs5 targeting leads to chronic low blood pressure and a lean body habitus. *Mol Cell Biol.*, **28**(8), 2590-7.
29. Stewart, A., Maity, B., Andereg, S.P., Allamargot, C., Yang, J., Fisher, R.A. (2015). Regulator of G protein signaling 6 is a critical mediator of both reward-related behavioral and pathological responses to alcohol. *Proc Natl Acad Sci U S A*, **112**(7), E786-95.
30. Stewart, A., Maity, B., Wunsch, A.M., Meng, F., Wu, Q., Wemmie, J.A., Fisher, R.A. (2014). Regulator of G-protein signaling 6 (RGS6) promotes anxiety and depression by attenuating serotonin-mediated activation of the 5-HT(1A) receptor-adenylyl cyclase axis. *FASEB J.*, **28**(4), 1735-44.
31. Hayes, M. P., and Roman, D. L. (2016) Regulator of G Protein Signaling 17 as a Negative Modulator of GPCR Signaling in Multiple Human Cancers. *The AAPS Journal* **18**, 550-559.
32. Bodle, C.R., Mackie, D.I., Roman, D.L. (2013). RGS17: an emerging therapeutic target for lung and prostate cancers. *Future Med Chem.*, **5**(9), 1-20.
33. Jordan, J.D., Carey, K.D., Stork, P.J., Iyengar, R. (1999). Modulation of rap activity by direct interaction of Galpha(o) with Rap1 GTPase-activating protein". *J Biol Chem.*, **274** (31), 21507-10.
34. Mao, H., Zhao, Q., Daigle, M., Ghahremani, M. H., Chidiac, P., and Albert, P. R. (2004). RGS17/RGS22, a Novel Regulator of Gi/o, Gz, and Gq Signaling. *J Biol Chem.*, **279**, 26314-26322.
35. Larminie, C., Murdock, P., Walhin, J.-P., Duckworth, M., Blumer, K. J., Scheideler, M. A., and Garnier, M. (2004). Selective expression of regulators of G-protein signaling (RGS) in the human central nervous system. *Mol Brain Res.*, **122**, 24-34.

36. Garzón, J., Rodríguez-Muñoz, M., López-Fando, A., García-España, A., Sánchez-Blázquez, P. (2004). RGSZ1 and GAIP regulate mu- but not delta-opioid receptors in mouse CNS: role in tachyphylaxis and acute tolerance. *Neuropsychopharmacology*, **29**(6), 1091–1104.
37. You, M., Wang, D., Liu, P., Vikis, H., James, M., Lu, Y., Wang, Y., Wang, M., Chen, Q., Jia, D., Liu, Y., Wen, W., Yang, P., Sun, Z., Pinney, S. M., Zheng, W., Shu, X. O., Long, J., Gao, Y. T., Xiang, Y. B., Chow, W. H., Rothman, N., Petersen, G. M., de Andrade, M., Wu, Y., Cunningham, J. M., Wiest, J. S., Fain, P. R., Schwartz, A. G., Girard, L., Gazdar, A., Gaba, C., Rothschild, H., Mandal, D., Coons, T., Lee, J., Kupert, E., Seminara, D., Minna, J., Bailey-Wilson, J. E., Amos, C. I., and Anderson, M. W. (2009). Fine Mapping of Chromosome 6q23-25 Region in Familial Lung Cancer Families Reveals RGS17 as a Likely Candidate Gene. *Clin Cancer Res.*, **15**, 2666-2674.
38. James, M. A., Lu, Y., Liu, Y., Vikis, H. G., and You, M. (2009). RGS17, an Overexpressed Gene in Human Lung and Prostate Cancer, Induces Tumor Cell Proliferation Through the Cyclic AMP-PKA-CREB Pathway. *Cancer Res.*, **69**, 2108-2116.
39. Soundararajan, M., Willard, F. S., Kimple, A. J., Turnbull, A. P., Ball, L. J., Schoch, G. A., Gileadi, C., Fedorov, O. Y., Dowler, E. F., Higman, V. A., Hutsell, S. Q., Sundstrom, M., Doyle, D. A., and Siderovski, D. P. (2008). Structural diversity in the RGS domain and its interaction with heterotrimeric G protein alpha-subunits. *Proc Natl Acad Sci U S A*, **105**, 6457-6462.
40. Jin Y., Zhong, H., Omnaas, J.R., Neubig, R.R., Mosberg, H.I. (2004). Structure-based design, synthesis, and pharmacologic evaluation of peptide RGS4 inhibitors. *J Pept Res.*, **63**(2), 141–6.
41. Roman, D.L., Talbot, J.N., Roof, R.A., Sunahara, R.K., Traynor, J.R., Neubig, R.R. (2007). Identification of small-molecule inhibitors of RGS4 using a high-throughput flow cytometry protein interaction assay. *Mol Pharmacol.*, **71**(1), 169–75.
42. Monroy, C.A., Mackie, D.I., Roman, D.L. (2013). A high throughput screen for RGS proteins using steady state monitoring of free phosphate formation. *PLoS One*, **8**(4), e62247.
43. Mackie, D.I., Roman, D.L. (2011). Development of a novel high-throughput screen and identification of small-molecule inhibitors of the Galpha-RGS17 protein-protein interaction using AlphaScreen. *J Biomol Screen.*, **16**(8), 869–77.
44. Roman, D.L., Ota, S., Neubig, R.R. (2009). Polyplexed flow cytometry protein interaction assay: a novel high-throughput screening paradigm for RGS protein inhibitors. *J Biomol Screen.*, **14**(6), 610–9.
45. Roman, D.L., Blazer, L.L., Monroy, C.A., Neubig, R.R. (2010). Allosteric inhibition of the regulator of G protein signaling-Galpha protein-protein interaction by CCG-4986. *Mol Pharmacol.*, **78**(3), 360–5.

46. Blazer, L.L., Roman, D.L., Chung, A., Larsen, M.J., Greedy, B.M., Husbands, S.M., et al. (2010). Reversible, allosteric small-molecule inhibitors of regulator of G protein signaling proteins. *Mol Pharmacol.* **78**(3), 524–33.
47. Wang, J., Ducret, A., Tu, Y., Kozasa, T., Aebersold, R., and Ross, E. M. (1998). RGSZ1, a Gz-selective RGS protein in brain. Structure, membrane association, regulation by Galphaz phosphorylation, and relationship to a Gz GTPase-activating protein subfamily. *J Biol Chem.*, **273**, 26014-26025
48. Ishii, M., Kurachi, Y. (2003). Physiological actions of regulators of G protein signaling proteins. *Life Sci.*, **74**(2-3), 163-71.
49. Kach, J., Sethakorn, N., Dulin, N.O. (2012). A finer tuning of G-protein signaling through regulated control of RGS proteins. *Am J Physiol Heart Circ Physiol.*, **303**, H19-H35.
50. Rodríguez-Muñoz, M., Bermúdez, D., Sánchez-Blázquez, P., Garzón, J. (2007). Sumoylated RGS-Rz proteins act as scaffolds for Mu-opioid receptors and G-protein complexes in mouse brain. *Neuropsychopharmacology.* **32**(4), 842–850.
51. Garzón, J., Rodríguez-Muñoz, M., Vicente-Sánchez, A., et al. (2011). SUMO-SIM interactions regulate the activity of RGSZ2 proteins. *PLoS ONE*, **6**(12), e28557–e28557.
52. Popov, S. G., Krishna, U. M., Falck, J. R., and Wilkie, T. M. (2000). Ca<sup>2+</sup>/Calmodulin reverses phosphatidylinositol 3,4, 5-trisphosphate-dependent inhibition of regulators of G protein-signaling GTPase-activating protein activity. *J Biol Chem.*, **275**, 18962-18968.
53. Ishii, M., Fujita, S., Yamada, M., Hosaka, Y., and Kurachi, Y. (2005). Phosphatidylinositol 3,4,5-trisphosphate and Ca<sup>2+</sup>/calmodulin competitively bind to the regulators of G-protein-signalling (RGS) domain of RGS4 and reciprocally regulate its action. *Biochem J.*, **385**, 65-73
54. Rhee, S. G. (2001). Regulation of Phosphoinositide-Specific Phospholipase C. *Annu. Rev. Biochem.*, **70**, 281-312.
55. Bunney, T. D., Katan, M. (2011). PLC regulation: emerging pictures for molecular mechanisms. *Cell Press*, **36**(2), 88-96.
56. Smrcka, A. V., Brown, J. H., & Holz, G. G. (2012). Role of phospholipase Cε in physiological phosphoinositide signaling networks. *Cellular Signaling*, **24**(6), 1333–1343.
57. Gresset, A., Sondek, J., Harden, T. K. (2012). The phospholipase C isozymes and their regulation. *Subcell Biochem.* **58**, 61-94.
58. Kadamur, G., Ross, E. M. (2013). Mammalian Phospholipase C. *Annu. Rev. Physiol.* **75**, 127-154.
59. Nakamura, Y., Fukami, K. (2017). Regulation and physiological functions of mammalian phospholipase C. *J. Biochem.* **161**(4), 315-321.

60. Shibatohe, M., Kariya, K., Liao, Y., Hu, C., Watari, Y., Goshima, M., Shima, F., Kataoka, T. (1998). Identification of PLC210, a *Caenorhabditis elegans* Phospholipase C, as a putative effector of Ras. *J Biol Chem.*, **273**(11), 6218-6222.
61. Lyon, A.M., Begley, J.A., Manett, T.D. & Tesmer, J.J. (2014). Molecular Mechanisms of Phospholipase C beta3 Autoinhibition. *Structure*, **22**, 1844-1854.
62. Lyon, A.M., Dutta, S., Boguth, C.A., Skiniotis, G. & Tesmer, J.J. (2013). Full-length Galpha(q)-phospholipase C-beta3 structure reveals interfaces of the C-terminal coiled-coil domain. *Nat Struct Mol Biol.*, **20**, 355-62.
63. Lyon, A.M., Dutta, S., Boguth, C.A., Skiniotis, G. & Tesmer, J.J. (2013). Full-length Galpha(q)-phospholipase C-beta3 structure reveals interfaces of the C-terminal coiled-coil domain. *Nat Struct Mol Biol.*, **20**, 355-62.
64. Smrcka, A.V., Sternweis, P.C. (1993). Regulation of purified subtypes of phosphatidylinositol-specific phospholipase C beta by G protein alpha and beta gamma subunits. *J Biol Chem.*, **268**, 9667-9674.
65. Illenberger, D., Schwald, F., Pimmer, D., Binder, W., Maier, G., Dietrich, A., Gierschik, P. (1998). Stimulation of phospholipase C- $\beta$ 2 by the Rho GTPases Cdc42Hs and Rac1. *EMBO J.*, **17**, 6241-6249.
66. Gresset, A., Hick, S.N., Harden, T.K., Sondek, J. (2010). Mechanism of phosphorylation-induced activation of phospholipase C-gamma isozymes. *J Biol Chem.*, **285**(46), 35836-47.
67. Ferguson, K.M., Lemmon, M.A., Schlessinger, J., Sigler, P.B. (1995). Structure of the high-affinity complex of inositol trisphosphate with a phospholipase C pleckstrin homology domain. *Cell*, **83**, 1037-1046.
68. Nomikos, M., Mulgrew-Nesbitt, A., Pallavi, P., Mihalyne, G., Zaitseva, I., et al. (2007). Binding of phosphoinositide-specific phospholipase C- $\zeta$  (PLC- $\zeta$ ) to phospholipid membranes. *J Biol Chem.*, **282**, 16644-53.
69. Zhou, Y., Sondek, J., Harden, T.K. (2008). Activation of human phospholipase C- $\eta$ 2 by G $\beta\gamma$ . *Biochemistry*, **47**, 4410-17.
70. Zhang, L. et al. (2013). Phospholipase C epsilon hydrolyzes perinuclear phosphatidylinositol 4-phosphate to regulate cardiac hypertrophy. *Cell*, **153**, 216-27.
71. Dusaban, S. S., Brown, J. H. (2015). PLC $\epsilon$  mediated sustained signaling pathways. *Adv Biol Regul.*, **57**, 17-23.
72. Seifert, J.P., Wing, M.R., Snyder, J.T., Gershburg, S., Sondek, J., Harden, T.K. (2004). RhoA activates purified phospholipase C $\epsilon$  by a guanine nucleotide-dependent mechanism. *J Biol Chem.*, **279**(46), 47992-47997.

73. Seifert, J.P., Synder, J.T., Sondek, J., Harden, T.K. (2006). Direct activation of purified phospholipase C epsilon by RhoA studied in reconstituted phospholipid vesicles. *Methods Enzymol.*, **406**, 260-271.
74. Seifert, J.P., Zhou, Y., Hicks, S.N., Sondek, J., Harden, T.K. (2008). Dual activation of phospholipase C- $\epsilon$  by Rho and Ras GTPases. *J Biol Chem.*, **283**(44), 29690-29698.
75. Edamatsu H, Satoh T, Kataoka T. (2006). Ras and Rap1 activation of PLCepsilon lipase activity. *Methods Enzymol.*, **407**, 99-107.
76. Song, C., Satoh, T., Edamatsu, H., Wu, D., Tadano, M., Gao, X., Kataoka, T. (2002). Differential roles of Ras and Rap1 in growth factor-dependent activation of phospholipase C epsilon. *Oncogene*, **21**, 8105-8113.
77. Kelley, G.G., Reks, S.E., Ondrako, J.M. & Smrcka, A.V. (2001). Phospholipase C $\epsilon$ : a novel Ras effector. *EMBO J.*, **20**, 743-54.
78. Zhang, L., Malik, S., Kelley, G.G., Kapiloff, M.S., Smrcka, A.V. (2011). Phospholipase C scaffolds to muscle-specific A kinase anchoring protein (mAKAPb) and integrates multiple hypertrophic stimuli in cardiac myocytes. *J Biol Chem.*, **286**(26), 23012-23021.
79. Kelley, G.G., Reks, S.E. & Smrcka, A.V. (2004). Hormonal regulation of phospholipase C $\epsilon$  through distinct and overlapping pathways involving G<sub>12</sub> and Ras family G-proteins. *Biochem J.*, **378**, 129-39.
80. Yang, Y. R., Follo, M. Y., Cocco, L., Suh, P. (2013). The physiological roles of primary phospholipase C. *Adv Biol Regul.*, **53**, 232-241.
81. Ross, C.A., MacCumber, M.W., Glatt, C.E., Snyder, S.H. (1989). Brain phospholipase C isozymes: differential mRNA localizations by in situ hybridization. *Proc Natl Acad Sci U S A*, **86**, 2923-2927.
82. Takenawa, T., Homma, Y., Emori, Y. (1991). Properties of phospholipase C isozymes. *Methods Enzymol.*, **197**, pp. 511-518.
83. Hannan, A.J., Kind, P.C., Blakemore, C. (1998). Phospholipase C-beta1 expression correlates with neuronal differentiation and synaptic plasticity in rat somatosensory cortex. *Neuropharmacology*, **37**, pp. 593-605.
84. Kim, D., Jun, K.S., Lee, S.B., Kang, N.G., Min, D.S., Kim, Y.H., et al. (1997). Phospholipase C isozymes selectively couple to specific neurotransmitter receptors. *Nature*, **389**, 290-293.
85. Jang, H.J., Yang, Y.R., Kim, J.K., Choi, J.H., Seo, Y.K., Lee, Y.H., et al. (2013). Phospholipase C-gamma1 involved in brain disorders. *Adv Biol Regul.*, **53**, 51-62.

86. Fukami, K., Nakao, K., Inoue, T., Kataoka, Y., Kurokawa, M., Fissore, R.A., Nakamura, K., Katsuki, M., Mikoshiba, K., Yoshida, N., and Takenawa, T. (2001) Requirement of phospholipase Cdelta4 for the zona pellucida-induced acrosome reaction. *Science*, **292**, 920923.
87. Yoon, S.Y., Jellerette, T., Salicioni, A.M., Lee, H.C., Yoo, M.S., Coward, K., Parrington, J., Grow, D., Cibelli, J.B., Visconti, P.E., Mager, J., and Fissore, R.A. (2008). Human sperm devoid of PLC, zeta 1 fail to induce Ca(2+) release and are unable to initiate the first step of embryo development. *J Clin Invest.*, **118**, 36713681.
88. Takenaka, N., Edamatsu, H., Suzuki, N., Saito, H., Inoue, Y., Oka, M., Hu, L., and Kataoka, T. (2011). Overexpression of phospholipase Ce in keratinocytes upregulates cytokine expression and causes dermatitis with acanthosis and T-cell infiltration. *Eur J Immunol.*, **41**, 202213.
89. Hu, L., Edamatsu, H., Takenaka, N., Ikuta, S., and Kataoka, T. (2010). Crucial role of phospholipase Cepsilon in induction of local skin inflammatory reactions in the elicitation stage of allergic contact hypersensitivity. *J Immunol.*, **184**, 9931002.
90. Tyutyunnykova, A., Telegeev, G., Dubrovskaya, A. (2017). The controversial role of phospholipase c epsilon (PLCε) in cancer development and progression. *Journal of Cancer*. **8**(5), 716-729.
91. Song, C., Hu, C.D., Masago, M., Kariya, K., Yamawaki, Kataoka, Y., et al. (2001). Regulation of a novel human phospholipase C, PLCε, through membrane targeting by Ras. *J Biol Chem.*, **276**, 2752–57.
92. Lopez, I., Mak, E.C., Ding, J., Hamm, H.E., Lomasney, J.W. (2001). A novel bifunctional phospholipase C that is regulated by Gα12 and stimulates the Ras/mitogen-activated protein kinase pathway. *J Biol Chem.*, **276**, 2758–65.
93. Sorli, S.C., Bunney, T.D., Sugden, P.H., Paterson, H.F., Katan, M. (2005) Signaling properties and expression in normal and tumor tissues of two phospholipase C epsilon splice variants. *Oncogene*, **24**, 90-100.
94. Jin, T., Satoh, T., Liao, Y., Song, C., Gao, X., Kariya, K., Hu, C., Kataoka, T. (2001). Role of the CDC25 homology domain of phospholipase Ce in amplification of Rap1-dependent signaling. *J Biol Chem.*, **276**(32), 30301-30307.
95. Satoh, T., Edamatsu, H., Kataoka, T. (2006). Phospholipase Ce guanine nucleotide exchange factor activity and activation of Rap1. *Methods enzymol.*, **407**, 281-290.
96. Takai, Y., Sasaki, T., Matozaki, T. (2001). Small GTP-binding proteins. *Physiol Rev.*, **81**(1), 153-208.
97. Wing, M. R., Bourdon, D. M., Harden, T. K. (2003). PLC-ε: A Shared Effector Protein in Ras-, Rho-, and Gαβγ-Mediated Signaling. *Mol Interventions*, **3**(5), 273-280.

98. Bunney, T. D., Harris, R., Gandarillas, N. L., Josephs, M. B., Roe, S. M., Sorli, S.C., Paterson, H. F., Rodrigues-Lima, F., Esposito, D., Ponting, C.P., Gierschik, P., Pearl, L.H., Driscoll, P.C., Katan, M. (2006). Structural and mechanistic insights into ras association domains of phospholipase C epsilon. *Mol Cell*, **21**, 495-507.
99. Tappia, P.S., Singal, T. (2009) Regulation of phospholipase C in cardiac hypertrophy. *Clin Lipidol.*, **4**(1), 79-90.
100. Wang, H. et al. (2005). Phospholipase C  $\epsilon$  modulates  $\beta$ -adrenergic receptor-dependent cardiac contraction and inhibits cardiac hypertrophy. *Circ Res.*, **97**, 1305-13.
101. Oestreich, E.A. et al. (2009). Epac and phospholipase C  $\epsilon$  regulate  $\text{Ca}^{2+}$  release in the heart by activation of protein kinase C and calcium-calmodulin kinase II. *J Biol Chem.*, **284**, 1514-22.
102. Oestreich, E.A. et al. (2007). Epac-mediated activation of phospholipase C  $\epsilon$  plays a critical role in beta-adrenergic receptor-dependent enhancement of  $\text{Ca}^{2+}$  mobilization in cardiac myocytes. *J Biol Chem.*, **282**, 5488-95.
103. Nash, C.A., Brown, L.M., Malik, S., Cheng, X., Smrcka, A.V. (2018). Compartmentalized cyclic nucleotides have opposing effects on regulation of hypertrophic phospholipase C $\epsilon$  signaling in cardiac myocytes. *J Mol Cell Cardiol.*, **7**(121), 51-59.
104. Rubio, R.G., Ransom, R.F., Malik, S., Yule, D.I., Anantharam, A., Smrcka, A.V. (2018). Phosphatidylinositol 4-phosphate is a major source of GPCR-stimulated phosphoinositide production. *Sci Signal.*, **11**(547), 1-11.

## CHAPTER 2. HIGH-RESOLUTION STRUCTURE OF RGS17 SUGGESTS A ROLE FOR $\text{Ca}^{2+}$ IN PROMOTING THE GTPASE ACTIVATING PROTEIN ACTIVITY BY RZ SUBFAMILY MEMBERS

This research was originally published in the Journal of Biological Chemistry. Sieng, M., Hayes, M.P., O'Brien, J.B., Fowler, A.C., Houtman, J.C., Roman, D.L., Lyon, A.M. High-resolution structure of RGS17 suggests a role for  $\text{Ca}^{2+}$  in promoting the GTPase activating protein activity by RZ subfamily members. *J Biol Chem.* 2019; **294**(20): 8148-8160. © the American Society for Biochemistry and Molecular Biology. doi: 10.1074/jbc.RA118.006059

### 2.1 Abstract

Regulator of G protein signaling (RGS) proteins are negative regulators of G protein-coupled receptor (GPCR) signaling through their ability to act as GTPase-activating proteins (GAPs) for activated  $\text{G}\alpha$  subunits. Members of the RZ subfamily of RGS proteins bind to activated  $\text{G}\alpha_o$ ,  $\text{G}\alpha_z$ , and  $\text{G}\alpha_{i1-3}$  proteins in the nervous system and thereby inhibit downstream pathways, including those involved in  $\text{Ca}^{2+}$ -dependent signaling. In contrast to other RGS proteins, little is known about RZ subfamily structure and regulation. Herein, we present the 1.5 Å crystal structure of RGS17, the most complete and highest-resolution structure of an RZ subfamily member to date. RGS17 co-crystallized with  $\text{Ca}^{2+}$  bound to conserved positions on the predicted  $\text{G}\alpha$ -binding surface of the protein. Using NMR chemical shift perturbations, we confirmed that  $\text{Ca}^{2+}$  binds in solution to the same site. Furthermore, RGS17 had greater than a 55-fold higher affinity for  $\text{Ca}^{2+}$  than for  $\text{Mg}^{2+}$ , without changing its thermal stability. Finally, we found that  $\text{Ca}^{2+}$  promotes interactions between RGS17 and activated  $\text{G}\alpha$ , and decreases the  $K_m$  for GTP hydrolysis, potentially by altering the binding mechanism between these proteins. Taken together, these findings suggest that  $\text{Ca}^{2+}$  positively regulates RGS17, which may represent a general mechanism by which increased  $\text{Ca}^{2+}$  concentration promotes the GAP activity of the RZ subfamily, leading to RZ-mediated inhibition of  $\text{Ca}^{2+}$  signaling.

### 2.2 Introduction

G protein-coupled receptors (GPCRs) regulate many physiological processes in response to the binding of an extracellular ligand, leading to the activation of diverse pathways including vision and hormonal signaling. The intracellular response to ligand binding is mediated by

heterotrimeric G proteins, which consist of  $G\alpha$  and  $G\beta\gamma$  subunits. In the inactive state,  $G\alpha$  is bound to GDP and stably associates with  $G\beta\gamma$ . The activated GPCR is a guanine nucleotide exchange factor (GEF) for  $G\alpha$ , catalyzing the exchange of GDP for GTP.  $G\alpha\cdot$ GTP and  $G\beta\gamma$  dissociate from one another and bind downstream effector enzymes to stimulate second messenger production (1).  $G\alpha$  subunits are deactivated upon GTP hydrolysis, and reassociate with  $G\beta\gamma$ , terminating downstream signaling. However, the intrinsic rate of GTP hydrolysis for many  $G\alpha$  subunits is too slow to be physiologically relevant. This discrepancy led to the discovery of the regulator of G protein signaling (RGS) proteins, which are GTPase activating proteins (GAPs) for some classes of  $G\alpha$  subunits (2-5). RGS proteins increase the rate of GTP hydrolysis by binding to the switch regions of  $G\alpha\cdot$ GTP and stabilizing the transition state conformation (6).

Over twenty RGS proteins have been identified, and are subdivided into four families (R4, R7, R12, and RZ) based on sequence conservation and  $G\alpha$  subunit preference. All RGS proteins share the highly conserved RGS homology (RH) domain that is required for  $G\alpha\cdot$ GTP binding and hydrolysis (7,8). This domain is composed of terminal and bundle subdomains, which consist of the N- and C-termini and a four-helix bundle, respectively. Additional subfamily-specific domains or regions flanking the RH domain contribute to the subcellular localization of the RGS protein, the specificity, and affinity for the  $G\alpha\cdot$ GTP subunit, and/or participate in protein-protein interactions (9). The majority of RGS proteins act as GAPs for  $G\alpha_{i/o}$  and  $G\alpha_q$  subunits. However, some RGS proteins have narrower substrate specificity, such as RGS2 which preferentially binds  $G\alpha_q\cdot$ GTP, or broader substrate specificity, like the RZ subfamily which can also bind  $G\alpha_z\cdot$ GTP (9,10).

The RZ subfamily, comprised of RGS17 (RGSZ2), RGS19 (GAIP), and RGS20 (RGSZ1 or Ret-RGS) are among the simplest RGS proteins. These proteins consist of the RH domain flanked by short N- and C-termini. The N-terminus contains a highly conserved cysteine string that can be palmitoylated, as has been reported for RGS19, resulting in potential localization of these proteins to the plasma membrane (11,12). The defining feature of the RZ subfamily is the residue implicated in GAP activity. The R4, R7, and R12 subfamilies use a highly conserved asparagine residue (e.g. Asn128 in RGS4) to engage the switch regions of  $G\alpha$  (6,13,14). In contrast, the RZ family contains a serine at this position (9,13,14). Whether or how this serine recapitulates the interactions of the canonical asparagine residue in promoting GAP activity is not understood.

RGS17 is a potent regulator of cAMP and  $\text{Ca}^{2+}$  signaling and is expressed at highest levels in the cerebellum (10,15,16). It was first identified as a GAP for  $\text{G}\alpha_o$ , and subsequently also found to interact with  $\text{G}\alpha_z$  and  $\text{G}\alpha_{i1-3}$ . Thus, RGS17 increases cAMP accumulation by inhibition of  $\text{G}\alpha_{i/o}$ . RGS17 has also been reported to negatively regulate  $\text{Ca}^{2+}$  through a  $\text{G}\alpha_q$ -dependent mechanism (15). The preferred substrate of RGS17 is therefore likely dependent upon the cellular context (12). More recently, RGS17 has emerged as a promising therapeutic target in several cancers. RGS17 expression in non-neuronal tissues is linked to lung (17,18) and breast cancer (19), as well as hepatocellular carcinoma (20). The mechanistic role of RGS17 in these diseases is attributed to the increased cAMP driven by the inhibition of  $\text{G}\alpha_i$  signaling pathways (17). However, how RGS17 itself is regulated is unclear.

Herein, we present the 1.53 Å structure of RGS17, the most complete structure of an RZ family member, and the highest-resolution RGS structure reported to date. RGS17 crystallized as a dimer, with strong electron density observed for two  $\text{Ca}^{2+}$  atoms in each chain. One site is formed by the side chain of Glu109 and the backbone of Tyr106, which are situated on the face of RGS17 that is predicted to bind the switch regions of  $\text{G}\alpha\cdot\text{GTP}$ . This places the site in close proximity to Ser150, the RZ subfamily residue thought to be responsible for GAP activity, and which is analogous to RGS4 residue Asn128 (13,14). We confirmed that RGS17 binds  $\text{Ca}^{2+}$  at the Tyr106-Glu109 site in solution, and at a concentration significantly less than that used to obtain the crystal structure. Furthermore, we found that  $\text{Ca}^{2+}$  binds to RGS17 with over 50-fold higher affinity than  $\text{Mg}^{2+}$ . Finally, we found that while  $\text{Ca}^{2+}$  has no effect on the stability of RGS17 itself,  $\text{Ca}^{2+}$  enhances the ability of RGS17 to bind  $\text{G}\alpha_o\cdot\text{GTP}$ . These findings suggest that  $\text{Ca}^{2+}$  is a novel potentiator of RGS17 activity. As RGS17 is known to regulate  $\text{Ca}^{2+}$  signaling (10,15,16), this could represent a mechanism of feedback inhibition, wherein elevated  $\text{Ca}^{2+}$  promotes RGS17– $\text{G}\alpha$  interactions to terminate  $\text{G}\alpha$  signaling.

## 2.3 Results

### 2.3.1 Crystal Structure of RGS17 Bound to Calcium

RGS17 (residues 70-206) crystallized as an asymmetric dimer, with the final structure refined to 1.53 Å spacings (Figure 2.1, Table 2.1). The dimer is a crystallographic dimer, as RGS17 is monomeric in solution as determined by both size exclusion chromatography and NMR.

Continuous electron density as observed for residues 72-203 in chain A and 72-206 in chain X, but the two chains were otherwise essentially identical (r.m.s.d. of 0.11 Å for C $\alpha$  atoms in residues 72-203). Overall, the RGS17 RH domain is similar to that of other RGS proteins (7) and a previously determined structure of RGS17 (PDB ID 1ZV4 (21)). However, the two RGS17 structures differ from one another by 1.08 Å (C $\alpha$  atoms of residues 72-204), which is unexpected given their identical sequence. This arises primarily due to differences within the terminal subdomain and the orientation between the terminal and bundle subdomains of the RH domain (Figure 2.2). Superimposing the bundle subdomains from this structure and 1ZV4 confirms the bundle subdomain is highly similar, with an r.m.s.d. of 0.52 Å for the C $\alpha$  atoms of residues 106-186. In contrast, superimposing the RGS17 structures over their terminal subdomains results in an r.m.s.d. of 0.86 Å for the C $\alpha$  atoms of residues 72-105 and 187-206. In addition, the terminal subdomain of our RGS17 structure is rotated by  $\sim 17^\circ$  with respect to its orientation in the 1ZV4 structure (Figure 2.2) (22).

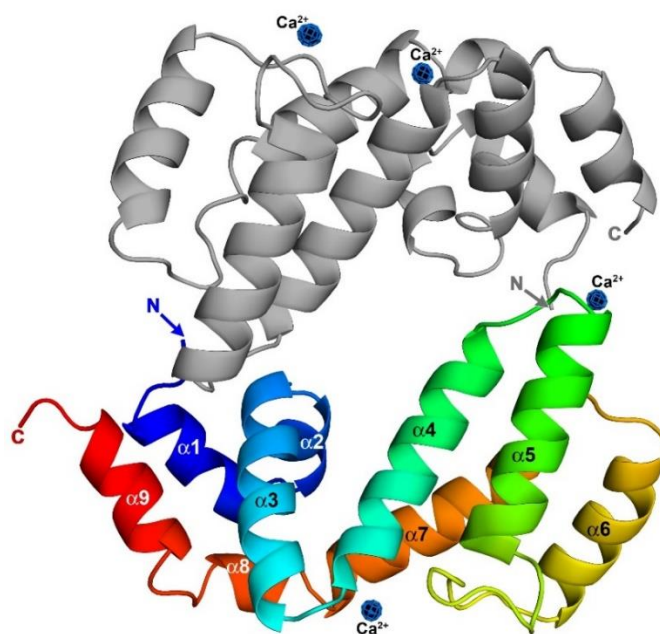


Figure 2.1. Crystal structure of RGS17 in complex with Ca $^{2+}$ . RGS17 crystallized as a dimer, but is monomeric in solution, as determined by SEC and NMR. Chain X is shown color-ramped from blue at the N-terminus to red at the C-terminus. Chain A is shown in gray, and the r.m.s.d. between chains is 0.6 Å. Strong electron density was observed for four Ca $^{2+}$  ions (black spheres). The  $10 \sigma |F_o| - |F_c|$  omit map for the Ca $^{2+}$  ions are shown as blue cages, and electron density for these ions persists beyond  $20 \sigma$ .

Table 2.1 RGS17 Data Collection and Refinement Statistics.

<b>Data Collection</b>	
X-ray source	LS-CAT 21-ID-D
Wavelength (Å)	1.068 Å
D <sub>min</sub> (Å)	30.0 – 1.53 (1.56-1.53)
Space group	<i>P</i> 12 <sub>1</sub> 1
Cell dimensions	
a, b, c (Å)	39.6, 59.3, 65.2
α, β, γ (°)	90, 100.6, 90
Total reflections	190,012
Unique reflections	39,255
R <sub>sym</sub> (%)	13.2 (66.5%)
Completeness (%)	87.5 (41.4)
( <i>I</i> /σ)	10.52 (6.95)
Redundancy	4.8 (1.7)
( <i>CC</i> <sub>1/2</sub> )	(0.58)
<b>Refinement</b>	
Refinement resolution (Å)	30.0 – 1.53 (1.56-1.53)
Total reflections used	37,292
RMSD bond lengths (Å)	0.009
RMSD bond angles (°)	1.31
Estimated coordinate error (Å)	0.103
Ramachandran plot	
Favored (%)	98.5
Outliers (%)	0.0
R <sub>work</sub> /R <sub>free</sub> (%)	20.3/22.5
Protein atoms	2,275
Ligand atoms	39
Solvent molecules	293
Average B-factor (Å <sup>2</sup> )	18.0
Protein	16.7
Ligand	37.2
Solvent	28.2
Wilson B factor (Å <sup>2</sup> )	12.9
PDB entry	6AM3

Values in parentheses correspond to the highest resolution data shell.

*CC*<sub>1/2</sub> is the Pearson correlation coefficient

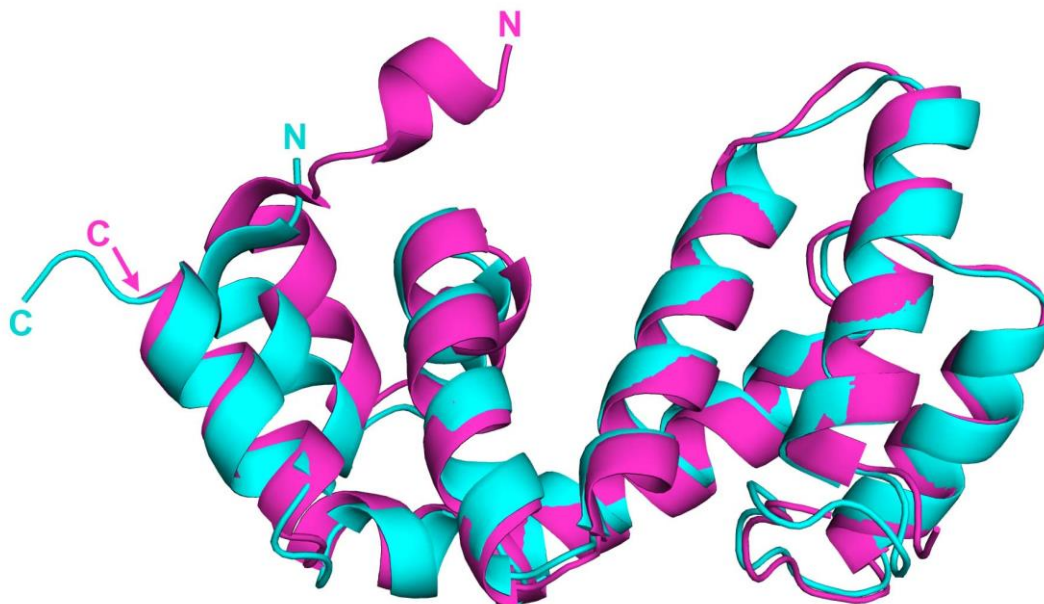


Figure 2.2. Superposition of RGS17 and 1ZV4 (21). The bundle subdomains of RGS17·Ca<sup>2+</sup> (cyan, chain X) and 1ZV4 (fuchsia) (21) have an r.m.s.d. of 0.52 Å for the C $\alpha$  atoms. The RGS17·Ca<sup>2+</sup> terminal subdomain is rotated ~17° from the bundle subdomain with respect to their orientation in the 1ZV4 structure. The N- and C- termini of the proteins are labeled N and C. The 1ZV4 structure includes residues 66-143 and 146-204.

Each chain of RGS17 in the crystal structure also contained strong electron density consistent with bound Ca<sup>2+</sup>, which was present in the crystallization conditions as 200 mM CaCl<sub>2</sub>. Each RGS17 chain coordinated two Ca<sup>2+</sup> atoms, but only one site is conserved between the two chains. This site, located in the loop connecting helices  $\alpha$ 3 and  $\alpha$ 4, coordinates Ca<sup>2+</sup> through the side chain of Glu109 and the backbone carbonyl oxygen of Tyr106, with the rest of the Ca<sup>2+</sup> coordination sites occupied by five water molecules (Figure 2.3A, B). These Ca<sup>2+</sup> are tightly bound, as electron density is still observed when the  $|F_o|-|F_c|$  omit map is contoured to 20  $\sigma$  (Figure 2.1). This Ca<sup>2+</sup> ion is on the same face of RGS17 that is predicted to interact with the switch regions of G $\alpha$ ·GTP and is ~11 Å from Ser150 (3,23,24). Thus, the Ca<sup>2+</sup> ion is positioned to potentially modulate the interactions between RGS17 and its cognate G $\alpha$ ·GTP.

Each RGS17 chain in the crystal structure also contains strong electron density for a second Ca<sup>2+</sup> ion. However, these secondary sites are not conserved between the two chains. In chain A, a Ca<sup>2+</sup> ion is coordinated by the side chain of Glu148 and the carbonyl oxygen of Ile143, with the remaining coordination sites occupied by three water molecules (Figure 2.3B). This site is located

in the loop connecting helices  $\alpha 5$  and  $\alpha 6$ , on the predicted  $G\alpha$  binding surface and in close proximity to both Ser150 ( $\sim 10\text{\AA}$ ) and the  $\text{Ca}^{2+}$  site formed by Tyr106 and Glu109 (Figure 2.3B). In Chain X, a  $\text{Ca}^{2+}$  is coordinated by the backbone carbonyl oxygen of Gln124, located in the loop connecting helices  $\alpha 4$  and  $\alpha 5$ , along with three water molecules that complete the coordination of  $\text{Ca}^{2+}$  (Figure 2.3C). While this  $\text{Ca}^{2+}$  is near the dimer interface and the N- and C-termini of Chain A, it does not contribute to the dimer interface or interact with any residues in Chain A. For both of these sites (Ile143-Glu148 and Gln124), the  $\text{Ca}^{2+}$  ions are tightly bound, as electron density is visible when the  $|F_o|-|F_c|$  omit map is contoured to  $20\sigma$ .

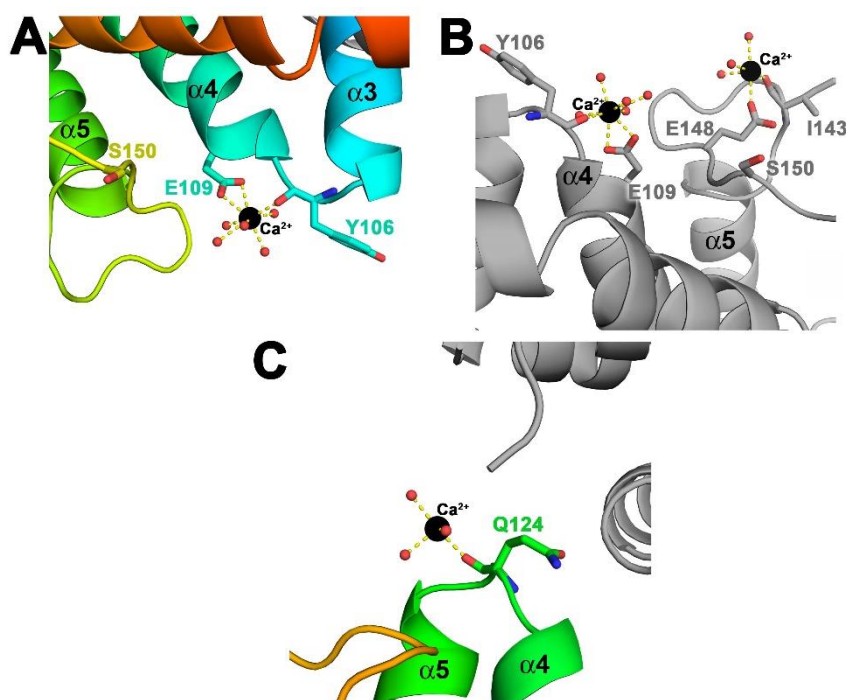


Figure 2.3. The crystallographic RGS17 dimer coordinates four  $\text{Ca}^{2+}$  ions. RGS17 chains are colored as in Figure 2.1.  $\text{Ca}^{2+}$  ions are shown as black spheres, waters as red spheres, and the distance between the  $\text{Ca}^{2+}$  ion and the coordinating atoms are shown in dashed yellow lines. All coordination distances are between 2.3 - 2.6  $\text{\AA}$ . (A) The backbone carbonyl oxygen of Tyr106 and side chain of Glu109 in the  $\alpha 3$ - $\alpha 4$  loop coordinate one  $\text{Ca}^{2+}$  ion in chain X. This is in close proximity to Ser150, the GAP residue in the RZ subfamily. (B) As observed in (A), the RGS17 A chain also coordinates  $\text{Ca}^{2+}$  via Tyr106 and Glu109. A second  $\text{Ca}^{2+}$  is bound by the backbone carbonyl of Ile143 and side chain of Glu148 in the  $\alpha 5$ - $\alpha 6$  loop. (C) The carbonyl oxygen of Gln124, located in the  $\alpha 4$ - $\alpha 5$  loop, coordinates a  $\text{Ca}^{2+}$  ion in chain X.

### 2.3.2 RGS17 Binds $\text{Ca}^{2+}$ and $\text{Mg}^{2+}$ in Solution

RGS17 and other RGS proteins have not previously been reported to directly bind  $\text{Ca}^{2+}$  or other divalent cations. One possible explanation for the presence of bound  $\text{Ca}^{2+}$  in our RGS17 structure is that it is an artifact due to the presence of 200 mM  $\text{CaCl}_2$  in the crystallization conditions. To establish whether RGS17 binds  $\text{Ca}^{2+}$  in solution, we used nuclear magnetic resonance (NMR) to monitor changes in the  $^1\text{H}$ - $^{15}\text{N}$  2D HSQC spectrum of RGS17 in the presence of 15 mM  $\text{CaCl}_2$ . In this spectrum, protons that are directly bound to  $^{15}\text{N}$  are detected, providing a “fingerprint” of the amide backbone of the protein. To assign each peak in the  $^1\text{H}$ - $^{15}\text{N}$  HSQC spectra, the protein backbone and  $\text{C}\beta$  carbons were first assigned using  $^{13}\text{C}$ - and  $^{15}\text{N}$ -labelled RGS17 and standard triple resonance experiments.

If RGS17 binds  $\text{Ca}^{2+}$  in solution,  $\text{Ca}^{2+}$  will alter the local chemical environment, causing perturbations in the chemical shifts of the amide proton and/or nitrogen of residues in close proximity to the bound ion. In contrast, residues that are distant from the site of binding and/or unaffected by  $\text{Ca}^{2+}$  addition will not have significantly perturbed chemical shifts relative to the  $^1\text{H}$ - $^{15}\text{N}$  HSQC spectrum of the protein alone. Addition of 15 mM  $\text{CaCl}_2$  to  $^{15}\text{N}$ -labelled RGS17 caused significant chemical shift perturbations (CSPs) for residues Ser107 (0.178 ppm), Glu108 (0.160 ppm), Glu109 (0.065 ppm) and Asn110 (0.096 ppm) ( $> 2$  S.D. from the average CSP of all residues, which is 0.059 ppm) (Figure 2.4). These residues are adjacent to Tyr106 and Glu109, the residues that directly bind  $\text{Ca}^{2+}$  in both chains of the crystal structure. A modest shift perturbation was also observed for Tyr106 (0.019 ppm).

The other  $\text{Ca}^{2+}$  ions observed in the crystal structure are coordinated by the backbone carbonyl of Ile143 and sidechain of Glu148 in Chain A, or by the backbone carbonyl of Gln124 in Chain X. Val149 displays significant perturbation (0.141 ppm), and a CSP for Ser145 was obtained that was just below the 2 S.D. cutoff (0.058 ppm). However, other residues adjacent to this location could not be definitively assigned in the triple resonance experiments. Similarly, definitive measurement of the CSP for Gln124 was not possible due to spectral overlap. However, minimal shift perturbations were observed for the adjacent residues Glu123 and Asn125 (Figure 2.4). Taken together, these findings suggest that the sites formed by Tyr106/ Glu109 and Ile143/Glu148 are most likely the preferred binding sites for  $\text{Ca}^{2+}$ , even at concentrations an order of magnitude lower than that used in crystallization (15 mM vs. 200 mM  $\text{CaCl}_2$ ).

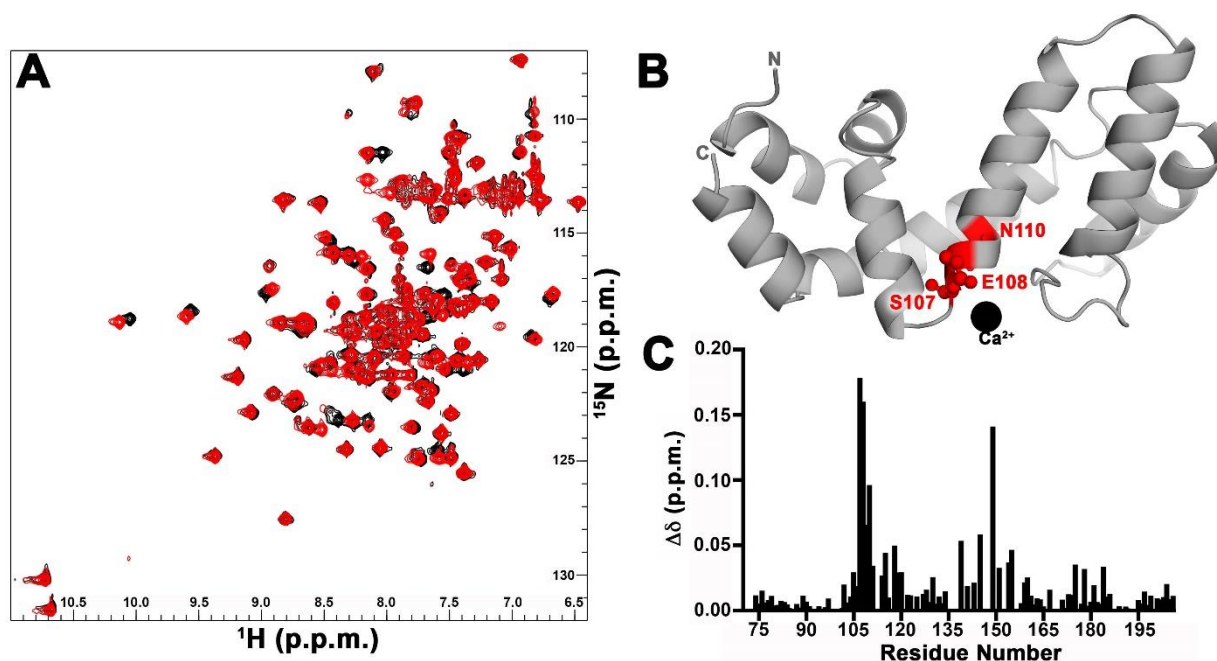


Figure 2.4. RGS17 binds  $\text{Ca}^{2+}$  in solution. (A)  $^1\text{H}$ - $^{15}\text{N}$  2D HSQC spectra of RGS17 alone (black) or upon addition of 15 mM  $\text{CaCl}_2$  (red). (B) Structure of RGS17 where residues that display chemical shift perturbations greater than 0.15 ppm are shown as ball-and-stick in red.  $\text{Ca}^{2+}$  is shown as a black sphere. (C) Table of CSPs for all the residues that could be assigned in the  $^1\text{H}$ - $^{15}\text{N}$  2D HSQC spectra for RGS17.

We next tested whether another divalent cation could bind to the same site(s) on RGS17, or if the interaction is unique to  $\text{Ca}^{2+}$ . We assessed the ability of  $\text{Mg}^{2+}$  to bind RGS17, given its relative abundance in cells. Addition of 15 mM  $\text{MgCl}_2$  to  $^{15}\text{N}$ -labelled RGS17 resulted in a significant CSP ( $> 2$  S.D. from average, 0.017 ppm) for Ser108 (0.024 ppm) (Figure 2.5), similar to the CSP observed in the presence of  $\text{Ca}^{2+}$ . Ser107 (0.022 ppm) and Glu109 (0.072 ppm) also displayed substantial shifts, consistent with  $\text{Mg}^{2+}$  also binding to this site in RGS17. 15 mM  $\text{MgCl}_2$  addition induced CSPs in a second group of residues including Val149 (0.031 ppm), Tyr140 (0.024 ppm), and Ser150 ( $>0.023$  ppm), located in helix  $\alpha_5$  and the  $\alpha_5$ - $\alpha_6$  loop (Figure 2.5). These residues are adjacent to or in close proximity to Ile143 and Glu148, which coordinate a second  $\text{Ca}^{2+}$  site in Chain A of the crystal structure (Figure 2.1, 2.3), and which display altered chemical shifts in the presence of  $\text{Ca}^{2+}$  (Figure 2.4).

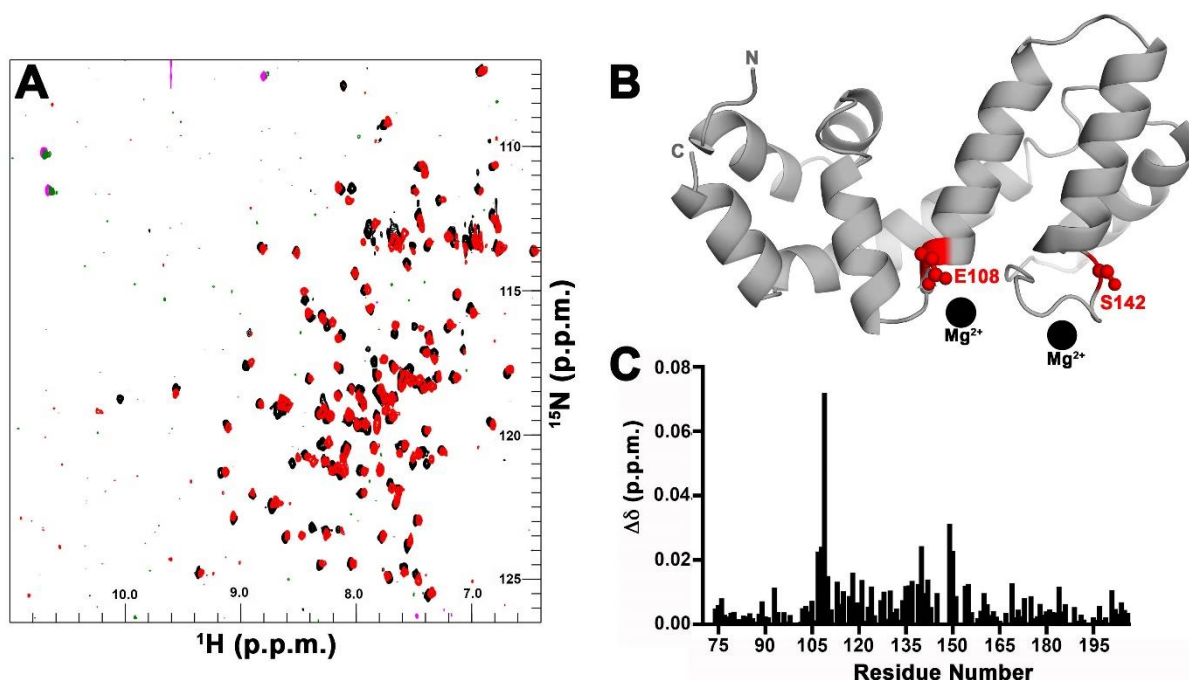


Figure 2.5. RGS17 binds  $\text{Mg}^{2+}$  in solution. (A)  $^1\text{H}$ - $^{15}\text{N}$  2D HSQC spectra of RGS17 alone (black) or upon addition of 15 mM  $\text{MgCl}_2$  (red). (B) Structure of RGS17 where residues with CSPs greater than 0.15 ppm are shown in ball-and-stick in red. In contrast to spectra obtained in the presence of  $\text{CaCl}_2$ ,  $\text{MgCl}_2$  induces CSPs in two regions of RGS17. The locations of the  $\text{Mg}^{2+}$  ions (black spheres) are modeled based on the location of  $\text{Ca}^{2+}$  atoms observed in the RGS17- $\text{Ca}^{2+}$  crystal structure. (C) Table of CSPs for all the residues that could be assigned in the  $^1\text{H}$ - $^{15}\text{N}$  2D HSQC spectra for RGS17.

These results demonstrate that both  $\text{Ca}^{2+}$  and  $\text{Mg}^{2+}$  bind directly to RGS17 in solution through a site formed by the backbone carbonyl of Tyr106 and the side chain of Glu109. This site is also the only  $\text{Ca}^{2+}$  binding site that occurs in both chains in the crystal structure. While secondary  $\text{Ca}^{2+}$  binding sites are observed within each chain of the crystal structure, the only other site in which significant CSPs could be reliably observed was the site formed by the backbone carbonyl of Ile143 and the side chain of Glu148. This second site may be less favorable for cation binding, given that only one RGS17 chain has  $\text{Ca}^{2+}$  bound in this site in the crystal structure. Finally, we also found no evidence that the binding of divalent cations impacts the thermal stability of RGS17 as determined by differential scanning fluorimetry (Figure 2.6, Table 2.2).

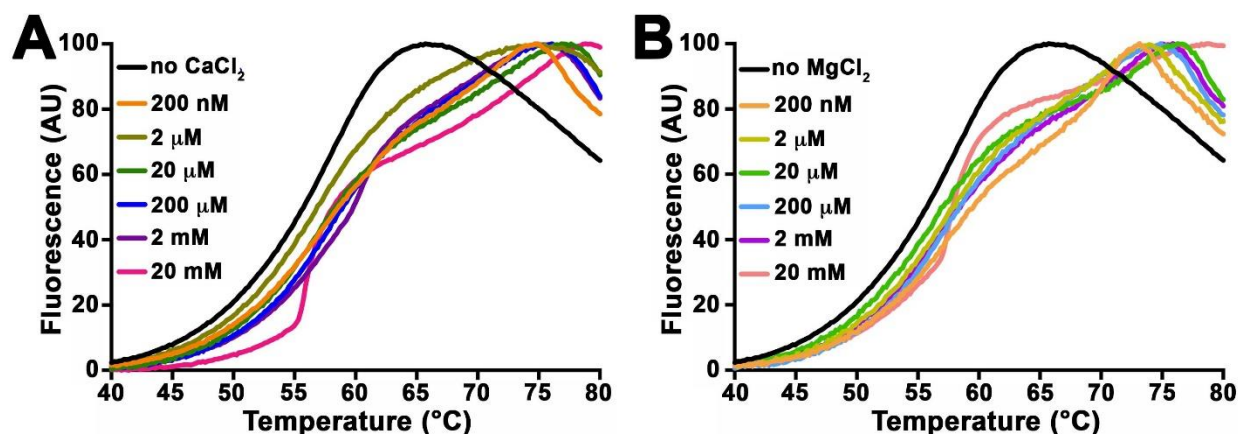


Figure 2.6. RGS17 is not significantly thermally stabilized by the addition of  $\text{CaCl}_2$  or  $\text{MgCl}_2$ . Differential scanning fluorimetry (DSF) was used to determine whether the binding of  $\text{Ca}^{2+}$  or  $\text{Mg}^{2+}$  perturbed the melting temperature ( $T_m$ ) of RGS17. RGS17 was incubated with a fluorescent dye and increasing concentrations of  $\text{CaCl}_2$  or  $\text{MgCl}_2$ , and the sample heated. As RGS17 denatures, the dye fluoresces, and the inflection point of the curve corresponds to the  $T_m$ .

Table 2.2 Thermal Stability of RGS17

	<b>RGS17</b> ( $T_m \pm \text{S.E.M.}$ )	<b>+ <math>\text{CaCl}_2</math></b> ( $T_m \pm \text{S.E.M.}$ )	<b>+ <math>\text{MgCl}_2</math></b> ( $T_m \pm \text{S.E.M.}$ )
protein only	$55.3 \pm 0.346$		
+ 200 nM		$56.1 \pm 0.63$	$58.3 \pm 0.87$
+ 2 $\mu\text{M}$		$58.0 \pm 1.14$	$56.9 \pm 0.80$
+ 20 $\mu\text{M}$		$56.3 \pm 1.07$	$56.1 \pm 1.05$
+ 200 $\mu\text{M}$		$58.2 \pm 1.21$	$57.9 \pm 1.07$
+ 2 mM		$57.3 \pm 0.566$	$59.5 \pm 1.44$
+ 20 mM		$51.7 \pm 0.189$	$55.5 \pm 1.07$

### 2.3.3 RGS17 has Higher Affinity for $\text{Ca}^{2+}$ than $\text{Mg}^{2+}$

Having demonstrated that RGS17 can bind both  $\text{Ca}^{2+}$  and  $\text{Mg}^{2+}$  at multiple sites, we next determined the affinity of RGS17 for these ions. Using NMR, we observed concentration-dependent changes in CSP for both ions, and the magnitude of CSPs induced by  $\text{Ca}^{2+}$  binding was greater than those observed upon  $\text{Mg}^{2+}$  binding (Figure 2.7). We determined the  $K_D$  for  $\text{Ca}^{2+}$  and  $\text{Mg}^{2+}$  for each residue that displayed a significant CSP upon the addition of the divalent cation. The CSP was fit as a function of ion concentration to a one-site binding model. For the binding site created by Tyr106 and Glu109, the dissociation constants of  $\text{Ca}^{2+}$  ranged from 98  $\mu\text{M}$  (35-197, 95% CI) for Glu109 to 181  $\mu\text{M}$  (98-296, 95% CI) for Glu108. Averaging the  $K_D$  values obtained

for residues 107-110 in the presence of  $\text{Ca}^{2+}$  yielded a  $K_{D, \text{avg}}$  of  $132 \pm 35 \mu\text{M}$ . A similar  $K_{D, \text{avg}}$  of  $91 \pm 6 \mu\text{M}$  was observed for the binding site near Ile143 and Glu148 through the analysis of Ser145, which had a  $K_D$  of  $86 \mu\text{M}$  (31-172, 95% CI) and Val149, which had a  $K_D$  of  $95 \mu\text{M}$  (37-182, 95% CI).

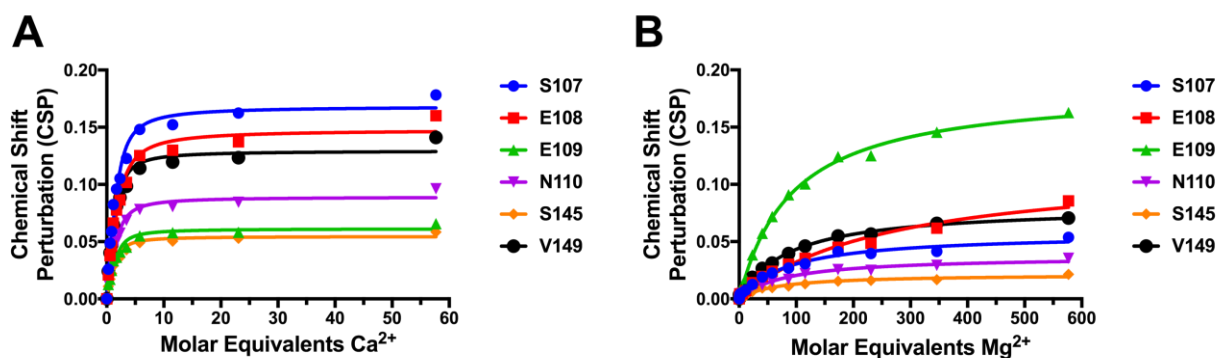


Figure 2.7. RGS17 binds  $\text{Ca}^{2+}$  with higher affinity than  $\text{Mg}^{2+}$ . The  $K_{D, \text{avg}}$  for  $\text{Ca}^{2+}$  and  $\text{Mg}^{2+}$  binding to RGS17 was determined for each amino acid that displayed a significant CSP upon the addition of divalent cation. Two cation binding sites were identified on RGS17, one formed by Tyr106 and Glu109, and a secondary site formed by Ile143 and Glu148. Residues adjacent to these binding sites that displayed CSPs  $> 2$  S.D. greater than the average CSP were used to calculate the  $K_{D, \text{avg}}$  for each site by fitting the CSP as a function of ion concentration to a one-site binding model. (A) CSP as a function of increasing  $\text{Ca}^{2+}$  concentration. The  $K_{D, \text{avg}}$  for residues Ser107, Glu108, Glu109, and Asn110 is  $132 \pm 35 \mu\text{M}$ , and the  $K_{D, \text{avg}}$  for residues Ser145 and Val149 is  $91 \pm 6 \mu\text{M}$ . (B) CSP as a function of increasing  $\text{Mg}^{2+}$  concentration. The  $K_{D, \text{avg}}$  for residues Ser107, Glu108, Glu109, and Asn110 is  $34 \pm 23 \text{mM}$ , and the  $K_{D, \text{avg}}$  for residues Ser145 and Val149 is  $20 \pm 4 \text{mM}$ .

Titration of RGS17 with increasing concentrations of  $\text{Mg}^{2+}$  revealed that RGS17 had much lower affinity for this metal at both sites examined. For the binding site formed by Tyr106 and Glu109, the  $K_{D, \text{avg}}$  was only  $34 \pm 23 \text{mM}$ , with individual residues exhibiting  $K_D$  values ranging from  $21 \text{mM}$  (13-38, 95% CI) for Asn110 to  $68 \text{mM}$  (45-104, 95% CI) for Glu108. The binding site formed by Ile143 and Glu148 also displayed a lower affinity for  $\text{Mg}^{2+}$ , where the  $K_{D, \text{avg}}$  was  $20 \pm 4 \text{mM}$ . Ser145 alone had a  $K_D$  of  $17 \text{mM}$  (12-25, 95% CI) and Val149 had a  $K_D$  of  $22 \text{mM}$  (20-25, 95% CI). Thus, RGS17 has 257-fold and 219-fold higher affinity for  $\text{Ca}^{2+}$  than  $\text{Mg}^{2+}$  at the sites formed by Tyr106 and Glu109 and Ile143 and Glu148, respectively.

### 2.3.4 RGS17 Binds Cations with Higher Affinity than RGS4 or RGS2

The RH domain is highly conserved across the RGS family, including the residues we have shown to bind cations in RGS17. Additionally, as some of the interactions are mediated by the peptide backbone, it is possible that all RGS proteins bind cations in solution. We used NMR spectroscopy to determine whether RGS4 and RGS2 bind  $\text{Ca}^{2+}$  and/or  $\text{Mg}^{2+}$  in solution. RGS4 and RGS2 share 40% and 38% identity with RGS17 across the RH domain and are well characterized with respect to their structure and regulation (7) (Figure 2.8, 2.9).

The spectrum of RGS4 has been fully assigned (25), allowing us to identify amino acids that show CSPs upon the addition of  $\text{Ca}^{2+}$  or  $\text{Mg}^{2+}$ . Using the same approach as described for RGS17, the  $^1\text{H}$ - $^{15}\text{N}$  HSQC spectrum of RGS4 was obtained alone and in the presence of a 40-fold molar excess of  $\text{CaCl}_2$  or  $\text{MgCl}_2$ . Similar to RGS17, two regions of RGS4 showed significant CSPs ( $> 2$  S.D. from average, 0.019 ppm in the presence of  $\text{Ca}^{2+}$ , or 0.006 ppm in the presence of  $\text{Mg}^{2+}$ ). The first region corresponds to the cation binding site formed by Tyr106 and Glu108 in RGS17 (Tyr84 and Glu86 in RGS4). In the presence of  $\text{Ca}^{2+}$ , RGS4 residues Tyr84 (0.056 ppm), Ser85 (0.206 ppm), Glu86 (0.291 ppm), Glu87 (0.043 ppm), Asn88 (0.081 ppm), and Ile89 (0.115 ppm) all show significant CSPs. The second site is equivalent to the site formed by RGS17 Ile143 and Glu148 (RGS4 Val121 and Glu126), with significant CSPs observed for residues Ala123 (0.019 ppm), Lys125 (0.066 ppm), and Val127 (0.056 ppm). The  $K_{D, \text{avg}}$  for these binding sites for  $\text{Ca}^{2+}$  was calculated as a function of ion concentration using a one-site binding model. For the site encompassing residues Tyr84, Ser85, Glu86, Glu87, Asn88, and Ile89 the calculated  $K_{D, \text{avg}}$  was  $9.6 \pm 3$  mM, while the  $K_{D, \text{avg}}$  for the site associated with residues Ala123, Lys125, and Val127 was  $6.1 \pm 1.6$  mM. Thus, the RGS4  $K_{D, \text{avg}}$  for  $\text{Ca}^{2+}$  at the two sites are 72-fold and 67-fold lower than those calculated for RGS17 (Figure 2.8B).

RGS4 also had decreased affinity for  $\text{Mg}^{2+}$ . The putative cation binding site formed by residues Tyr84 and Glu86 showed significant CSPs for residues Ser85 (0.014 ppm), Glu86 (0.033 ppm), Glu87 (0.021 ppm), and Asn88 (0.011 ppm) (Figure 2.8C). However, the  $K_{D, \text{avg}}$  for this site was  $93 \pm 193$  mM. The RGS4 site likely formed by Val121 and Glu126 showed significant CSPs for residues Ala123 (0.022 ppm) and Lys125 (0.027 ppm), with a calculated  $K_{D, \text{avg}}$  of  $90 \pm 75$  mM (Figure 2.8D). Thus, RGS4 has ~10-15-fold lower affinity for  $\text{Mg}^{2+}$  relative to  $\text{Ca}^{2+}$  and binds both cations weaker than RGS17.

The ability of RGS2 to bind  $\text{Ca}^{2+}$  and  $\text{Mg}^{2+}$  in solution was then tested. The NMR spectrum of RGS2 has not been assigned, and thus the  $^1\text{H}$ - $^{15}\text{N}$  HSQC spectra of RGS2 was compared to spectra obtained with increasing concentrations of  $\text{CaCl}_2$  or  $\text{MgCl}_2$  (Figure 2.9). Addition of 20- or 250-fold molar excess of  $\text{CaCl}_2$  to  $^{15}\text{N}$ -labelled RGS2 caused few changes in the  $^1\text{H}$ - $^{15}\text{N}$  HSQC spectra (Figure 2.9A). This is consistent with RGS2 binding weakly to  $\text{Ca}^{2+}$  in solution. Similarly, the addition of up to 500-fold molar excess of  $\text{MgCl}_2$  to  $^{15}\text{N}$ -labelled RGS2 had essentially no impact on the  $^1\text{H}$ - $^{15}\text{N}$  HSQC spectra (Figure 2.9B), demonstrating that RGS2 binds  $\text{Mg}^{2+}$  very weakly under these experimental conditions.

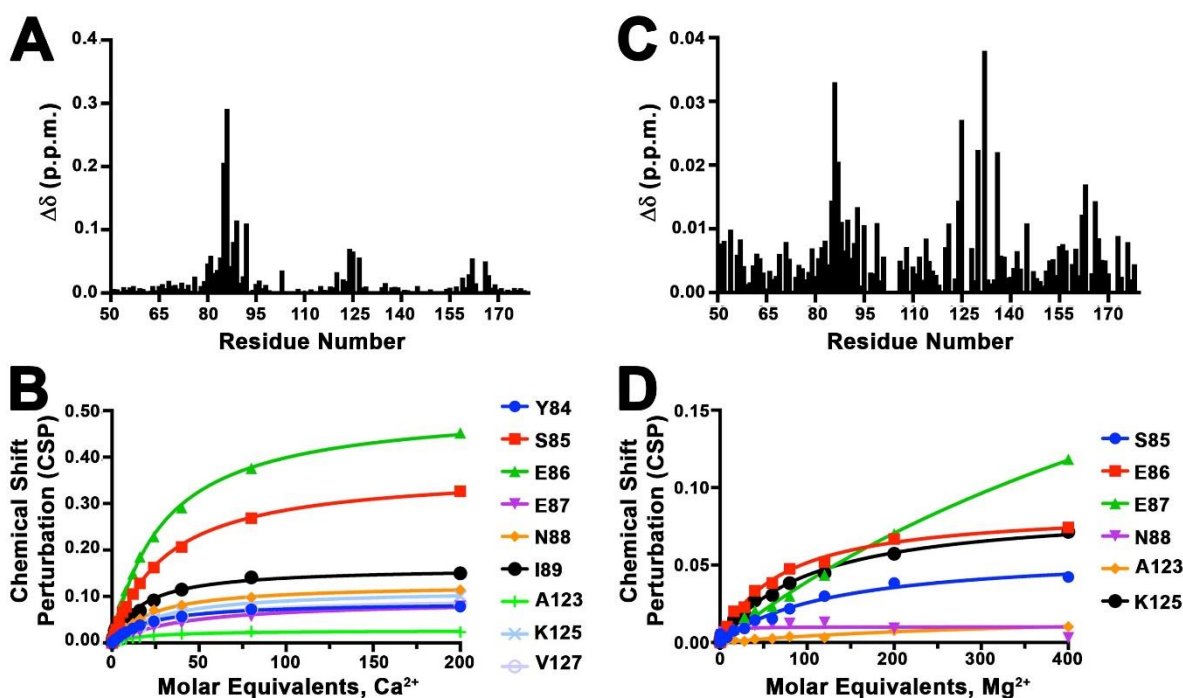


Figure 2.8. RGS4 binds  $\text{Ca}^{2+}$  weakly but does not bind  $\text{Mg}^{2+}$ . RGS4 shares 40% sequence identity with RGS17, including the residues that bind cations in RGS17. In RGS4, these sites contain Y84 and E86 (RGS17 Y106 and E109), and V121 and E126 (RGS17 I143 and E148). (A) Table of CSPs for all residues that could be assigned in the  $^1\text{H}$ - $^{15}\text{N}$  2D HSQC spectra of RGS4 (25) upon addition of 40-fold molar excess  $\text{CaCl}_2$ . (B) Residues including and adjacent to the putative cation binding sites in RGS4 that displaced CSPs  $> 2$  S.D. greater than the average CSP were used to calculate the  $K_{D,\text{avg}}$  for each site by fitting the CSP as a function of ion concentration to a one-site binding model. CSP as a function of increasing  $\text{Ca}^{2+}$  concentration. The  $K_{D,\text{avg}}$  for residues Y84, S85, E86, E87, N88, and I89 is  $9.6 \pm 3$  mM, and the  $K_{D,\text{avg}}$  for residues A123, K125, and V127 is  $6.1 \pm 1.6$  mM. (C) Table of CSPs for all residues assigned in the  $^1\text{H}$ - $^{15}\text{N}$  2D HSQC spectra of RGS4 upon addition of 40-fold molar excess  $\text{MgCl}_2$ . (D) CSP as a function of increasing  $\text{Mg}^{2+}$  concentration. The  $K_{D,\text{avg}}$  for residues S85, E86, E87, and N88 is  $93 \pm 193$  mM, and the  $K_{D,\text{avg}}$  for residues A125 and K125 is  $90 \pm 75$  mM.

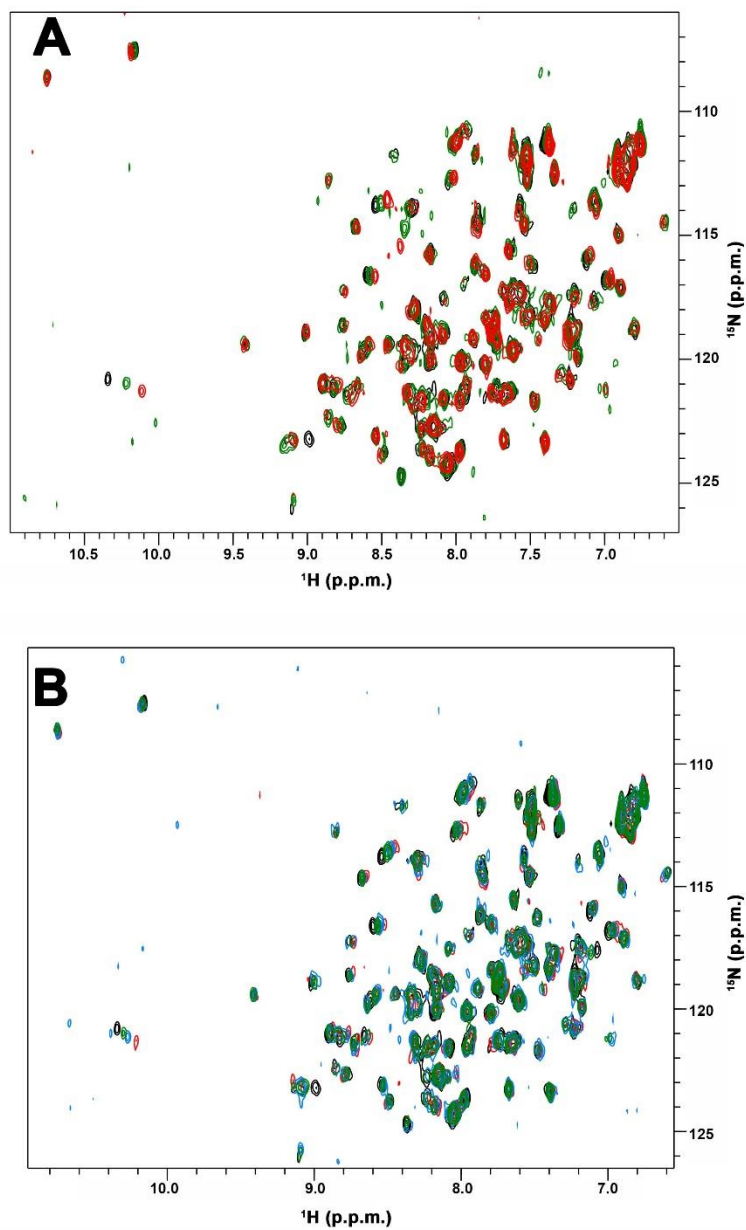


Figure 2.9.  $^1\text{H}$ - $^{15}\text{N}$  spectra of RGS2 in the presence of  $\text{CaCl}_2$  or  $\text{MgCl}_2$ . (A)  $^1\text{H}$ - $^{15}\text{N}$  2D HSQC spectra of RGS2 alone (black) and upon addition of 20 (green) or 250 molar excess of  $\text{CaCl}_2$  (red). (B)  $^1\text{H}$ - $^{15}\text{N}$  2D HSQC spectra of RGS2 alone (black) and upon addition of 100 (green), 250 (blue), or 500 molar excess  $\text{MgCl}_2$  (red).

### 2.3.5 Calcium Enhances Interactions Between RGS17 and Activated $G\alpha_o$

The binding sites for  $Ca^{2+}$  and  $Mg^{2+}$  on RGS17 are located on the same face of the protein predicted to interact with activated  $G\alpha$  subunits (6,14,15) and is in close proximity to the putative GAP residue, Ser150. To determine whether  $Ca^{2+}$  impacts the ability of RGS17 to bind activated  $G\alpha_o$ , an AlphaScreen protein interaction assay (26) was used to quantify association. Briefly, RGS17 was biotinylated and immobilized on streptavidin-coated donor beads, while activated GST-tagged  $G\alpha_o \cdot GDP \cdot AIF_4$  was immobilized on anti-GST acceptor beads. RGS17– $G\alpha_o$  binding was quantified as an increase in bead-based fluorescence. RGS17 binds activated  $G\alpha_o$  in a concentration-dependent manner, with saturation occurring at approximately 5 nM  $G\alpha_o \cdot GDP \cdot AIF_4$  (Figure 2.10). Addition of 5 mM  $CaCl_2$  has no impact on the apparent affinity of the interaction but does cause a significant increase ( $p < 0.01$ ) in the amount of bead-based fluorescence relative to the control, suggesting increased binding between RGS17 and  $G\alpha_o \cdot GDP \cdot AIF_4$  (Figure 2.10A, B). In contrast, the addition of 10 mM EGTA, which preferentially chelates free  $Ca^{2+}$ , has no significant effect on the amount of bead-based fluorescence, suggesting the increased signal is dependent upon the presence of  $Ca^{2+}$ . This increase in binding in the presence of  $Ca^{2+}$  is only observed between RGS17 and  $G\alpha_o \cdot GDP \cdot AIF_4$ , as  $Ca^{2+}$  had no impact on the interaction between  $G\alpha_o \cdot GDP \cdot AIF_4$  and the closely related RGS4 protein (Figure 2.10C, D).

$Mg^{2+}$  binds the same sites on RGS17 as  $Ca^{2+}$  in solution, and thus could also impact the RGS17– $G\alpha_o \cdot GDP \cdot AIF_4$  interaction. However, because  $Mg^{2+}$  is required to stabilize the transition state of  $G\alpha_o \cdot GDP \cdot AIF_4$ , its role in the protein-protein interaction cannot be directly assessed. To indirectly probe the role of  $Mg^{2+}$  in binding, 10 mM EDTA was used to chelate free  $Mg^{2+}$  in the binding reaction. Under these conditions, bead-based fluorescence decreased relative to the control. However, it is not possible to determine how much of the decrease is due to perturbation of the RGS17– $G\alpha_o \cdot GDP \cdot AIF_4$  interaction versus destabilization of activated  $G\alpha_o$ . It is possible that  $Ca^{2+}$  alters the affinity between RGS17 and  $G\alpha_o \cdot GDP$ , however, the affinity of RGS17 for inactive  $G\alpha$  subunits is too low to accurately determine.

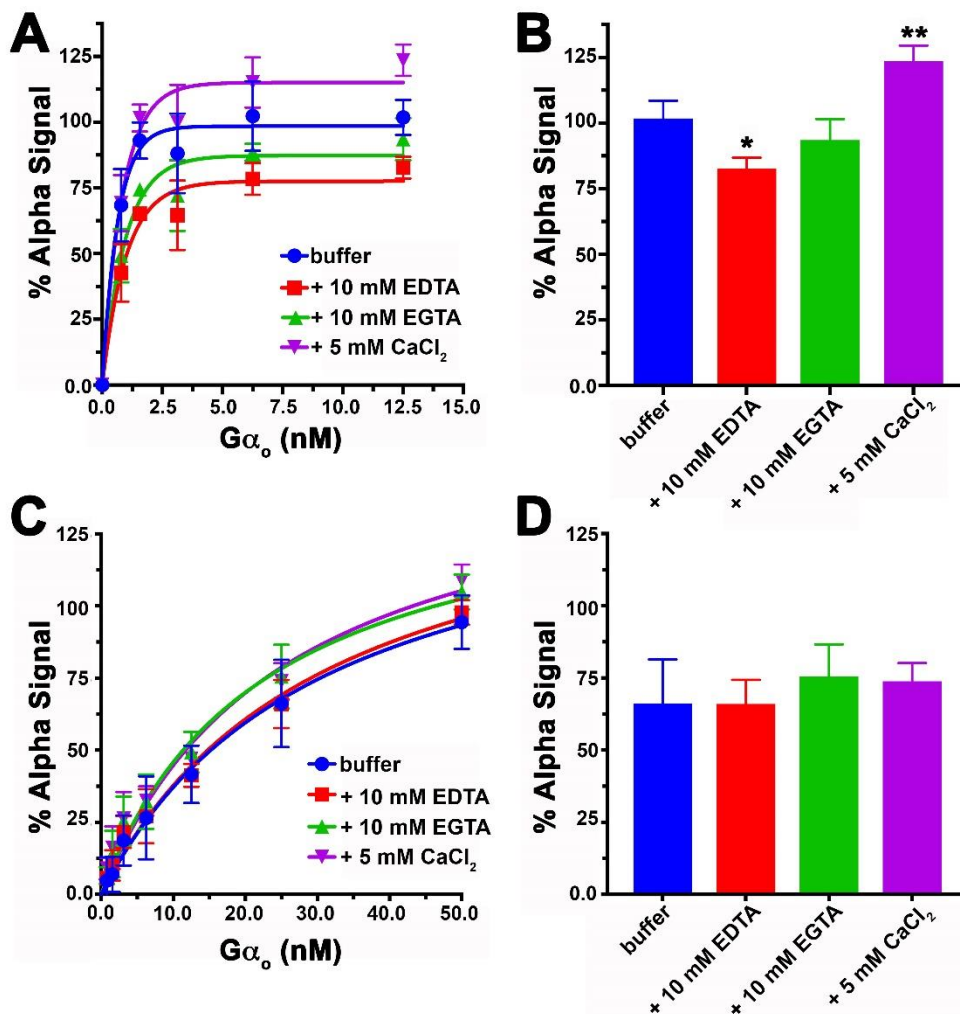


Figure 2.10.  $CaCl_2$  enhances the binding of activated  $G\alpha_o$  by RGS17, but not RGS4. An AlphaScreen assay was used to detect and quantify the binding of RGS17 to  $G\alpha_o$ . (A) RGS17 binding to activated  $G\alpha_o$  is increased upon the addition of 5 mM  $CaCl_2$  (purple inverted triangle) relative to the control (blue circle), consistent with  $Ca^{2+}$  promoting binding. Addition of 10 mM EGTA, which preferentially chelates free  $Ca^{2+}$  in solution, has no effect on the RGS17– $G\alpha_o$  interaction. In contrast, the addition of 10 mM EDTA (red squares), which preferentially chelates free  $Mg^{2+}$  in solution, decreases the binding between RGS17 and  $G\alpha_o$ . This could be due to loss of  $Mg^{2+}$  bound to RGS17 or it may reflect a decrease in the amount of activated  $G\alpha_o$ , which requires  $Mg^{2+}$  for stability. (B) Quantitation of saturation binding curves shown in panel (A). (C) RGS4 binding to activated  $G\alpha_o$  (blue circles) is not altered by  $CaCl_2$  (purple inverted triangles), EDTA (red squares), or EGTA (green triangles). (D) Quantitation of saturation binding curves shown in panel (C). Data represent the mean of three independent experiments  $\pm$  S.E.M.

### 2.3.6 $\text{Ca}^{2+}$ Increases the GTPase Activity of RGS17

$\text{Ca}^{2+}$  selectively binds to RGS17 and increases its interactions with  $\text{G}\alpha_o \cdot \text{GDP} \cdot \text{AlF}_4^-$ . Therefore,  $\text{Ca}^{2+}$  may alter the ability of RGS17 to stimulate GTP hydrolysis. A GTPase Glo assay was therefore used to measure the rate of GTP hydrolysis on a previously reported rate-altered  $\text{G}\alpha_{i1}$  mutant ( $\text{G}\alpha_{i1}$  R178M/A236S) (27) with or without  $\text{Ca}^{2+}$ . RGS17 stimulated GTPase activity on  $\text{G}\alpha_{i1}$  with statistically similar  $k_{\text{cat}}$  and  $k_{\text{cat}}/K_m$  values regardless of the presence of saturating  $[\text{Ca}^{2+}]$  (Figure 2.11A, Table 2.3). However, the  $K_m$  for RGS17-stimulated GTP hydrolysis decreased from  $1.49 \pm 0.3 \mu\text{M}$  to  $0.56 \pm 0.1 \mu\text{M}$  ( $p = 0.018$ ) in the presence of  $\text{Ca}^{2+}$ .

To determine whether the decrease in  $K_m$  upon  $\text{Ca}^{2+}$  addition was specific for RGS17, the rate of GTP hydrolysis was also measured for RGS4 and the rate-altered  $\text{G}\alpha_{i1}$  mutant ( $\text{G}\alpha_{i1}$  R178M/A236S) with or without  $\text{Ca}^{2+}$ . RGS4 increased the rate of GTP hydrolysis, but no significant change in the kinetic parameters was observed in the presence of  $\text{Ca}^{2+}$  (Figure 2.11B, Table 2.3). Thus,  $\text{Ca}^{2+}$  appears to selectively enhance the GTPase activity of RGS17. The impact of  $\text{Ca}^{2+}$  on GTP hydrolysis was also investigated using  $\text{G}\alpha_q$ . However,  $\text{G}\alpha_q$  hydrolyzed GTP too quickly for accurate measurements in this assay.

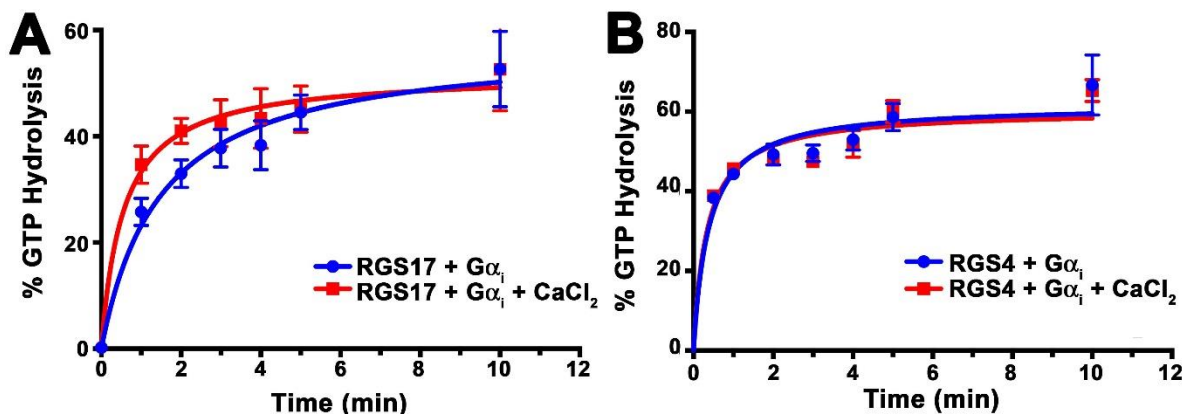


Figure 2.11.  $\text{Ca}^{2+}$  increases RGS17-stimulated GTP hydrolysis. A GTPase Glo assay was used to detect and quantify RGS-stimulated GTP hydrolysis on a rate-altered  $\text{G}\alpha_{i1}$  mutant  $\text{G}\alpha_{i1}$  R178M/A326S). (A) RGS17 increases the rate of GTP hydrolysis in the presence (red squares) or absence (blue circles) of saturating  $\text{CaCl}_2$ . Addition of  $\text{CaCl}_2$  significantly decreased the  $K_m$  (Table 2). (B) RGS4 stimulates GTP hydrolysis on  $\text{G}\alpha_{i1}$ , but is insensitive to the presence of  $\text{CaCl}_2$ . Data represent the mean of four independent experiments  $\pm$  S.E.M.

Table 2.3. Steady-state kinetic parameters for RGS17 and RGS4 GTPase activity

	$k_{cat}$ ( $\text{min}^{-1}$ )	$K_m$ ( $\mu\text{M}$ )	$V_{max}$ (% GTP hydrolysis)	$k_{cat}/K_m$ ( $\text{min}^{-1}/\mu\text{M}$ )
RGS17 + $G\alpha_i$	$57.71 \pm 2.94$	$1.49 \pm 0.26^*$	$57.1 \pm 2.94$	$38.7 \pm 6.89$
RGS17 + $G\alpha_i$ + $\text{CaCl}_2$	$51.93 \pm 2.18$	$0.56 \pm 0.14$	$51.9 \pm 2.12$	$92.9 \pm 23.2$
RGS4 + $G\alpha_i$	$61.78 \pm 2.18$	$0.39 \pm 0.08$	$61.8 \pm 2.18$	$160.4 \pm 34$
RGS4 + $G\alpha_i$ + $\text{CaCl}_2$	$60.38 \pm 2.06$	$0.34 \pm 0.07$	$60.4 \pm 2.06$	$176 \pm 38.1$

### 2.3.7 Calcium Alters the Binding Mechanism Between RGS17 and Activated $G\alpha_o$

Isothermal titration calorimetry (ITC) was utilized to further characterize the RGS17– $G\alpha_o$  binding interaction in the presence and absence of saturating concentrations of  $\text{Ca}^{2+}$  (Figure 2.12). We observed no significant difference in the dissociation constants ( $K_D$ ) of the RGS17– $G\alpha_o$  interaction in the presence ( $596 \pm 257$  nM) or absence ( $611 \pm 128.5$  nM) of  $\text{Ca}^{2+}$ . The stoichiometry of the  $G\alpha_o$ :RGS17 complex was also found to be unchanged in the presence or absence of  $\text{Ca}^{2+}$ . However, the binding enthalpy for the interaction in the presence and absence of  $\text{Ca}^{2+}$  was found to be significantly different at  $-2.76 \pm .74$  and  $-7.33 \pm .72$   $\text{K}_{cal}/\text{mol}$ , respectively. The presence of  $\text{Ca}^{2+}$  in the experiment increased the enthalpy by  $4.57$   $\text{K}_{cal}/\text{mol}$ , which is consistent with  $\text{Ca}^{2+}$  changing the binding mechanism between RGS17 and  $G\alpha_o$ . This change in binding is most likely due to a decrease in the electrostatic interactions between RGS17 and  $G\alpha_o$ , and/or by altering the local structures at the protein-protein interface (28,29).

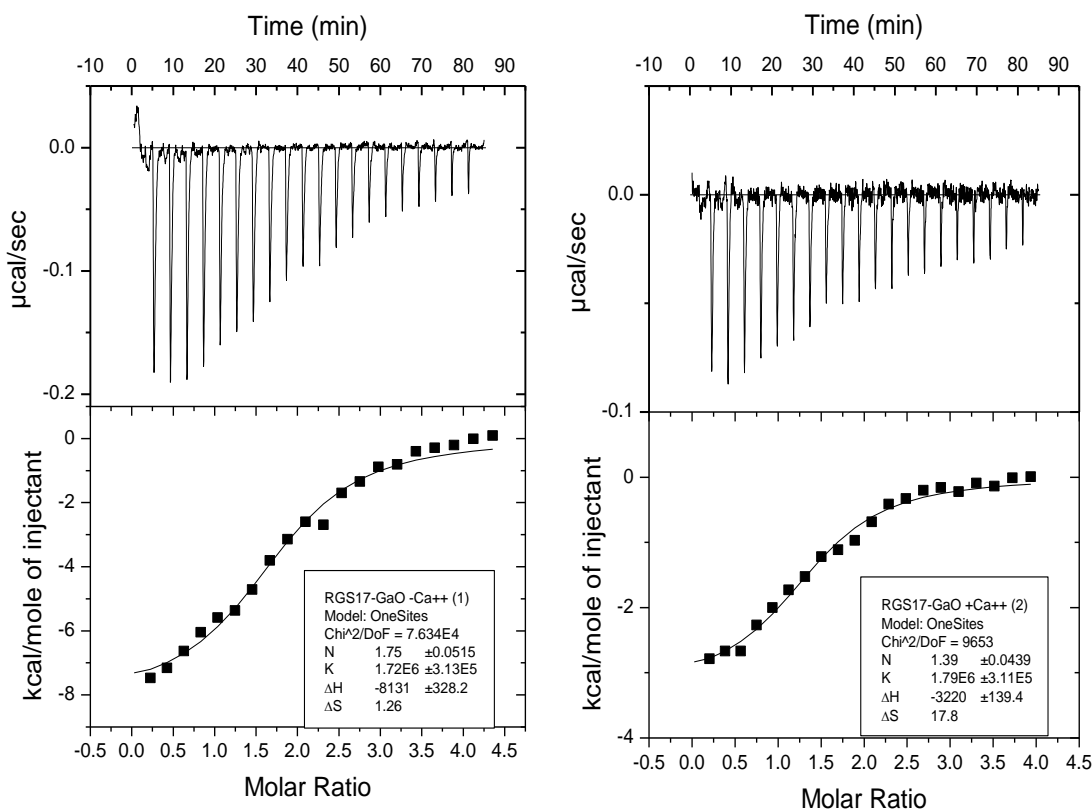


Figure 2.12. ITC characterization of RGS17-G $\alpha_o$  in the absence (Left) and presence (Right) of saturating levels of Ca<sup>2+</sup>. Dissociation constants ( $K_D$ ) were calculated to be  $611 \pm 128.5$  nM and  $596 \pm 257$  nM in the absence and presence of Ca<sup>2+</sup> respectively. The binding enthalpies were  $-7.33 \pm 0.72$  Kcal/mol and  $-2.76 \pm 0.74$  in the absence and presence of Ca<sup>2+</sup>, respectively.

## 2.4 Discussion

RGS proteins are critical negative regulators of GPCR signaling through their ability to act as GAPs for activated G $\alpha$  subunits. The RZ subfamily inhibits GPCR signaling in the nervous system, where they inactivate G $\alpha_z$ , G $\alpha_o$ , and G $\alpha_{i1-3}$ , thereby preventing G $_i$ -dependent inhibition of adenylyl cyclase (9,10). RGS17, a member of the RZ family, has also been reported to negatively regulate Ca<sup>2+</sup> signaling, suggesting it also contributes to the regulation of G $\alpha_q$ -dependent processes (15). RGS17 has emerged as a driver in cancer, in particular, lung and breast cancers (17-19), where its overexpression results in increased inhibition of G $\alpha_i$ -dependent signaling, thereby increasing cAMP and PKA activity (17). However, how RGS17 itself is regulated is not well characterized. In this study, we report a high-resolution crystal structure of RGS17 revealing that

this protein binds  $\text{Ca}^{2+}$  and provide support for a mechanism wherein  $\text{Ca}^{2+}$  binding to RGS17 enhances its interactions with activated  $\text{G}\alpha$ .

RGS17 crystallized as a dimer and both chains in the asymmetric unit preserve the canonical RH fold (Figure 2.1) (7). Despite being identical in sequence to a previously published RGS17 structure (PDB ID 1ZV4 (21)), our RGS17 structure differs from 1ZV4 in two major ways. First, the terminal subdomain is rotated with respect to the bundle subdomain by  $\sim 17^\circ$ , relative to their orientation in the 1ZV4 structure (Figure 2.2) (21,22). This suggests the terminal and bundle subdomains may be flexible in their relative orientation, which could potentially facilitate binding to activated  $\text{G}\alpha$  subunits. Secondly, our structure of RGS17 shows strong electron density for four well-resolved  $\text{Ca}^{2+}$  ions, with each chain in the asymmetric unit binding two  $\text{Ca}^{2+}$  ions (Figure 2.1). One  $\text{Ca}^{2+}$  site, formed by the backbone carbonyl of Tyr106 and the side chain of Glu109, is observed in both chains of the crystal structure (Figure 2.3A, B). We confirmed that RGS17 binds  $\text{Ca}^{2+}$  or  $\text{Mg}^{2+}$  in solution by monitoring CSPs in the NMR spectra of  $^{15}\text{N}$ -labelled RGS17 in the presence or absence of  $\text{CaCl}_2$  or  $\text{MgCl}_2$  (Figure 2.4, 5). Each RGS17 chain in the crystal structure also bound a second  $\text{Ca}^{2+}$  through the backbone carbonyl of Gln124 or via the backbone carbonyl of Ile143 and the side chain of Glu148. We demonstrated that this latter site also displayed CSP upon addition of  $\text{MgCl}_2$  and  $\text{CaCl}_2$ , and therefore likely represents a secondary cation binding site (Figure 2.5). Subsequent NMR experiments examined the affinities of these two metal binding sites for  $\text{Mg}^{2+}$  and  $\text{Ca}^{2+}$ . RGS17 was found to preferentially bind  $\text{Ca}^{2+}$  in solution, as the site formed by Tyr106 and Glu109 exhibited a  $K_{D,\text{avg}}$  of  $132 \pm 35 \mu\text{M}$ , a 257-fold increase in the affinity relative to  $\text{Mg}^{2+}$ . The metal-binding site formed by the carbonyl of Ile143 and the Glu148 sidechain showed a similar trend in the affinity, where the  $K_{D,\text{avg}}$  was found to be  $91 \pm 6 \mu\text{M}$  for  $\text{Ca}^{2+}$ , 219-fold higher affinity than that observed for  $\text{Mg}^{2+}$  (Figure 2.7).

RGS17, and potentially the RZ subfamily, bind  $\text{Ca}^{2+}$  and  $\text{Mg}^{2+}$  to a greater extent than other RGS proteins. For example, RGS4 is able to bind  $\text{Ca}^{2+}$  in solution through sites equivalent to those observed in RGS17 (Figure 2.8), but with  $\sim 70$ -fold lower affinity. RGS4 bound even more weakly to  $\text{Mg}^{2+}$ , with 10-fold lower affinity than  $\text{Ca}^{2+}$ . However, the calculated  $K_{D,\text{avg}}$  for the two cation binding sites were within the error range of the experiment ( $93 \pm 193 \text{ mM}$  for the site including residues Tyr84 and Glu86, and  $90 \pm 75 \text{ mM}$  for the site formed by Val121 and Glu126, Figure 2.8). Thus, RGS4 does not appreciably bind  $\text{Mg}^{2+}$  under these conditions. Similar results were obtained with RGS2, which had only minimal changes in its  $^1\text{H}$ - $^{15}\text{N}$  spectra at  $\text{Ca}^{2+}$  concentrations

up to 250-fold and in the spectra observed at 500-fold excess  $Mg^{2+}$  (Figure 2.9). Thus, despite the sequence conservation of the RH domain and the residues involved in cation binding, RGS4 and RGS2 interact weakly with  $Ca^{2+}$  in solution.

$Ca^{2+}$  and  $Mg^{2+}$  bind the same face of RGS17 that is predicted to interact with the switch regions of activated  $G\alpha$  subunits to promote GTP hydrolysis (Figure 2.13). Comparison of the RGS17- $Ca^{2+}$  structure with RGS- $G\alpha$  complexes (6,30-33) would suggest that  $Ca^{2+}$  could inhibit  $G\alpha$  binding. To test this hypothesis, an AlphaScreen protein interaction assay was used to measure binding between RGS17 and  $G\alpha_o$ . Addition of  $Ca^{2+}$  increased the observed binding between RGS17 and  $G\alpha_o$ , whereas addition of EGTA had no effect on the interaction (Figure 2.10). The increased interactions between RGS17 and  $G\alpha$  may also contribute to changes in GTP hydrolysis. We found that  $Ca^{2+}$  decreased the  $K_m$  for RGS17-stimulated GTP hydrolysis on  $G\alpha_{i1}$ , but had no impact on RGS4-stimulated GTP hydrolysis (Figure 2.11, Table 2.3). Finally, isothermal calorimetry revealed a significant difference in binding enthalpy for the RGS17- $G\alpha_o$  interaction brought about by the presence of  $Ca^{2+}$  (Figure 2.12).  $Ca^{2+}$  was found to increase the binding enthalpy by 4.57  $K_{cal}/mol$ , demonstrating that  $Ca^{2+}$  changes the binding mechanism for RGS17- $G\alpha_o$ . Polar interactions and/or conformational changes are typically reflected in the enthalpy of binding (28,29). Thus,  $Ca^{2+}$  may alter binding by decreasing the polar contacts between RGS17 and  $G\alpha_o$ , and/or altering the local structure at the protein interfaces.

Taken together, our data suggest  $Ca^{2+}$  regulates RGS17 activity. While  $Ca^{2+}$  binding directly to other RGS proteins has not been previously reported, there is a precedent for  $Ca^{2+}$ -mediated regulation of RGS activity. For example,  $Ca^{2+}$ /calmodulin is a known regulator of some RZ and R4 subfamily members. These RGS proteins are inhibited when bound to  $PIP_3$  at the cell membrane and this inhibition is relieved upon binding  $Ca^{2+}$ /calmodulin (9,34-36). Thus, these RGS proteins are activated following  $G_q$ -dependent  $Ca^{2+}$  release, providing a feedback mechanism to inhibit further  $G_q$  signaling (34,35). Thus, additional studies will be required to determine whether  $Ca^{2+}$ , alone or in combination with calmodulin, may be a general regulator of RZ RGS function.

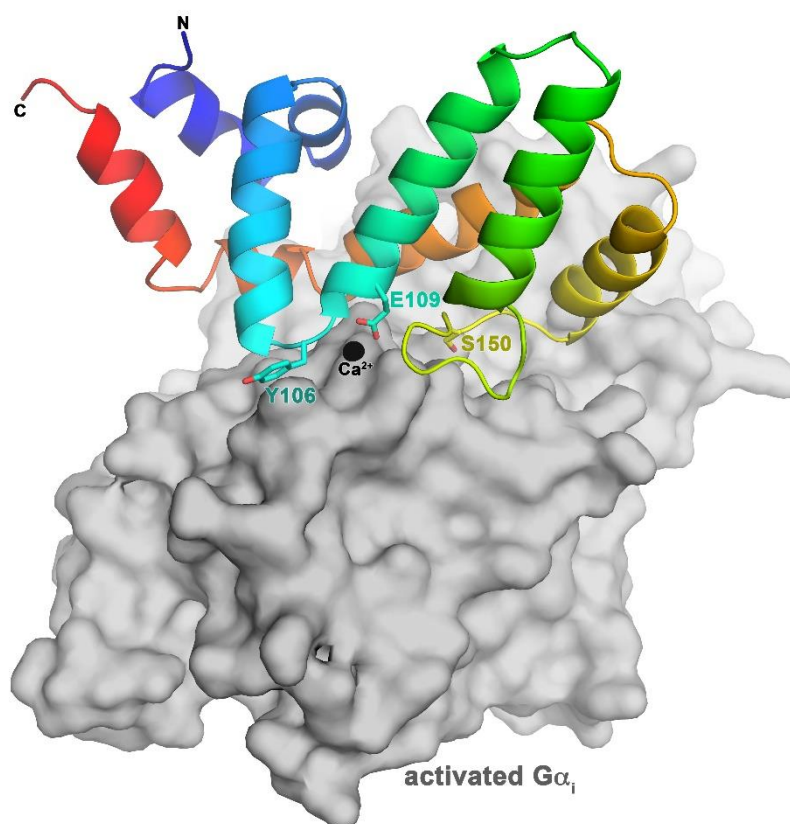


Figure 2.13. Model of RGS17 bound to activated  $G\alpha_i$ . RGS17 is proposed to bind to the switch regions of  $G\alpha$  subunits to promote GTP hydrolysis, based on the superposition of RGS17 with RGS4 in its complex with activated  $G\alpha_i$  (PDB ID 1AG4) (6). Ser150 is required for GAP activity and is equivalent to Asn128 in RGS4 (9). Tyr106 and Glu109 coordinate a  $Ca^{2+}$  ion (shown as a black sphere) in the structure of RGS17 and are located on the predicted  $G\alpha_i$  binding surface. RGS17 is shown color-ramped from blue at the N-terminus to red at the C-terminus and activated  $G\alpha_i$  is shown as a gray surface.

## 2.5 Experimental Procedures

### 2.5.1 RGS17 Expression and Purification

A construct for the RGS17 protein, encoding residues 70-206, was obtained from Addgene (#39141) and was a gift from Nicola Burgess-Brown (The Structural Genomics Consortium). RGS17 was purified largely as previously described (21). Briefly, RGS17 was expressed in BL21-CodonPlus(DE3)-RIPL cells and grown at 37 °C and 275-300 rpm until an  $OD_{600}$  of 2.0 was reached. Protein production was then induced with 0.5-1 mM IPTG, and the culture was incubated for an additional 16 h at 18 °C while shaking at 275-300 rpm. Bacterial cells were then pelleted

and resuspended in 50 mM HEPES, 500 mM NaCl, 1 mM  $\beta$ -mercaptoethanol, 10 mM imidazole at pH 8 (Buffer A) at 4 °C. Cells were lysed with lysozyme (1 mg mL<sup>-1</sup> cell pellet), and DNase I (approximately 2 mg) was added. The lysate was then subjected to multiple freeze-thaw cycles in liquid N<sub>2</sub>, and the soluble lysate fraction was separated by centrifugation at 100,000 x g. His-tagged RGS17 was then separated from the supernatant using an AKTA FPLC (GE Healthcare, Chicago, IL) equipped with an immobilized metal affinity chromatography column (IMAC) (Ni Sepharose 6 Fast Flow, GE Healthcare, Chicago, IL). Eluted fractions containing RGS protein were then treated with His-tagged TEV protease at approximately 1:20 TEV:RGS molar ratio and dialyzed overnight at 4°C against 5 L Buffer A to cleave the His<sub>6</sub> tag. Samples were again subjected to IMAC and the flow through was collected. Size-exclusion chromatography (10 mM borate, 500 mM NaCl, and 1 mM DTT at pH 7.0) was then used to obtain 99+% pure RGS17, as determined by SDS-PAGE.

Isotope-labeled (<sup>15</sup>N and <sup>13</sup>C-<sup>15</sup>N) RGS17 was purified largely as above, with the exception that when culture OD<sub>600</sub> reached 1.5, cells were pelleted at 3,500 x g at 4 °C for 15 min, and resuspended in an equal volume of M9 minimal media supplemented with 2 g L<sup>-1</sup> D-Glucose-<sup>13</sup>C<sub>6</sub> and 1 g L<sup>-1</sup> <sup>15</sup>NH<sub>4</sub>Cl for <sup>13</sup>C-<sup>15</sup>N sample or 1 g L<sup>-1</sup> <sup>15</sup>NH<sub>4</sub>Cl for <sup>15</sup>N sample. Isotope-labeled samples were concentrated to >1 mM in 20 mM K<sub>2</sub>HPO<sub>4</sub> buffer with 100 mM NaCl, 0.5 mM  $\beta$ -mercaptoethanol, and 2 mM NaN<sub>3</sub>, at pH 7.6. Prior to all NMR experiments, RGS17 was exhaustively dialyzed against 55 mM HEPES, 110mM NaCl, 0.55 mM  $\beta$ -mercaptoethanol at pH 7.6 to remove phosphate buffer.

### 2.5.2 Crystallization of RGS17

Initial crystallization conditions were determined using commercially available crystallization screens. Hanging drop vapor-diffusion experiments were set up in 96-well polystyrene microplates (Greiner Bio-one) using a Mosquito LCP crystallization robot (TTP Labtech) at 25 °C. The drops contained an equal volume (200 nL) of RGS17 (20.6 mg/mL in 10 mM borate pH 7.0, 500 mM NaCl, 1 mM DTT) and reservoir solution (0.2 M CaCl<sub>2</sub> and 20% PEG 3350, pH 5.1) of the PEG/Ion Screen (Hampton Research) suspended over 50  $\mu$ L of reservoir. Conditions were optimized in-house using 24-well SuperClear Pregreased plates (Crystalgen) with drops containing equal volumes (0.5  $\mu$ L) of RGS17 (16 mg/mL) and precipitant solution. Final crystals were obtained from reservoirs containing 0.2 M CaCl<sub>2</sub>, 22% PEG 3350 (w/v), and 0.1 M

MES pH 6.0 at 12 °C using streak seeding. Crystals were harvested in 0.2 M calcium chloride dihydrate, 40% PEG 3350, 0.1 M MES pH 6.0 and frozen on nylon loops in liquid N<sub>2</sub>.

### 2.5.3 Data Collection, Processing, and Refinement

Diffraction data were collected at 100 K using an Eiger detector at the Advanced Photon Source at LS-CAT 21-ID-D. HKL2000 was used to integrate and scale the data, and Phaser in CCP4 (37) was used to solve the structure by molecular replacement with the prior structure of RGS17 (PDB ID 1ZV4 (21)) as a starting model. The structure was built by manual model building in COOT (38) alternating with TLS refinement in REFMAC5 (39). The correctness of the structure was assessed using MolProbity (40). Structure figures were generated using PyMOL 1.8.6.2 (Schrödinger, LLC).

### 2.5.4 Nuclear Magnetic Resonance

The following triple resonance experiments were performed at 25 °C using a 600 MHz Varian INOVA NMR spectrometer equipped with a triple resonance gradient probe to assign RGS17-RH backbone (and C $\beta$ ) chemical shifts: HNCACB, CBCA(CO)NH, HNCO, and HN(CA)CO). Data were processed and analyzed using NMRPipe (41) and CCPNAnalysis (42), respectively. 260  $\mu$ M RGS17 in 50 mM HEPES, 100 mM NaCl, 0.5 mM  $\beta$ -mercaptoethanol, pH 7.6 in 10% D<sub>2</sub>O was incubated with or without the indicated concentration of CaCl<sub>2</sub> or MgCl<sub>2</sub>. Subsequently, <sup>1</sup>H-<sup>15</sup>N HSQC spectra were acquired at 25 °C using either a 500 MHz Bruker Avance II or a 600 MHz Varian INOVA NMR spectrometer each equipped with a triple resonance gradient probe.

NMR experiments with RGS4 and RGS2 were carried out as described for RGS17. <sup>1</sup>H-<sup>15</sup>N HSQC spectra of 375  $\mu$ M RGS4 in 50 mM HEPES, 100 mM NaCl, 10 mM  $\beta$ -mercaptoethanol at pH 7.6 and 10% D<sub>2</sub>O or 300  $\mu$ M RGS2 50 mM HEPES, 100 mM NaCl, 11 mM  $\beta$ -mercaptoethanol at pH 7.6 in 10% D<sub>2</sub>O were acquired, followed by addition of increasing concentrations of CaCl<sub>2</sub> or MgCl<sub>2</sub>. Chemical shift assignments for RGS4 were confirmed using prior assignments (25), while the spectrum of RGS2 has not been assigned.

Chemical shift perturbations (CSPs) between control and metal-treated samples were calculated by measuring the distance between the centers of the peaks using the following equation:

$$CSP = \sqrt{(\Delta\delta_H)^2 + (0.101 \times \Delta\delta_N)^2}$$

where  $\Delta\delta_H$  and  $\Delta\delta_N$  are the difference in a chemical shift in the absence and presence of cation in the indicated dimension.

$K_D$  values for individual residues with  $CSP \geq 2$  S.D. from the mean were obtained using GraphPad Prism 7 by fitting CSP titration data to a one site binding model with correction for ligand depletion as follows:

$$CSP = CSP_{max} \left( \frac{([M^{2+}] + 2[P] + K_D) - \sqrt{([M^{2+}] + 2[P] + K_D)^2 - 4 \times 2[P][M^{2+}]}}{2 \times 2[P]} \right)$$

where  $CSP_{max}$  is the maximum CSP value observed,  $[M^{2+}]$  is concentration metal ion,  $[P]$  is the concentration protein, and  $K_D$  is the dissociation constant. Note:  $2 \times [P]$  was used to account for the two metal binding sites on each molecule of RGS17.  $K_D$  values obtained for residues were averaged to determine the  $K_{D, avg}$  of metal-binding sites. Identical residues were used for  $Mg^{2+}$   $K_D$  determinations.

### 2.5.5 Differential Scanning Fluorimetry

The impact of  $Ca^{2+}$  or  $Mg^{2+}$  on the thermal stability of RGS17 was determined by measuring the change in fluorescence of SYPRO Orange (Molecular Probes, Eugene, OR) due to protein denaturation as a function of temperature (43). RGS17 was exchanged into a buffer containing 10 mM borate pH 9.0, 500 mM NaCl, and 1 mM DTT. RGS17 at a final concentration of 0.9 mg/mL was incubated with 5X SYPRO Orange dye and increasing concentrations of  $CaCl_2$  or  $MgCl_2$  (0.2 nM – 200 mM) for 30 min on ice in a final volume of 20  $\mu$ L. Samples were assayed in triplicate in a MicroAmp Optical 96-well plate and sealed with MicroAmp Optical Adhesive Film (Applied Biosystems), and centrifuged for 1 min. DSF assays were carried out on a ViiA7 qPCR instrument (Thermo Fisher). The change in fluorescence was measured at 0.2  $^{\circ}C$  intervals from 25-95  $^{\circ}C$ . The  $T_m$  was calculated by fitting the increase in fluorescence as a function of temperature to a Boltzmann sigmoid (GraphPad Prism 7.0). Data represent the mean of at least three experiments performed in triplicate  $\pm$  S.E.M.

### 2.5.6 AlphaScreen Method for the RGS17–G $\alpha_o$ Interaction

RGS17–G $\alpha_o$  binding was assessed as previously described (44). Biotinylated RGS17 was conjugated to streptavidin donor bead in ALPHA Buffer (20 mM HEPES, 100 mM NaCl, 1% BSA, 1% Lubrol, pH 8). GST-rG $\alpha_o$ , purified as previously described (45) was conjugated to anti-GST acceptor beads in ALPHA buffer. G $\alpha_o$  mixture was supplemented with a 5  $\mu$ M AlCl<sub>3</sub>, 5 mM MgCl<sub>2</sub>, and 5 mM NaF (AMF), and 2.5 mM GDP. Final concentrations were 100 nM RGS17, indicated concentration of G $\alpha_o$ , and 15 ng/ $\mu$ l of each bead. The assay was incubated for 1 h at ambient temperature and then fluorescence measured using a Perkin Elmer Envision plate reader. Wells lacking AMF represented negative control and were normalized to 0%, and wells containing RGS17 in ALPHA buffer alone were normalized to 100%. Data analysis was performed using GraphPad Prism 7.

### 2.5.7 GTP Hydrolysis Assays

RGS-stimulated GTP hydrolysis was measured using a rate-altered G $\alpha_i$  variant, G $\alpha_{i1}$  R178M/A326S, which was expressed and purified as previously described (27,46). GTPase activity was measured using the Promega GTPase-Glo<sup>TM</sup> assay (Promega, Madison, WI) as has been described, but with some modifications (47). Briefly, 1  $\mu$ M G $\alpha_{i1}$  R178M/A326S and 1  $\mu$ M RGS17 or RGS4 were incubated in GTPase/GAP reaction buffer (50 mM Tris-HCl, pH 7.5, 50 mM NaCl, and 10 MgCl<sub>2</sub>) in the presence or absence of 100  $\mu$ M CaCl<sub>2</sub> for 30 minutes. The reaction was initiated by the addition of 2.5  $\mu$ M GTP (10  $\mu$ L final volume) and allowed to proceed for increasing time points before the addition of an equal volume of GTPase-Glo reagent and a 30-minute incubation. The GTPase-Glo reagent uses a nucleoside diphosphate kinase and ADP to convert remaining GTP to ATP and GDP. The GTPase activity inversely correlates with ATP production and is detected with the detection reagent containing a luciferase/luciferin mix. 20  $\mu$ L of this detection reagent was added to 20  $\mu$ L of the reaction mixture and incubated in the dark for 10 minutes. Assay plates (Corning 3572, 384-well) were read on a Synergy 2 plate reader (Biotek; Winooski, VT) in luminescence mode. Time points at 0.5, 1, 2, 3, 4, 5, and 10 minutes post-GTP addition were taken. Wells without GTP was used in the normalization of values for data analysis to represent 100% GTP hydrolysis while wells without G $\alpha_{i1}$  R178M/A326S represented 0% GTP hydrolysis. Data analysis was performed using GraphPad Prism 7.

### 2.5.8 Isothermal Titration Calorimetry.

$G\alpha_o$  was concentrated in ITC sample buffer (50 mM HEPES pH 8.0, 200 mM NaCl, 2 mM  $\beta$ -mercaptoethanol, and 50  $\mu$ M GTP $\gamma$ S) to 3  $\mu$ M. RGS17 was concentrated in ITC sample buffer to 60  $\mu$ M and 53.4  $\mu$ M for - and +  $Ca^{2+}$  samples, respectively. 45 mM  $Ca^{2+}$  was included in  $G\alpha_o$  and RGS17 samples to achieve saturation as determined by  $^1H$ - $^{15}N$  2D HSQC NMR. RGS17 injections of 14  $\mu$ L over 20 total injections were added to the ITC cell containing 1.4 mL of  $G\alpha_o$  to reach a molar ratio (RGS17/ $G\alpha_o$ ) of 4.5. An injection duration time of 14 seconds and a spacing of 240 seconds were set for each injection. All experiments were conducted on a GE MicroCal VP-ITC System (General Electric; Piscataway, NJ, USA) at 25 °C. Heats of dilution were determined by averaging the heat evolved by the last five injections and subtracted from the raw data. The values for affinity, stoichiometry, and change in enthalpy were then determined using the ORIGIN software provided by the manufacturer. Replicates for each run were further analyzed using GraphPad Prism 7.

## 2.6 Acknowledgments

This work is supported by an American Heart Association Scientist Development Grant 16SDG29920017 (A.M.L.), NIH 1R01HL141076-01 (A.M.L.), and an American Cancer Society Institutional Research Grant (IRG-14-190-56) to the Purdue University Center for Cancer Research (A.M.L.). Use of the Advanced Photon Source, an Office of Science User Facility operated for the U. S. Department of Energy (DOE) Office of Science by Argonne National Laboratory, was supported by the U.S. DOE under Contract Number DE-AC02-06CH11357. We thank the LS-CAT staff members for their help with data collection. Coordinates and structure factors for RGS17 are deposited in the Protein Data Bank as 6AM3. The content is solely the responsibility of the authors and does not necessarily represent the official views of the National Institutes of Health.

## 2.7 Conflict of Interest

The authors declare that they have no conflicts of interest with the contents of this article.

## 2.8 Author Contributions

D.L.R. and A.M.L. designed the experimental approach. M.P.H. expressed and purified RGS17 and  $G\alpha_o$  proteins. M.P.H., J.B.O., and C.A.F. carried out all NMR experiments. J.B.O. and M.P.H. performed the AlphaScreen experiments, J.B.O. performed the GTPase experiments, and J.B.O. and J.C.H. performed the ITC experiments. M.S. crystallized RGS17, and M.S. and A.M.L. solved the crystal structure. M.S. carried out the DSF assays. M.S., M.P.H., J.B.O., C.A.F., D.L.R., and A.M.L. wrote the manuscript.

## 2.9 References

1. Oldham, W.M., and Hamm, H.E. (2008). Heterotrimeric G protein activation by G-protein-coupled receptors. *Nat Rev Mol Cell Biol.*, **9**, 60-71.
2. Dohlman, H.G., Apaniesk, D., Chen, Y., Song, J., and Nusskern, D. (1995). Inhibition of G-protein signaling by dominant gain-of-function mutations in Sst2p, a pheromone desensitization factor in *Saccharomyces cerevisiae*. *Mol Cell Biol.*, **15**, 3635-3643.
3. De Vries, L., Zheng, B., Fischer, T., Elenko, E., and Farquhar, M. G. (2000). The Regulator of G Protein Signaling Family. *Annu Rev Pharmacol Toxicol.*, **40**, 235-271.
4. Koelle, M.R., and Horvitz, H.R. (1996). EGL-10 regulates G protein signaling in the *C. elegans* nervous system and shares a conserved domain with many mammalian proteins. *Cell*, **84**, 115-125.
5. Berman, D.M., Wilkie, T.M., and Gilman, A.G. (1996). GAIP and RGS4 are GTPase-activating proteins for the  $G_i$  subfamily of G protein alpha subunits. *Cell*, **86**, 445-452.
6. Tesmer, J.J., Berman, D.M., Gilman, A.G., and Sprang, S.R. (1997). Structure of RGS4 bound to  $AlF_4^-$ -activated  $G_{i\alpha_1}$ : stabilization of the transition state for GTP hydrolysis. *Cell*, **89**, 251-261.
7. Tesmer, J.J. (2009). Structure and function of regulator of G protein signaling homology domains. *Prog Mol Biol Transl Sci.*, **86**, 75-113.
8. Popov, S., Yu, K., Kozasa, T., and Wilkie, T.M. (1997). The regulators of G protein signaling (RGS) domains of RGS4, RGS10, and GAIP retain GTPase activating protein activity in vitro. *Proc Natl Acad Sci U S A*, **94**, 7216-7220.
9. Ross, E.M., and Wilkie, T.M. (2000). GTPase-activating proteins for heterotrimeric G proteins: regulators of G protein signaling (RGS) and RGS-like proteins. *Annu Rev Biochem.*, **69**, 795-827.

10. Nunn, C., Mao, H., Chidiac, P., and Albert, P.R. (2006). RGS17/RGSZ2 and the RZ/A family of regulators of G-protein signaling. *Semin Cell Dev Bio.*, **17**, 390-399.
11. De Vries, L., Elenko, E., Hubler, L., Jones, T.L., and Farquhar, M.G. (1996). GAIP is membrane-anchored by palmitoylation and interacts with the activated (GTP-bound) form of G alpha i subunits. *Proc Natl Acad Sci U S A*, **93**, 15203-15208.
12. Hayes, M.P., and Roman, D.L. (2016). Regulator of G Protein Signaling 17 as a Negative Modulator of GPCR Signaling in Multiple Human Cancers. *AAPS J.*, **18**, 550-559.
13. Natochin, M., McEntaffer, R.L., and Artemyev, N.O. (1998). Mutational analysis of the Asn residue essential for RGS protein binding to G-proteins. *J Biol Chem.*, **273**, 6731-6735.
14. Posner, B.A., Mukhopadhyay, S., Tesmer, J.J., Gilman, A.G., and Ross, E.M. (1999). Modulation of the Affinity and Selectivity of RGS Protein Interaction with G $\alpha$ Subunits by a Conserved Asparagine/Serine Residue. *Biochemistry*, **38**, 7773-7779.
15. Mao, H., Zhao, Q., Daigle, M., Ghahremani, M.H., Chidiac, P., and Albert, P.R. (2004). RGS17/RGSZ2, a Novel Regulator of Gi/o, Gz, and Gq Signaling. *J Biol Chem.*, **279**, 26314-26322.
16. Larminie, C., Murdock, P., Walhin, J.P., Duckworth, M., Blumer, K.J., Scheideler, M.A., and Garnier, M. (2004). Selective expression of regulators of G-protein signaling (RGS) in the human central nervous system. *Mol Brain Res.*, **122**, 24-34.
17. James, M.A., Lu, Y., Liu, Y., Vikis, H.G., and You, M. (2009). RGS17, an Overexpressed Gene in Human Lung and Prostate Cancer, Induces Tumor Cell Proliferation Through the Cyclic AMP-PKA-CREB Pathway. *Cancer Res.*, **69**, 2108-2116.
18. You, M., Wang, D., Liu, P., Vikis, H., James, M., Lu, Y., Wang, Y., Wang, M., Chen, Q., Jia, D., Liu, Y., Wen, W., Yang, P., Sun, Z., Pinney, S.M., Zheng, W., Shu, X.O., Long, J., Gao, Y.T., Xiang, Y.B., Chow, W.H., Rothman, N., Petersen, G.M., de Andrade, M., Wu, Y., Cunningham, J.M., Wiest, J.S., Fain, P.R., Schwartz, A.G., Girard, L., Gazdar, A., Gaba, C., Rothschild, H., Mandal, D., Coons, T., Lee, J., Kupert, E., Seminara, D., Minna, J., Bailey-Wilson, J.E., Amos, C.I., and Anderson, M.W. (2009). Fine Mapping of Chromosome 6q23-25 Region in Familial Lung Cancer Families Reveals RGS17 as a Likely Candidate Gene. *Clin Cancer Res.*, **15**, 2666-2674.
19. Li, Y., Li, L., Lin, J., Hu, X., Li, B., Xue, A., Shen, Y., Jiang, J., Zhang, M., Xie, J., and Zhao, Z. (2015). Deregulation of RGS17 Expression Promotes Breast Cancer Progression. *J Cancer*, **6**, 767-775.
20. Sokolov, E., Iannitti, D.A., Schrum, L.W., and McKillop, I.H. (2011). Altered expression and function of regulator of G-protein signaling-17 (RGS17) in hepatocellular carcinoma. *Cell Signal.*, **23**, 1603-1610.

21. Soundararajan, M., Willard, F.S., Kimple, A.J., Turnbull, A.P., Ball, L.J., Schoch, G.A., Gileadi, C., Fedorov, O.Y., Dowler, E.F., Higman, V.A., Hutsell, S.Q., Sundstrom, M., Doyle, D.A., and Siderovski, D.P. (2008). Structural diversity in the RGS domain and its interaction with heterotrimeric G protein alpha-subunits. *Proc Natl Acad Sci U S A*, **105**, 6457-6462.
22. Krissinel, E., and Henrick, K. (2004). Secondary-structure matching (SSM), a new tool for fast protein structure alignment in three dimensions. *Acta Crystallogr D Biol Crystallogr.*, **60**, 2256-2268.
23. Faurobert, E., and Hurley, J.B. (1997). The core domain of a new retina specific RGS protein stimulates the GTPase activity of transducin in vitro. *Proc Natl Acad Sci U S A*, **94**, 2945-2950.
24. Wang, J., Ducret, A., Tu, Y., Kozasa, T., Aebersold, R., and Ross, E.M. (1998). RGSZ1, a Gz-selective RGS protein in brain. Structure, membrane association, regulation by Galphaz phosphorylation, and relationship to a Gz GTPase-activating protein subfamily. *J Biol Chem.*, **273**, 26014-26025.
25. Moy, F.J., Chanda, P.K., Cockett, M.I., Edris, W., Jones, P.G., Mason, K., Semus, S., and Powers, R. (2000). NMR structure of free RGS4 reveals an induced conformational change upon binding Galpha. *Biochemistry*, **39**, 7063-7073.
26. Mackie, D.I., and Roman, D.L. (2011). Development of a novel high-throughput screen and identification of small-molecule inhibitors of the Galpha-RGS17 protein-protein interaction using AlphaScreen. *J Biomol Screen.*, **16**, 869-877.
27. Monroy, C.A., Mackie, D.I., and Roman, D.L. (2013). A High Throughput Screen for RGS Proteins Using Steady State Monitoring of Free Phosphate Formation. *PLoS ONE*, **8**, e62247.
28. Ladbury, J.E. (2010). Calorimetry as a tool for understanding biomolecular interactions and an aid to drug design. *Biochem Soc Trans.*, **38**, 888-893.
29. Ward, W.H., and Holdgate, G. A. (2001). Isothermal titration calorimetry in drug discovery. *Prog Med Chem.*, **38**, 309-376.
30. Taylor, V.G., Bommarito, P.A., and Tesmer, J.J. (2016). Structure of the Regulator of G Protein Signaling 8 (RGS8)-Galphaq Complex: MOLECULAR BASIS FOR Galpha SELECTIVITY. *J Biol Chem.*, **291**, 5138-5145.
31. Nance, M.R., Kreutz, B., Tesmer, V.M., Sterne-Marr, R., Kozasa, T., and Tesmer, J.J. (2013). Structural and functional analysis of the regulator of g protein signaling 2-galpaq complex. *Structure*, **21**, 438-448.

32. Kimple, A.J., Soundararajan, M., Hutsell, S.Q., Roos, A.K., Urban, D.J., Setola, V., Temple, B.R., Roth, B.L., Knapp, S., Willard, F.S., and Siderovski, D.P. (2009). Structural determinants of G-protein  $\alpha$  subunit selectivity by regulator of G-protein signaling 2 (RGS2). *J Biol Chem.*, **284**, 19402-19411.
33. Slep, K.C., Kercher, M.A., He, W., Cowan, C.W., Wensel, T.G., and Sigler, P.B. (2001). Structural determinants for regulation of phosphodiesterase by a G protein at 2.0 Å. *Nature*, **409**, 1071-1077.
34. Popov, S.G., Krishna, U.M., Falck, J.R., and Wilkie, T.M. (2000).  $\text{Ca}^{2+}$ /Calmodulin reverses phosphatidylinositol 3,4, 5-trisphosphate-dependent inhibition of regulators of G protein-signaling GTPase-activating protein activity. *J Biol Chem.*, **275**, 18962-18968.
35. Ishii, M., Fujita, S., Yamada, M., Hosaka, Y., and Kurachi, Y. (2005). Phosphatidylinositol 3,4,5-trisphosphate and  $\text{Ca}^{2+}$ /calmodulin competitively bind to the regulators of G-protein-signalling (RGS) domain of RGS4 and reciprocally regulate its action. *Biochem J.*, **385**, 65-73.
36. Ishii, M., and Kurachi, Y. (2004). Assays of RGS Protein Modulation by Phosphatidylinositides and Calmodulin. **389**, 105-118.
37. Storoni, L.C., McCoy, A.J., and Read, R.J. (2004). Likelihood-enhanced fast rotation functions. *Acta Crystallogr D Biol Crystallogr.*, **60**, 432-438.
38. Emsley, P., Lohkamp, B., Scott, W.G., and Cowtan, K. (2009). Features and development of *Coot*. *Acta Crystallogr D Biol.*, **D66**, 486-501.
39. Murshudov, G.N., Skubak, P., Lebedev, A.A., Pannu, N.S., Steiner, R.A., Nicholls, R.A., Winn, M.D., Long, F., and Vagin, A.A. (2011). REFMAC5 for the refinement of macromolecular crystal structures. *Acta Crystallogr D Biol Crystallogr.*, **67**, 355-367.
40. Davis, I.W., Leaver-Fay, A., Chen, V.B., Block, J.N., Kapral, G.J., Wang, X., Murray, L.W., Arendall, W.B., 3rd, Snoeyink, J., Richardson, J.S., and Richardson, D.C. (2007). MolProbity: all-atom contacts and structure validation for proteins and nucleic acids. *Nucleic Acids Res.*, **35**, W375-383.
41. Delaglio, F., Grzesiek, S., Vuister, G.W., Zhu, G., Pfeifer, J., and Bax, A. (1995). NMRPipe: a multidimensional spectral processing system based on UNIX pipes. *J Biomol NMR*, **6**, 277-293.
42. Vranken, W.F., Boucher, W., Stevens, T.J., Fogh, R.H., Pajon, A., Llinas, M., Ulrich, E.L., Markley, J.L., Ionides, J., and Laue, E.D. (2005). The CCPN data model for NMR spectroscopy: development of a software pipeline. *Proteins*, **59**, 687-696.
43. Mezzasalma, T.M., Kranz, J.K., Chan, W., Struble, G.T., Schalk-Hihi, C., Deckman, I.C., Springer, B.A., and Todd, M.J. (2007). Enhancing recombinant protein quality and yield by protein stability profiling. *J Biomol Screen.*, **12**, 418-428.

44. Bodle, C.R., Mackie, D.I., Hayes, M.P., Schamp, J.H., Miller, M.R., Henry, M.D., Doorn, J.A., Houtman, J.C.D., James, M.A., and Roman, D.L. (2017). Natural Products Discovered in a High-Throughput Screen Identified as Inhibitors of RGS17 and as Cytostatic and Cytotoxic Agents for Lung and Prostate Cancer Cell Lines. *J Nat Prod.*, **80**, 1992-2000.
45. Delprato, A.M., Monroy, C.A., Mackie, D.I., and Roman, D.L. (2013). A High Throughput Screen for RGS Proteins Using Steady State Monitoring of Free Phosphate Formation. *PLoS ONE*, **8**, e62247.
46. Zielinski, T., Kimple, A.J., Hutsell, S.Q., Koeff, M.D., Siderovski, D.P., and Lowery, R.G. (2009). Two Galpha(i1) rate-modifying mutations act in concert to allow receptor-independent, steady-state measurements of RGS protein activity. *J Biomol Screen.*, **14**, 1195-1206.
47. Mondal, S., Hsiao, K., and Goueli, S.A. (2015). A Homogenous Bioluminescent System for Measuring GTPase, GTPase Activating Protein, and Guanine Nucleotide Exchange Factor Activities. *ASSAY Drug Dev Technol.*, **13**, 444-455.

## CHAPTER 3. RAP1A ALLOSTERICALLY ACTIVATES PHOSPHOLIPASE C $\epsilon$ VIA ITS C-TERMINAL RA2 DOMAIN

### 3.1 Abstract

Phospholipase C $\epsilon$  (PLC $\epsilon$ ) responds to extracellular signals to produce second messengers that activate PKC and downstream signaling pathways. Two C-terminal Ras association (RA) domains, RA1 and RA2, which interact with scaffolding proteins or are activated by small GTPases, respectively, are involved in this response. However, their roles in regulating basal PLC $\epsilon$  activity are unknown. Using a domain deletion strategy and functional assays, we found that the RA1 domain significantly contributes to stability and activity relative to the RA2 domain. We next identified conserved, hydrophobic residues on the surface of the RA2 domain that are distant from the G protein binding site but could be involved in intra- or intermolecular interactions. Mutation of these hydrophobic residues had minimal impact on the basal activity but eliminated Rap1A-dependent activation. Small angle X-ray scattering was then used to gain insights into the molecular architectures of a PLC $\epsilon$  variant alone and in complex with Rap1A. Rap1A binding induces substantial conformational changes in PLC $\epsilon$ , resulting in a more compact activation complex. These results are consistent with Rap1A being an allosteric activator of PLC $\epsilon$ , and that activation likely requires interactions between hydrophobic surface residues of the RA2 domain and the PLC $\epsilon$  core.

### 3.2 Introduction

Phospholipase C (PLC) enzymes hydrolyze phosphatidylinositol lipids to generate the second messengers' diacylglycerol (DAG) and inositol phosphates, including inositol-1,4,5-triphosphate (IP<sub>3</sub>). IP<sub>3</sub> stimulates Ca<sup>2+</sup> release from internal stores, and DAG, together with Ca<sup>2+</sup>, activates protein kinase C (PKC) (1-5). Thus, PLC enzymes regulate numerous pathways including cell proliferation, differentiation, and survival (6,7). The PLC $\epsilon$  subfamily is the most recently identified member of the PLC family and is required for maximum calcium-induced calcium release in the cardiovascular system. However, chronic activation of PLC $\epsilon$  leads to the overexpression of genes that promote cardiac hypertrophy. Indeed, PLC $\epsilon$  expression is increased in patients with heart failure (3,5,8-10).

PLC $\epsilon$  shares a highly-conserved set of core domains with other isozymes of the PLC family, which consists of a pleckstrin homology (PH) domain, four tandem EF-hand repeats, the catalytic TIM barrel, and a C2 domain (5). PLC $\epsilon$  uniquely contains an N-terminal CDC25 domain and two C-terminal Ras association (RA) domains (1-5,11,12). The CDC25 domain is a guanine nucleotide exchange factor (GEF) for the small GTPase Rap1A (13-15), whereas the RA domains interact with scaffolding proteins or activated G proteins (8,11,15-22). These regulatory domains have been proposed to contribute to the basal regulation of PLC $\epsilon$ , as well as its activation following G protein-coupled receptor (GPCR) or receptor tyrosine kinase (RTK) stimulation (3,23).

The best-characterized pathway leading to PLC $\epsilon$  activation is mediated by Rap1A. Stimulation of  $\beta$ -adrenergic receptors activates adenylyl cyclase, leading to an accumulation of cyclic AMP (cAMP). In turn, cAMP activates exchange protein activated by cAMP (Epac), a GEF for Rap1A. Rap1A-GTP then binds to the C-terminal RA2 domain of PLC $\epsilon$ , activating and translocating the lipase to the perinuclear membrane (3,8,10,24,25). There, PLC $\epsilon$  hydrolyzes phosphatidylinositol-4-phosphate (PI<sub>4</sub>P), increasing DAG and activating PKC-dependent pathways. Rap1A and PLC $\epsilon$  have also been proposed to form a feed-forward activation loop, wherein Rap1A-GDP binds to the PLC $\epsilon$  CDC25 domain, is activated to Rap1A-GTP, and then binds to the C-terminal RA2 domain (19,20). This feed-forward loop is thought to underlie the increased expression of genes that result in cardiac hypertrophy (8,10,12,20,25-28). However, the molecular mechanism by which Rap1A-GTP stimulates the lipase activity of PLC $\epsilon$  remains unknown.

To better understand how the PLC $\epsilon$  RA domains contribute to regulation, we expressed and purified PLC $\epsilon$  domain deletion variants that lacked one or both RA domains, and characterized their basal activity and thermal stability. While the RA domains have similar folds (29), they have divergent functions, as the RA1 domain interacts with scaffolding proteins and the RA2 domain binds activated G proteins, including Rap1A (18-23,29). However, how Rap1A binding to the RA2 domain stimulates lipase activity is unknown. Guided by the structure of the RA2 domain alone and in complex with H-Ras (29), we identified highly conserved residues that may be involved in activation. Site-directed mutagenesis, thermal stability assays, activity assays, binding assays, and small angle X-ray scattering (SAXS) were used to begin investigating the molecular mechanism of Rap1A-dependent activation.

### 3.3 Results

#### 3.3.1 The Two RA Domains of PLC $\epsilon$ Have Different Roles in Stability and Basal Activity

Full-length PLC $\epsilon$  presents significant challenges for expression and purification, however, N-terminal truncations that retain lipase activity can be purified to homogeneity from baculovirus-infected insect cells (30). We expressed and purified PLC $\epsilon$  PH-COOH, which retains both RA domains (30), PH-COOH  $\Delta$ RA1, which lacks the RA1 domain, PH-COOH  $\Delta$ RA2, which lacks the RA2 domain, and PH-C2, which lacks both (Figure 3.1A) (30). The contribution of each domain to thermal stability was determined by measuring the melting temperature ( $T_m$ ) of each variant using differential scanning fluorimetry (DSF) (Figure 3.1B, Table 3.1) (31). Loss of both RA domains (PH-C2) significantly decreases the  $T_m$  by  $\sim 3$  °C compared to PH-COOH (Figure 3.1B, Table 3.1,  $p \leq 0.001$ ) (30). Similarly, deletion of the RA1 domain in PH-COOH  $\Delta$ RA1 decreased the  $T_m$  by  $\sim 4$  °C. In contrast, deletion of the RA2 domain in the PH-COOH  $\Delta$ RA2 variant did not change the thermal stability relative to PH-COOH (Figure 3.1B, Table 3.1). These results are consistent with the RA1 domain forming a stable interface with the PLC $\epsilon$  core, and the RA2 domain being more flexibly connected.

The basal activity of each PLC $\epsilon$  variant was then measured using a [ $^3$ H]-PIP $_2$  liposome hydrolysis assay (Figure 3.1C, Table 3.1) (17,32,33). Relative to PH-COOH ( $370 \pm 120$  nmol IP $_3$ /min/nmol PLC $\epsilon$  variant), PH-C2, which lacks both RA domains, had  $\sim 6$ -fold lower basal activity ( $62 \pm 25$  nmol IP $_3$ /min/nmol PLC $\epsilon$  variant,  $p \leq 0.0001$ ) (Figure 3.1C, Table 3.1) (30). The PH-COOH  $\Delta$ RA1 variant had a specific activity of  $16 \pm 4$  nmol IP $_3$ /min/nmol PLC $\epsilon$  variant ( $p \leq 0.0001$ ), a  $\sim 23$ -fold decrease in basal activity compared to PH-COOH (Figure 3.1C, Table 3.1). However, PH-COOH  $\Delta$ RA2 showed only a modest  $\sim 2$ -fold decrease in specific activity ( $200 \pm 64$  nmol IP $_3$ /min/nmol PLC $\epsilon$  variant,  $p \leq 0.001$ ) (Figure 3.1C, Table 3.1). Taken together with the thermal stability measurements, these results suggest that the decreased activity of PH-COOH  $\Delta$ RA1 is due to destabilization of the enzyme.

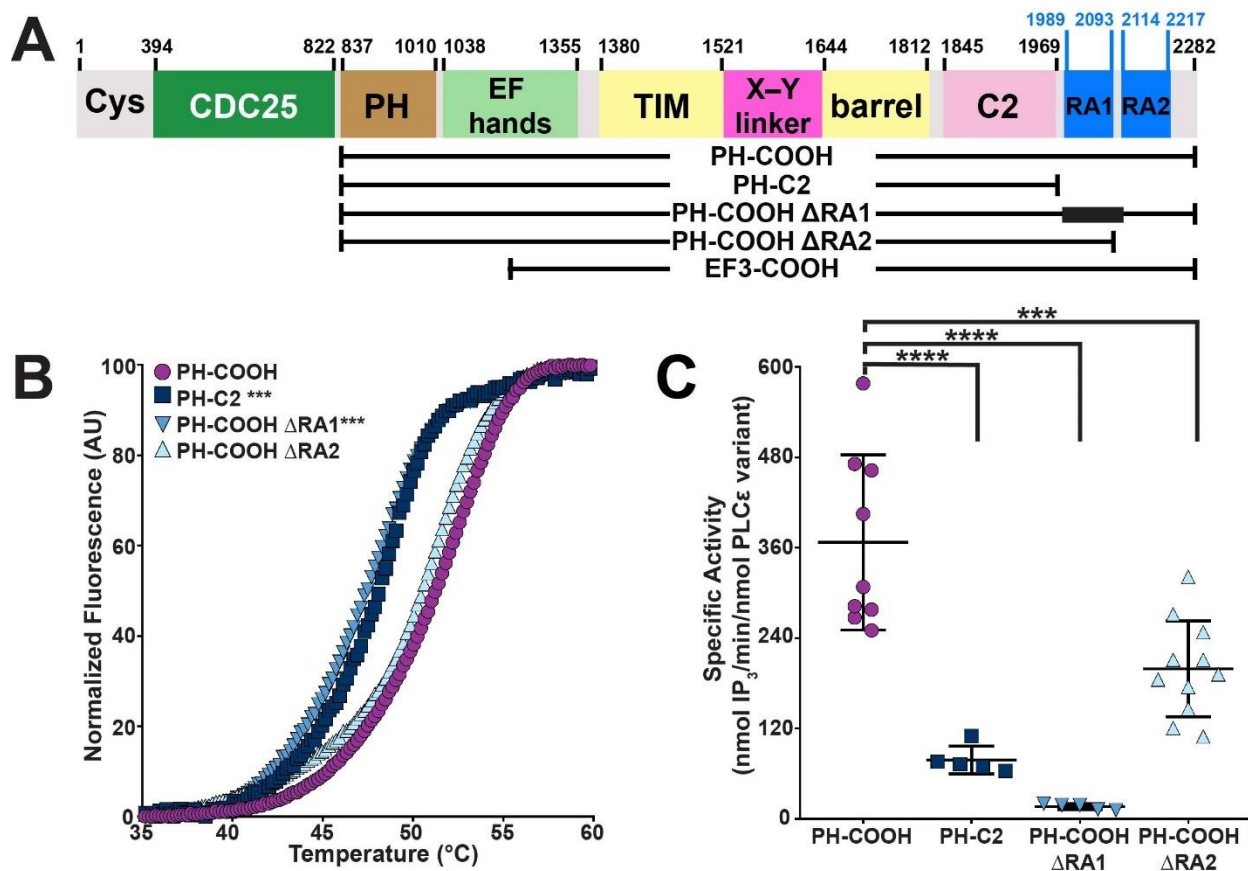


Figure 3.1. The PLC $\epsilon$  RA domains have different roles in stability and basal activity. (A) Domain structure of *R. norvegicus* PLC $\epsilon$ . The residue numbers above the diagram correspond to predicted domain boundaries. PLC $\epsilon$  variants used in this study are shown below. The black box in PLC $\epsilon$  PH-COOH  $\Delta$ RA1 corresponds to deletion of the RA1 domain. (B) Representative thermal melt curves of PH-COOH (purple circles), PH-C2 (navy blue squares), PH-COOH  $\Delta$ RA1 (blue inverted triangles), and PH-COOH  $\Delta$ RA2 (light blue triangles). Loss of the RA1 domain or both RA domains decreases thermal stability by  $3.9 \pm 0.7$  °C or  $2.9 \pm 0.6$  °C, respectively. Data represent at least three experiments performed in duplicate  $\pm$  S.D. (\*\*\*,  $p \leq 0.001$  based on one-way ANOVA followed by Dunnett's multiple comparisons test vs. PH-COOH). (C) Loss of both RA domains (PH-C2) or the RA1 domain (PH-COOH  $\Delta$ RA1) decreases basal specific activity 6-fold or 23-fold as compared to PH-COOH, respectively. Deletion of the RA2 domain (PH-COOH  $\Delta$ RA2) only decreased activity 2-fold compared to PH-COOH. Data represent at least three experiments performed in duplicate  $\pm$  S.D. (\*\*\*\*,  $p \leq 0.0001$ ; \*\*\*,  $p \leq 0.001$  based on one-way ANOVA followed by Dunnett's multiple comparisons test vs. PH-COOH).

Table 3.1. Basal Activity and Melting Temperature ( $T_m$ ) of PLC $\epsilon$  Variants

PLC $\epsilon$ Variant	Specific Activity $\pm$ S.D. (nmol IP <sub>3</sub> /min/nmol PLC $\epsilon$ variant)	$T_m \pm$ S.D. ( $^{\circ}$ C)
PH-COOH	370 $\pm$ 120	51.3 $\pm$ 0.72
PH-C2	62 $\pm$ 25 <sup>1</sup>	48.3 $\pm$ 1.0 <sup>2</sup>
PH-COOH $\Delta$ RA1	16 $\pm$ 4 <sup>1</sup>	47.4 $\pm$ 0.68 <sup>2</sup>
PH-COOH $\Delta$ RA2	200 $\pm$ 64 <sup>2</sup>	50.8 $\pm$ 0.37
PH-COOH K2150A	250 $\pm$ 86	50.5 $\pm$ 0.86
PH-COOH K2152A	260 $\pm$ 41	49.6 $\pm$ 0.79
PH-COOH Y2155A	250 $\pm$ 43	50.2 $\pm$ 0.98
PH-COOH L2158A	270 $\pm$ 120	51.2 $\pm$ 0.39
PH-COOH L2192A	270 $\pm$ 51	51.5 $\pm$ 0.71
PH-COOH F2198A	280 $\pm$ 130	51.5 $\pm$ 0.45
EF3-COOH	9 $\pm$ 5 <sup>1</sup>	51.7 $\pm$ 0.12

<sup>1</sup>p  $\leq$  0.0001, <sup>2</sup>p  $\leq$  0.001; based on one-way ANOVA followed by Dunnett's multiple comparisons test vs. PH-COOH.

### 3.3.2 Mutations on the RA2 Domain Surface Do Not Alter Activity or Stability

The RA2 domain contributes to basal activity, but not thermal stability (Figure 3.1, Table 3.1). The RA1 and RA2 domains were shown to be flexibly connected using nuclear magnetic resonance studies (29), and the RA2 domain may still form transient interactions with the rest of the PLC $\epsilon$  core, hence the modest decrease in the activity of the PH-COOH  $\Delta$ RA2 variant (Figure 3.1, Table 3.1). To identify residues on the RA2 domain that may be involved in intramolecular interactions, we generated a homology model of the domain alone and in complex with Rap1A·GTP (Figure 3.2A). This model was generated by superimposing the structure of Rap1A·GTP with that of H-Ras bound to the RA2 domain (PDB ID 1C1Y and 2C5L, r.m.s.d. 0.51 Å) (29,34). Previous cell-based studies identified two lysine residues on the RA2 domain, K2150, and K2152, which were proposed to engage the switch regions of activated GTPases (21,23,29). Specifically, the sidechain of K2150 forms electrostatic interactions with the switch region of H-Ras. Further analysis of the crystal packing of the H-Ras–RA2 structure (PDB ID 2C5L) revealed four conserved, solvent-exposed hydrophobic residues involved in lattice contacts: Y2155, L2158, L2192, and F2198. These residues are not predicted to contribute to G protein binding and may instead contribute to intra- or intermolecular interactions. To investigate the role of these residues, site-directed mutagenesis was used to introduce the Y2155A, L2158A, L2192A, and F2198A

mutants in the background of PLC $\epsilon$  PH-COOH. In addition, K2150 and K2152 were also mutated to alanine to further investigate the roles of the residues (21,23,29).

Mutation of any of the RA2 domain surface residues had no significant impact on the  $T_m$  (Figure 3.2B, Table 3.1), consistent with the  $T_m$  of the PH-COOH  $\Delta$ RA2 variant (Figure 3.1B, Table 3.1). The basal activity of these point mutants was measured using the [ $^3$ H]-PIP $_2$  liposome hydrolysis assay. The PH-COOH K2150A and K2152A mutants showed minimal changes in activity ( $250 \pm 86$  nmol IP $_3$ /min/nmol PLC $\epsilon$  variant and  $260 \pm 41$  nmol IP $_3$ /min/nmol PLC $\epsilon$  variant, respectively) compared to PH-COOH ( $370 \pm 120$  nmol IP $_3$ /min/nmol PLC $\epsilon$  variant); (Figure 3.2C, Table 3.1). Similar trends were reported for these mutants in the background of full-length PLC $\epsilon$  using the cell-based [ $^3$ H]-IP $_x$  assay (21,23). The PH-COOH Y2155A, L2158A, L2192A, and F2198A points mutants however exhibited basal activity ~2-fold lower than that of PH-COOH (Figure 3.2C, Table 3.1). These results are consistent with a minor role for the RA2 domain in maintaining basal activity (Figure 3.1, 3.2).

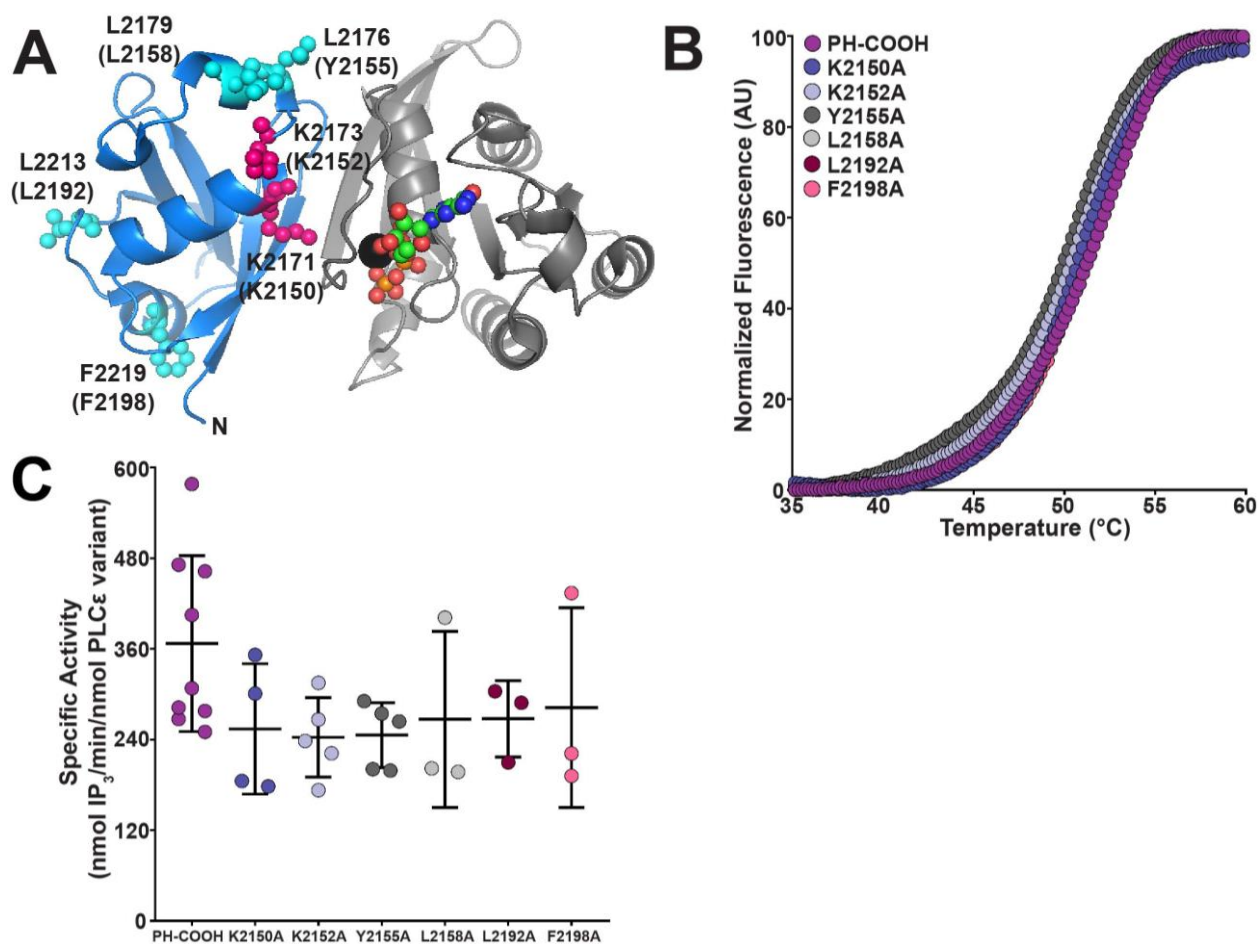


Figure 3.2. Mutation of conserved, hydrophobic residues on the RA2 domain does not alter activity or stability. (A) A model of Rap1A·GTP (gray) in complex with the PLC $\epsilon$  RA2 domain (blue). This model is based on the crystal structure of H-Ras bound to the RA2 domain (PDB ID 2C5L) and was generated by superimposing the structure of Rap1A·GTP with that of H-Ras (PDB ID 1C1Y). Analysis of the crystal packing in the H-Ras·GTP–RA2 structure revealed conserved, solvent-exposed hydrophobic residues distant from the G protein binding surface. These residues numbered as in *H. sapiens* and *R. norvegicus* (in parentheses), are shown as cyan spheres and could modulate intra- or intermolecular interactions important for basal and Rap1A dependent activity. The PLC $\epsilon$  RA2 residues K2150 and K2152, shown in hot pink spheres, have been shown to contribute to Rap1A-dependent activation. (B) Representative thermal melt curves of PH-COOH (purple circles), and the RA2 point mutants in the PH-COOH background: K2150A (slate blue circles), K2152A (lavender circles), Y2155A (dark gray circles), L2158A (light gray circles), L2192A (maroon circles) and F2198A (pink circles). Data represent at least three experiments performed in duplicate  $\pm$  S.D. (C) Mutation of residues on the RA2 domain had no significant impact on the basal specific activity. Data represent at least three experiments performed in duplicate  $\pm$  S.D.

### 3.3.3 Residues on the Surface of RA2 Are Required for Rap1A-dependent Activation

Rap1A activation of PLC $\epsilon$  has previously only been demonstrated in the cell-based [ $^3\text{H}$ ]-IP $_x$  assay (19,20,23). We used the [ $^3\text{H}$ ]-PIP $_2$  liposome-based activity assay to determine whether activation could be recapitulated *in vitro* using purified components. To ensure that Rap1A remained in its activated GTP-bound form, a constitutively active mutant of Rap1A (referred to as Rap1A<sup>G12V</sup>.GTP) was used in these experiments (35). Because the RA2 domain is the primary site for Rap1A binding, the PLC $\epsilon$  PH-COOH variant should show a Rap1A-dependent increase in lipase activity, whereas the PH-C2 variant should be unresponsive. Upon addition of increasing concentrations of Rap1A<sup>G12V</sup>.GTP, the PLC $\epsilon$  PH-COOH variant showed a ~3-fold increase in specific activity ( $1,900 \pm 300$  nmol IP $_3$ /min/nmol PLC $\epsilon$  variant, Figure 3.3, Table 3.2), consistent with the activation reported in cells (19,20,23), and an approximate EC $_{50}$  of  $1.60 \pm 0.58$   $\mu\text{M}$ . In contrast, PH-C2, which lacks both RA domains, showed no change in activity at all concentrations of Rap1A<sup>G12V</sup>.GTP tested (Figure 3.3, Table 3.2).

Mutation of PLC $\epsilon$  K2150 or K2152 was previously reported to decrease or eliminate G protein-dependent activation in cells (21,23). The PH-COOH K2150A and K2152A mutants showed similar results *in vitro* (Figure 3.3, Table 3.2). Lastly, as the hydrophobic residues on the RA2 surface do not appear to contribute to Rap1A binding (Figure 3.2A), they are not expected to contribute to Rap1A-dependent activation. However, PH-COOH Y2155A, L2158A, L2192A, and F2198A were insensitive to Rap1A.GTP at all concentrations tested (Figure 3.3, Table 3.2). Thus, the hydrophobic residues on the RA2 surface are required for Rap1A-stimulated lipase activity.

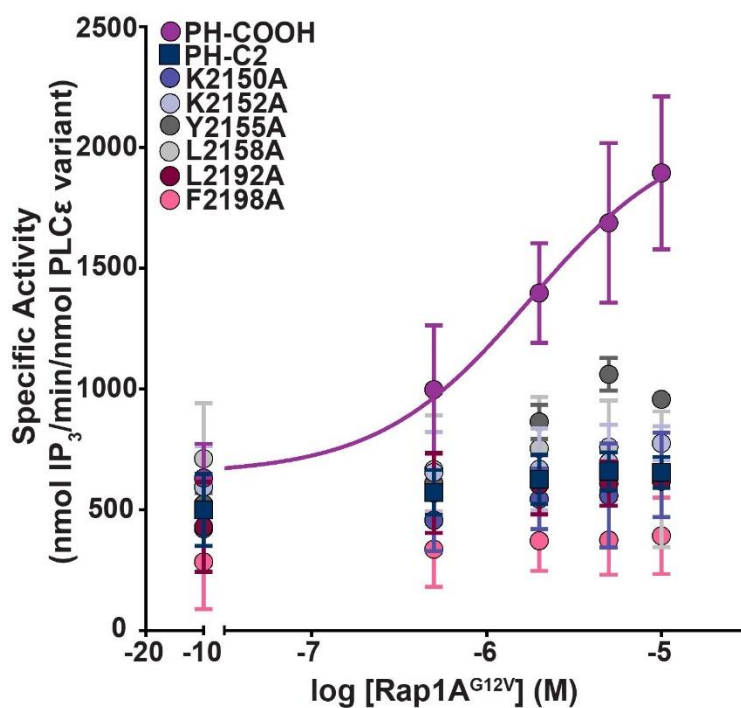


Figure 3.3. Residues in the RA2 domain contribute to Rap1A-dependent activation. PH-COOH (purple circles) is activated by Rap1A<sup>G12V</sup>·GTP in a concentration-dependent manner, whereas PH-C2 (navy blue squares) is unresponsive at all concentrations tested. Mutation of K2150 (slate blue circles) or K2152 (lavender circles) eliminates Rap1A<sup>G12V</sup>·GTP-dependent activation, as does mutation of Y2155 (dark gray circles), L2158 (light gray circles), L2192 (maroon circles), and F2198 (pink circles). All data represent the average of at least three experiments performed in duplicate  $\pm$  S.D.

Table 3.2. Rap1A-dependent Activity and IC<sub>50</sub> Values of PLC $\epsilon$  Variants

PLC $\epsilon$ Variant	Minimum activity $\pm$ S.D. (nmol IP <sub>3</sub> /min/nmol PLC $\epsilon$ variant)	Maximum activity $\pm$ S.D. (nmol IP <sub>3</sub> /min/nmol PLC $\epsilon$ variant)	Fold <sup>1</sup> Activation	IC <sub>50</sub> $\pm$ S.D. ( $\mu$ M)
PH-COOH	630 $\pm$ 140	1,900 $\pm$ 300	3.0	0.38 $\pm$ 0.19
PH-C2	540 $\pm$ 180	700 $\pm$ 120	1.3 <sup>3</sup>	5.0 $\pm$ 4.8 <sup>4</sup>
PH-COOH $\Delta$ RA1	N.D. <sup>5</sup>	N.D. <sup>5</sup>	N.D. <sup>5</sup>	N.D. <sup>5</sup>
PH-COOH $\Delta$ RA2	N.D. <sup>5</sup>	N.D. <sup>5</sup>	N.D. <sup>5</sup>	N.D. <sup>5</sup>
PH-COOH K2150A	420 $\pm$ 72	640 $\pm$ 180	1.5 <sup>4</sup>	0.56 $\pm$ 0.43
PH-COOH K2152A	590 $\pm$ 170	780 $\pm$ 70	1.3 <sup>3</sup>	0.52 $\pm$ 0.93
PH-COOH Y2155A	520 $\pm$ 46	960 $\pm$ 31	1.8 <sup>4</sup>	0.46 $\pm$ 0.18
PH-COOH L2158A	710 $\pm$ 230	630 $\pm$ 280	0.9 <sup>2</sup>	0.67 $\pm$ 0.31
PH-COOH L2192A	430 $\pm$ 190	620 $\pm$ 31	1.4 <sup>4</sup>	0.93 $\pm$ 0.67
PH-COOH F2198A	380 $\pm$ 130	390 $\pm$ 160	1.0 <sup>3</sup>	0.47 $\pm$ 0.18
EF3-COOH	38 $\pm$ 13	47 $\pm$ 11	1.2 <sup>3</sup>	N.D. <sup>5</sup>

<sup>1</sup>Fold activation of PLC $\epsilon$  variants by Rap1A<sup>G12V</sup>.GTP was calculated by dividing the maximum Rap1A-stimulated activity by the activity in the absence of Rap1A<sup>G12V</sup>.GTP. These specific activities are determined at a single time-point, in contrast to the basal activities reported in Table 1. <sup>2</sup>p  $\leq$  0.0001, <sup>3</sup>p  $\leq$  0.001, <sup>4</sup>p  $\leq$  0.01; based on one-way ANOVA followed by Dunnett's multiple comparisons test vs. PH-COOH. <sup>5</sup>Not determined.

### 3.3.4 Mutation of the RA2 Domain Does Not Change the Affinity for Rap1A<sup>G12V</sup>.GTP

To validate that the surface hydrophobic residues of PLC $\epsilon$  do not contribute to Rap1A binding, an AlphaScreen protein-protein interaction assay was used to measure the binding between PLC $\epsilon$  PH-COOH and the RA2 domain mutants with Rap1A<sup>G12V</sup>.GTP. Using this approach, PH-COOH was found to have an IC<sub>50</sub> of 0.38  $\pm$  0.19  $\mu$ M for Rap1A<sup>G12V</sup>.GTP (Figure 3.4, Table 3.2). In contrast, the addition of untagged Rap1A<sup>G12V</sup>.GTP to PH-C2 resulted in a significant increase in IC<sub>50</sub> of 5.0  $\pm$  4.8  $\mu$ M, consistent with the loss of the RA2 domain and therefore Rap1A<sup>G12V</sup>.GTP binding (Figure 3.4, Table 3.2) (8,11,12,18-22). PH-COOH K2150A and K2152A have similar IC<sub>50</sub> values (0.56  $\pm$  0.43  $\mu$ M and 0.52  $\pm$  0.93  $\mu$ M) for Rap1A<sup>G12V</sup>.GTP, comparable to that of PH-COOH (Figure 3.4, Table 3.2). Thus, the lysine residues are not required for Rap1A<sup>G12V</sup>.GTP binding under these conditions. This is consistent with a previous study wherein binding between the RA2 domain and H-Ras was characterized by isothermal titration calorimetry (29). In cell-based assays, alanine substitutions at these positions result in modest decreases in G protein activation (21,23). The binding affinity between the PH-COOH RA2 point

mutants and Rap1A<sup>G12V</sup>·GTP was also measured. PH-COOH Y2155A, L2185A, L2192A, and F2198A all bound Rap1A<sup>G12V</sup>·GTP with an affinity similar to that of PH-COOH (Figure 3.4, Table 3.2). The loss of Rap1A-dependent activation in these mutants is therefore not due to defects in binding.

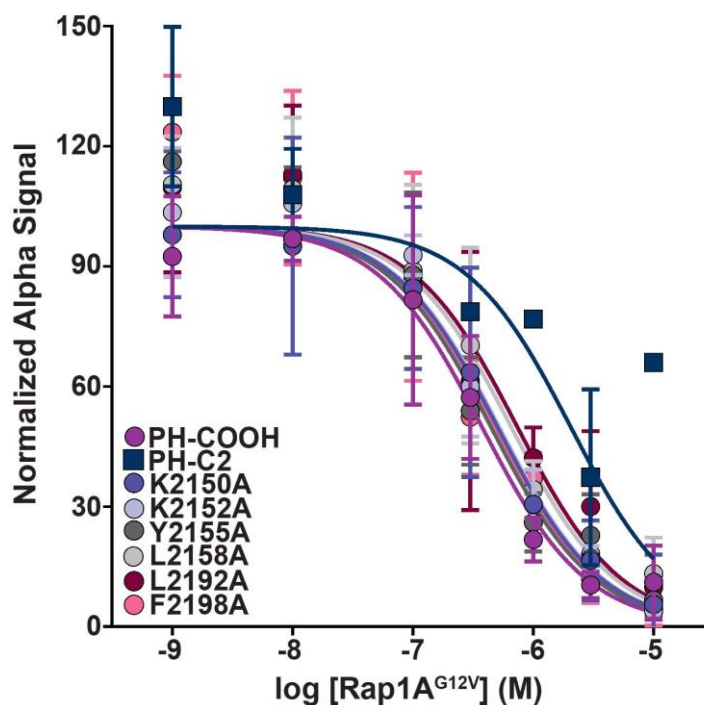


Figure 3.4. The PLC $\epsilon$  RA2 mutants are not defective in binding Rap1A<sup>G12V</sup>·GTP. A competition AlphaScreen protein-protein interaction assay was used to determine the binding affinities of PLC $\epsilon$  PH-COOH and the RA2 domain point mutants for Rap1A<sup>G12V</sup>·GTP. PLC $\epsilon$  PH-COOH (purple circles) binds to Rap1A<sup>G12V</sup>·GTP with an IC<sub>50</sub> of  $0.38 \pm 0.19 \mu\text{M}$  whereas PH-C2 (navy blue squares) binds to Rap1A<sup>G12V</sup>·GTP with an IC<sub>50</sub> of  $5.0 \pm 4.8 \mu\text{M}$ , demonstrating that Rap1A<sup>G12V</sup>·GTP does not bind PH-C2 as efficiently. The K2150A (slate blue circles) and K2152A (lavender circles) mutants bind to Rap1A<sup>G12V</sup>·GTP with an affinity comparable to PH-COOH. Mutation of the conserved hydrophobic residues on the RA2 domain surface to alanine had no impact on the binding affinity for Rap1A<sup>G12V</sup>·GTP, consistent with their location in the structure (PDB ID 2C5L) (29). Curves were normalized by setting the negative control (wells lacking GST- Rap1A<sup>G12V</sup>·GTP and untagged Rap1A<sup>G12V</sup>·GTP) to 0% and the positive control (wells lacking untagged Rap1A<sup>G12V</sup>·GTP to 100%. All data represent at least two independent experiments performed in duplicate  $\pm$  S.D.

### 3.3.5 Rap1A<sup>G12V</sup>.GTP Binding Induces Conformational Changes in PLC $\epsilon$

The RA2 domain is the primary site for Rap1A binding, but the lysines and hydrophobic residues on the RA2 surface are required for activation. It is possible that these hydrophobic residues link Rap1A binding to the rest of the PLC $\epsilon$  core, thereby increasing lipase activity. To test this hypothesis, small angle X-ray scattering (SAXS) was used to determine the solution architecture of a PLC $\epsilon$  domain deletion variant alone and in complex with Rap1A<sup>G12V</sup>.GTP. For these studies, a PLC $\epsilon$  domain deletion variant spanning EF3-COOH (residues 1284-2281) was used. This variant lacks the conformational heterogeneity associated with the PH domain and first two EF-hands (30) but retains the RA domains for improved stability. PLC $\epsilon$  EF3-COOH was purified from baculovirus-infected insect cells and shown to retain stability and lipase activity using DSF and the liposome-based activity assay. This variant also formed a stable, 1:1 stoichiometric complex between EF3-COOH and Rap1A<sup>G12V</sup>.GTP that could be isolated by size exclusion chromatography (SEC) (Figure 3.5).

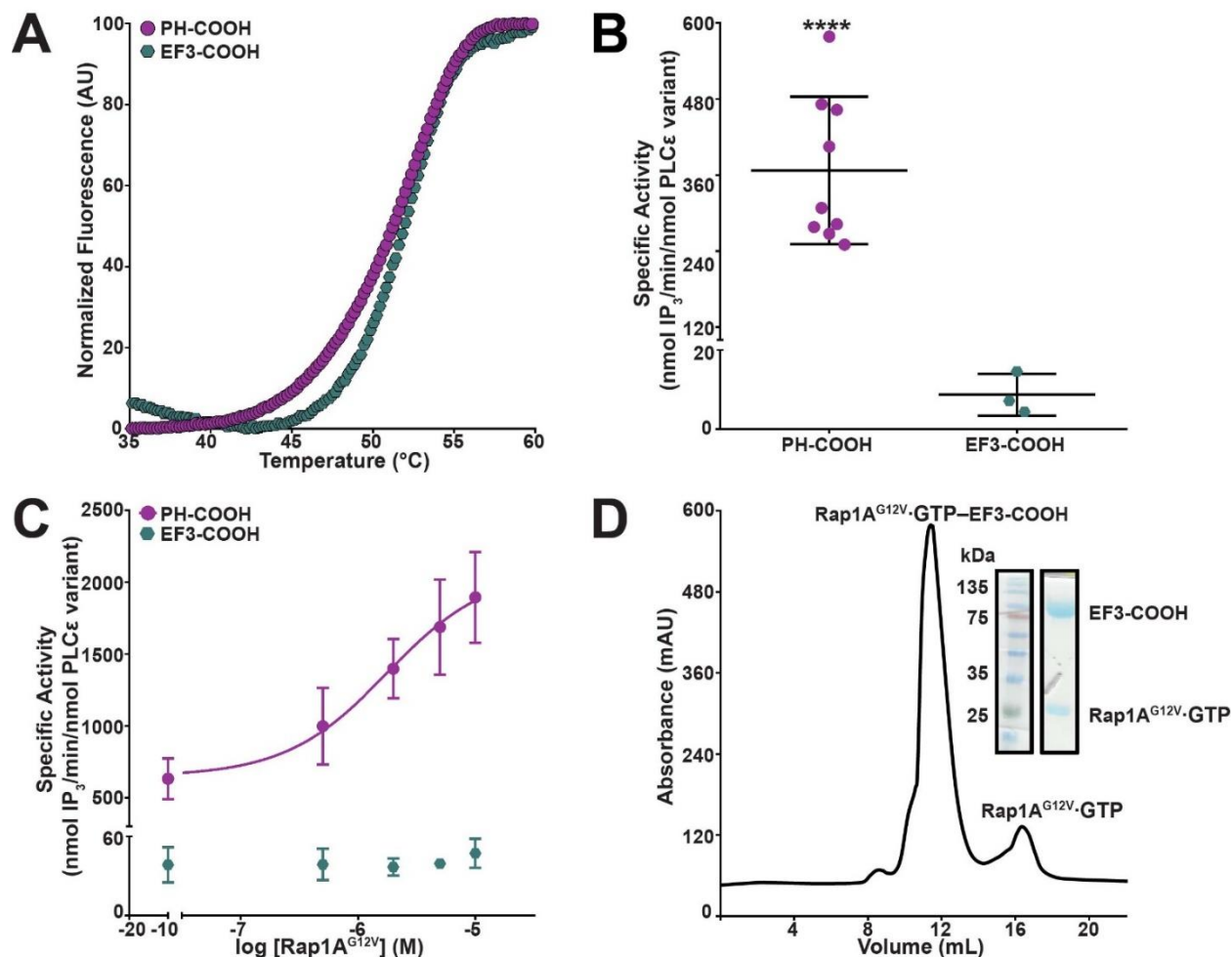


Figure 3.5. Characterization of PLC $\epsilon$  EF3-COOH. (A) Representative thermal melt curves of EF3-COOH (teal hexagons) and PH-COOH (purple circles). Deletion of the PH domain and EF hands 1/2 does not alter thermal stability. (B) PLC $\epsilon$  EF3-COOH has ~40-fold lower basal activity compared to PH-COOH. Data represent at least three experiments performed in duplicate  $\pm$  S.D. (\*\*\*\*,  $p \leq 0.0001$  based on one-way ANOVA followed by Dunnett's multiple comparisons test vs. PH-COOH). (C) PLC $\epsilon$  PH-COOH is activated by Rap1A<sup>G12V</sup>.GTP in a concentration-dependent manner, whereas EF3-COOH is unresponsive. Statistical tests were performed with all PLC $\epsilon$  variants from Figure 3.1 and 3.3, but shown on separate graphs for simplicity. (D) PLC $\epsilon$  EF3-COOH forms a stable, stoichiometric complex that can be isolated by size exclusion chromatography. Purified PLC $\epsilon$  EF3-COOH (112 kDa) and Rap1A<sup>G12V</sup>.GTP (21 kDa) were incubated to allow complex formation. The complex was isolated by size exclusion chromatography and peak fractions were analyzed by SDS-PAGE.

PLC $\epsilon$  EF3-COOH was found to be monomeric and monodisperse in solution (Figure 3.6A, Table 3.3) and the Rap1A<sup>G12V</sup>.GTP-EF3-COOH complex was also monodisperse (Figure 3.6B, Table 3.3) (36,37). The molecular weight of EF3-COOH and the Rap1A<sup>G12V</sup>.GTP-EF3-COOH

complex was determined by SEC-SAXS using the volume of correlation ( $V_c$ ) and the Porod volume ( $V_p$ ) (37,38). EF3-COOH had estimated molecular weights of 108 kDa ( $V_c$ ) and 118 kDa ( $V_p$ ), consistent with the calculated molecular weight of 112 kDa. The Rap1A<sup>G12V</sup>·GTP-EF3-COOH complex had an estimated molecular weight of 90 kDa ( $V_c$  and  $V_p$ ) compared to the calculated molecular weight of 133 kDa (37,38). The radius of gyration ( $R_g$ ) for EF3-COOH and the complex were determined from their respective Guinier plots (Figure 3.6C, D). EF3-COOH had an  $R_g$  of  $45 \pm 0.1$  Å (Figure 3.6C), while Rap1A<sup>G12V</sup>·GTP-EF3-COOH had a smaller  $R_g$  of  $39 \pm 0.2$  Å (Figure 3.6D).

The pair-distance distribution function provides information regarding the overall shape of the molecule and the maximum interparticle distance ( $D_{max}$ ). PLCε EF3-COOH is predominantly globular in solution with some extended features, consistent with the tail observed at high  $r$  values (Figure 3.6E) (37). Its  $D_{max}$  was found to be  $\sim 162$  Å, similar to the  $D_{max}$  values reported for PLCε PH-COOH and EF-COOH variants (30). In contrast, the pair distance distribution function for Rap1A<sup>G12V</sup>·GTP-EF3-COOH is consistent with a more compact structure in solution (Figure 3.6F). Indeed, the  $D_{max}$  for the complex is  $\sim 136$  Å,  $\sim 26$  Å smaller than that of EF3-COOH alone. This is consistent with the more compact *ab initio* bead model of Rap1A<sup>G12V</sup>·GTP-EF3-COOH compared to EF3-COOH (Figure 3.6G-H).

Figure 3.6. Rap1A<sup>G12V</sup>·GTP induces conformational changes in PLCε EF3-COOH. SAXS was used to determine the solution structures of PLCε EF3-COOH alone and in complex with Rap1A<sup>G12V</sup>·GTP. Raw scattering curves for (A) EF3-COOH and (B) Rap1A<sup>G12V</sup>·GTP-EF3-COOH. Guinier analyses of low  $q$  values,  $\ln(I)$  (beam intensity) vs.  $q^2$  (scattering angle) with a radius of gyration ( $R_g$ ) of (C) EF3-COOH and (D) Rap1A<sup>G12V</sup>·GTP-EF3-COOH. Fitting of the linear regressions to the data is represented by residuals, shown at the top of the plots, demonstrating the proteins are monomeric in solution. Pair-distance distribution functions ( $P(r)$ ) with estimated maximum interparticle distances ( $D_{max}$ ) for (E) EF3-COOH and (F) Rap1A<sup>G12V</sup>·GTP-EF3-COOH. When Rap1A<sup>G12V</sup>·GTP is bound to EF3-COOH, the  $D_{max}$  decreases by nearly  $\sim 26$  Å and results in a more compact, globular structure as evidenced by the more bell-shaped curve in the  $P(r)$  plot. *Ab initio* envelope models for (G) EF3-COOH and (H) Rap1A<sup>G12V</sup>·GTP-EF3-COOH confirm Rap1A<sup>G12V</sup>·GTP induces conformational changes with EF3-COOH.

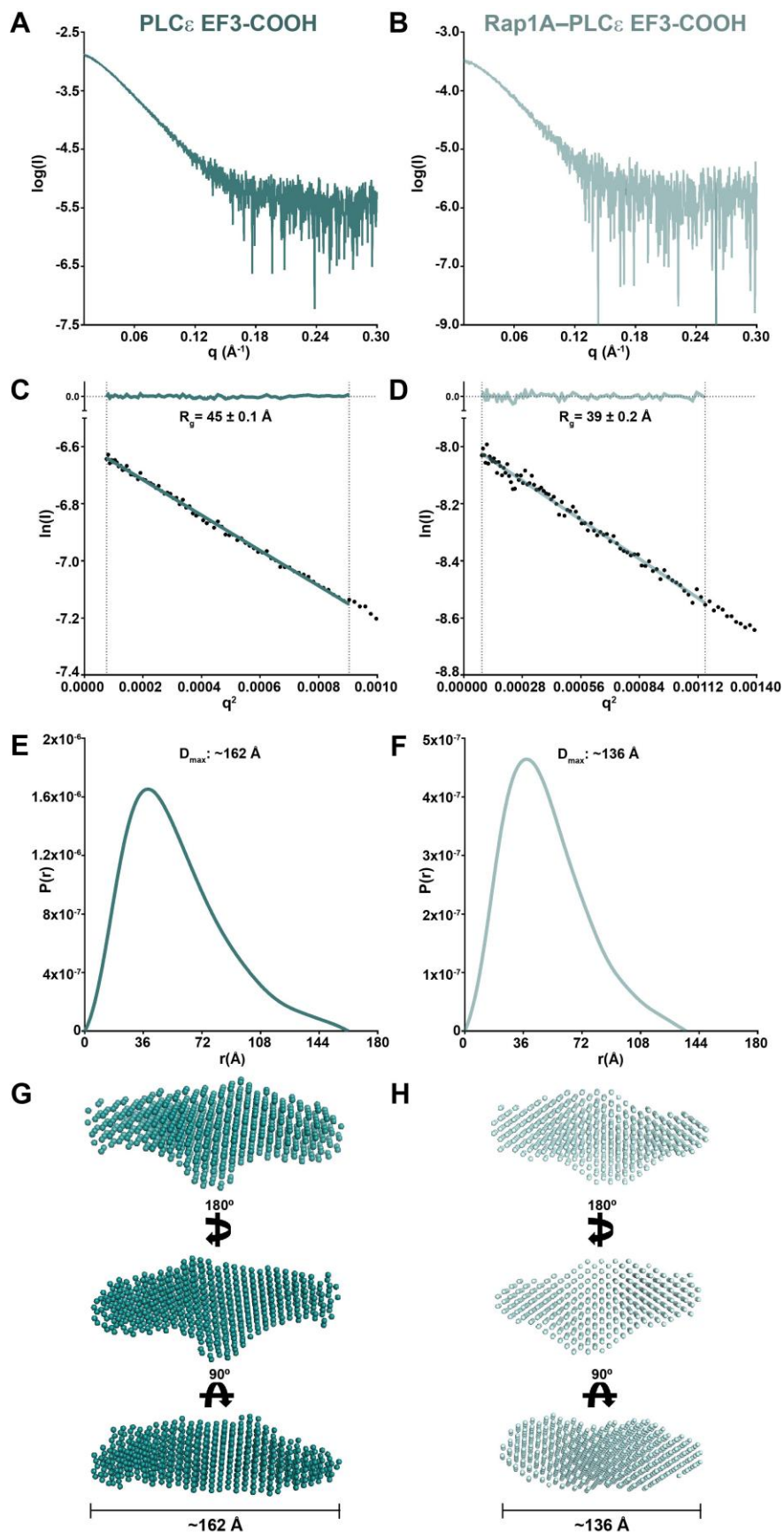


Table 3.3 SAXS Structural Parameters of PLC $\epsilon$  Variants

	PLC $\epsilon$ EF3-COOH	Rap1A <sup>G12V</sup> ·GTP-EF3-COOH
<i>Guinier analysis</i>		
$I(0)$ (cm <sup>-1</sup> )	$1.378 \times 10^{-3} \pm 2.903 \times 10^{-6}$	$3.436 \times 10^{-4} \pm 1.488 \times 10^{-6}$
$R_g$ (Å)	$44.72 \pm 0.1385$	$39.42 \pm 0.238$
$q$ min (Å <sup>-1</sup> )	$8.719 \times 10^{-3}$	$9.320 \times 10^{-3}$
$q$ range (Å <sup>-1</sup> )	$8.719 \times 10^{-3}$ - $3.006 \times 10^{-2}$	$9.320 \times 10^{-3}$ - $3.397 \times 10^{-2}$
<i>P(r) analysis</i>		
$I(0)$ (cm <sup>-1</sup> )	$1.400 \times 10^{-3}$	$3.440 \times 10^{-4}$
$R_g$ (Å)	44.60	39.36
$D_{max}$ (Å)	162	136
Porod volume (Å <sup>-3</sup> )	196000	170000
$q$ range (Å <sup>-1</sup> )	$8.719 \times 10^{-3}$ -0.3810	$9.320 \times 10^{-3}$ -0.3810

### 3.4 Discussion

PLC $\epsilon$  is regulated downstream of GPCRs and RTKs via direct interactions with small GTPases, including Rap1A, RhoA, and the Ras isoforms (21,23). The PLC $\epsilon$  RA1 and RA2 domains have emerged as important regulators of subcellular distribution and small G protein activation, respectively. However, their roles in basal activity are largely unknown, as is the mechanism by which G protein binding to the RA2 domain stimulates lipase activity.

In this work, the respective roles of the RA1 and RA2 domains in basal activity and thermal stability were investigated. The RA1 domain contributes to thermal stability, and its deletion decreases basal activity, likely due to destabilization of the PLC $\epsilon$  core. In contrast, removal of the RA2 domain does not change stability and has a modest role in maintaining basal activity. Thus, the RA2 domain may only transiently interact with other domains in PLC $\epsilon$  (Figure 3.1). We also showed that Rap1A activates the PH-COOH variant *in vitro* to the same extent reported in cells (19,20,23). Deletion of the RA domains in PH-C2 eliminated Rap1A-dependent activation, consistent with the loss of the RA2 domain.

Because the RA2 domain is required for activation by Rap1A<sup>G12V</sup>·GTP, we sought to identify residues that may allow the domain to interact with the PLC $\epsilon$  core and modulate activity. We identified conserved, hydrophobic residues on the RA2 surface that could be involved in these intramolecular interactions. Mutation of these residues had minimal impact on the basal properties of PLC $\epsilon$  PH-COOH and Rap1A binding but eliminated Rap1A-dependent activation. We also

tested the contributions of two lysine residues (K2150 and K2152) that were previously reported to contribute to G protein activation in cells. Mutation of these residues to alanine also eliminated Rap1A-dependent activation but had no impact on Rap1A-binding or basal properties (Figures 3.2-3.4). The simplest explanation for these results is that these residues are involved in communicating Rap1A<sup>G12V</sup>·GTP binding to the rest of the enzyme. Interaction of RA2 with the core of PLC $\epsilon$  is also consistent with the conformational changes observed by SAXS (Figure 3.6).

Taken together, these findings are consistent with a model of allosteric PLC $\epsilon$  activation by Rap1A (Figure 3.7). The RA2 domain is poised to link binding of activated Rap1A to the rest of the PLC $\epsilon$  core via intramolecular interactions, most likely mediated by its conserved surface hydrophobic residues. The lysine residues likely indirectly mediate activation given their proximity to the bound GTPase (29). This results in conformational changes in the Rap1A–PLC $\epsilon$  complex that increases lipase activity, potentially by relieving autoinhibition and/or increasing and optimizing interactions with the membrane. Future studies that provide higher resolution insights into PLC $\epsilon$  alone and in complex with Rap1A are essential for elucidating the molecular details of this process. Such studies will provide needed insights into how dysregulation of this interaction results in cardiovascular disease.

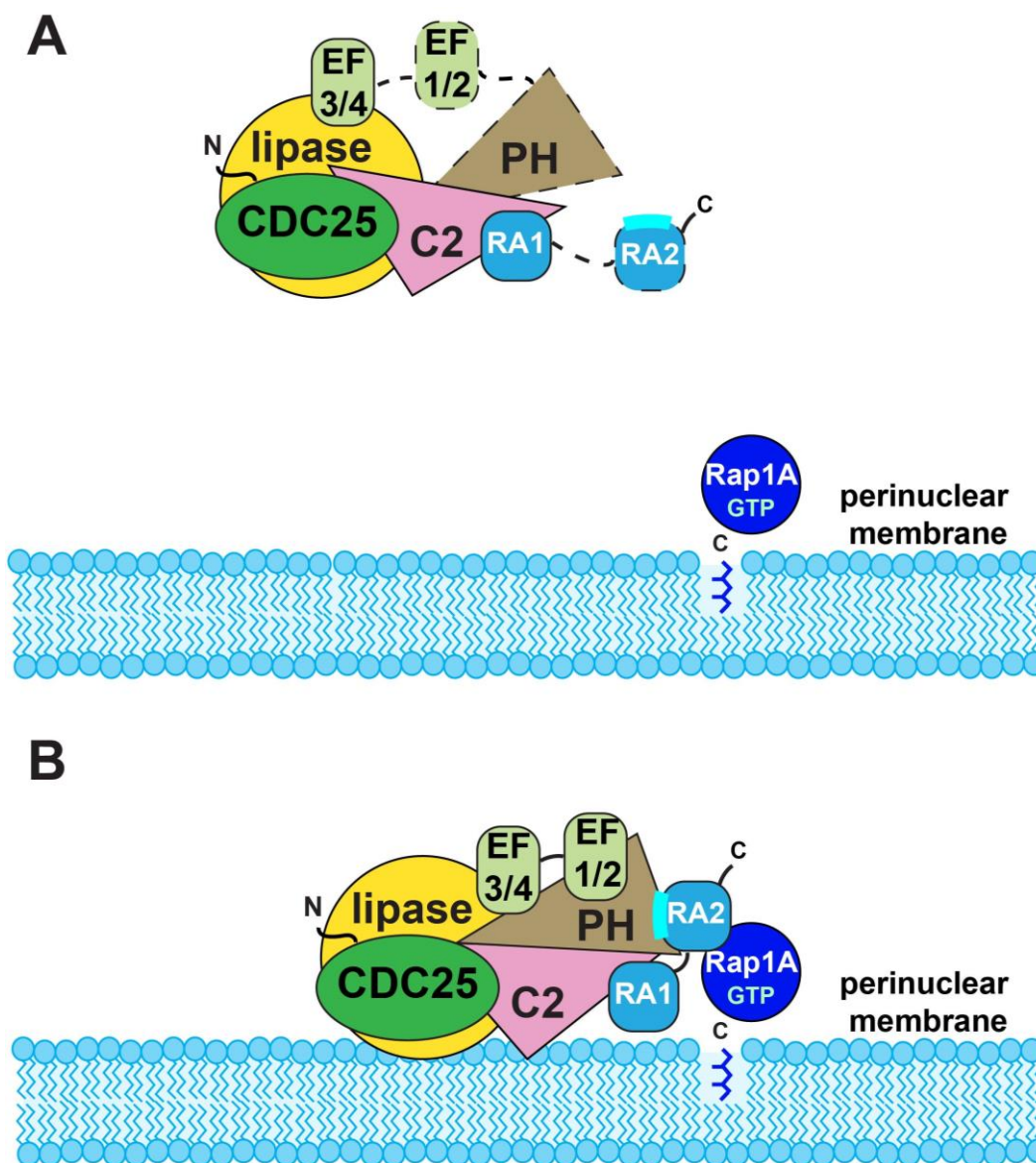


Figure 3.7. Model of by Rap1A-dependent activation of PLC $\epsilon$ . (A) Under basal conditions, PLC $\epsilon$  is present in the cytoplasm. The RA1 domain forms stable interactions with other domains in the PLC $\epsilon$  core, whereas the PH domain, first two EF-hands (EF1/2), and the RA2 domain are flexibly connected. Rap1A is prenylated at its C-terminus and is localized to the perinuclear membrane (45). (B) Following stimulation of  $\beta$  adrenergic receptors, Rap1A is activated and binds directly to the PLC $\epsilon$  RA2 domain. This binding induces conformational changes within PLC $\epsilon$ , some of which are mediated by the hydrophobic surface of the RA2 domain (cyan) interacting with the rest of the PLC $\epsilon$  core, thereby linking Rap1A binding to the lipase activity of the enzyme. In addition, the PH domain and EF1/2 may form more stable interactions with the core domains, as seen in crystal structures of the related PLC $\beta$  enzyme. These conformational changes may also facilitate interactions with the perinuclear membrane. Rap1A may also increase association with the membrane via its C-terminal prenyl group and help orient the PLC $\epsilon$  active site for maximum lipid hydrolysis.

### 3.5 Experimental Procedures

#### 3.5.1 Protein Expression, Purification, and Mutagenesis of PLC $\epsilon$ Variants

cDNAs encoding N-terminally His-tagged PLC $\epsilon$  variants from *R. norvegicus* were subcloned into pFastBac HTA (PH-COOH: residues 837-2281, PH-C2: 832-1972, PH-COOH  $\Delta$ RA1: 837-1988, 2098-2281; PH-COOH  $\Delta$ RA2: 837-2098). EF3-COOH (residues 1284-2281) was made using the Q5 Site-Directed Mutagenesis Kit (New England Biolabs), while the PH-COOH K2150A, K215A, Y2155A, L2158A, L2192A, and F2198A mutants were made using the QuikChange Site-Directed Mutagenesis Kit (Stratagene). All mutants were sequenced over the entire coding regions and expressed and purified as previously described (30).

For SAXS experiments, the N-terminal His-tag of PLC $\epsilon$  EF3-COOH was removed prior to purification over the ion exchange columns. Briefly, PLC $\epsilon$  EF3-COOH was incubated with 5% w/w TEV protease and dialyzed overnight in S200 buffer at 4 °C, and then subjected to further purification as previously described (30).

#### 3.5.2 Expression and Purification of Rap1A<sup>G12V</sup>.GTP

cDNA encoding N-terminally His-tagged constitutively active Rap1A (Rap1A<sup>G12V</sup>) from *H. sapiens* was subcloned into pFastBac HTA. cDNA encoding N-terminally GST-tagged *H. sapiens* Rap1A<sup>G12V</sup> was generated using the Q5 Site-Directed Mutagenesis Kit and subcloned into pFastbac Dual. Proteins were expressed in baculovirus-infected High5 cells. For both proteins, the cell pellet was resuspended in 20 mM HEPES pH 8.0, 100 mM NaCl, 10 mM  $\beta$ -mercaptoethanol, 0.1 mM EDTA, 10 mM NaF, 20 mM AlCl<sub>3</sub>, 0.1 mM LL, 0.1 mM PMSF, and 20  $\mu$ M GTP (lysis buffer) and lysed via dounce on ice. The lysate was centrifuged for 1 hour at 100,000 x g. The pellet was dounced again on ice using lysis buffer supplemented with 1% sodium cholate and solubilized at 4 °C for 1 hour. The sample was centrifuged again for 1 hour at 100,000 x g, and the supernatant was diluted 2X with lysis buffer. His-tagged Rap1A<sup>G12V</sup> was then loaded on a Ni-NTA pre-equilibrated with lysis buffer. The Ni-NTA column was washed with lysis buffer containing 10 mM imidazole and 0.2% cholate, then washed with lysis buffer containing 10 mM imidazole and 10 mM CHAPS (3-[(3-cholamidopropyl)dimethylammonio]-1-propanesulfonate). Rap1A<sup>G12V</sup> was then eluted with lysis buffer supplemented with 250 mM imidazole and 10 mM CHAPS. GST-Rap1A<sup>G12V</sup> was loaded onto a glutathione column pre-equilibrated with lysis buffer. The column

was washed with lysis buffer containing 0.2% cholate followed by lysis buffer supplemented with 10 mM CHAPS. GST-Rap1A<sup>G12V</sup> was eluted with lysis buffer supplemented with 20 mM reduced glutathione and 10 mM CHAPS.

Rap1A<sup>G12V</sup> and GST-Rap1A<sup>G12V</sup> were then concentrated and applied to tandem Superdex S200 columns pre-equilibrated with G protein S200 Buffer (20 mM HEPES pH 8.0, 50 mM NaCl, 1 mM MgCl<sub>2</sub>, 2 mM DTT, 10 mM CHAPS, and 20 μM GTP). Fractions containing purified protein were identified by SDS-PAGE, pooled, concentrated, and flash frozen in liquid nitrogen. Rap1A<sup>G12V</sup> used in the [<sup>3</sup>H]-PIP<sub>2</sub> hydrolysis assays was purified in 1 mM CHAPS.

For SAXS experiments and AlphaScreen displacement assays, the N-terminal His-tag was removed prior to purification over Superdex S200 Increase columns. Rap1A<sup>G12V</sup>.GTP was incubated with 5% w/w TEV protease and dialyzed overnight in dialysis buffer (20 mM HEPES pH 8.0, 50 mM NaCl, 1 mM MgCl<sub>2</sub>, 10 mM β-mercaptoethanol, 1 mM CHAPS, and 20 μM GTP at 4 °C, and then subjected to further purification.

### 3.5.3 Differential Scanning Fluorimetry

Melting temperatures ( $T_m$ ) of PLCε variants were determined as previously described (30,31). A final protein concentration of 0.5 mg/mL was used for each PLCε variant. The thermal melt curves were fit to a Boltzmann sigmoidal distribution, and the inflection point was used to calculate the  $T_m$ . All assays were performed in duplicate with protein from at least two independent purifications.

### 3.5.4 PLCε Basal Activity Assays

Basal activity of PLCε variants was measured as previously described (17,30,32,33). PLCε PH-COOH was assayed at a final concentration of 0.075 ng/μL, and the PH-C2, PH-COOH ΔRA1, PH-COOH ΔRA2, and EF3-COOH were assayed at a final concentration of 5 ng/μL. The PLCε PH-COOH K2150A, K2152A, Y2155A, L2158A, L2192A, and F2198A mutants were assayed at a final concentration of 0.5 ng/μL. All assays were performed in duplicate with protein from at least two independent purifications.

### 3.5.5 Rap1A<sup>G12V</sup>.GTP-dependent Activation of PLC $\epsilon$ Variants

Rap1A<sup>G12V</sup>.GTP-dependent increases in lipase activity were measured using the same approach as described for measuring basal specific activity (30,32), with some modifications. Briefly, the [<sup>3</sup>H]-PIP<sub>2</sub> liposomes were first incubated with increasing concentrations of Rap1A<sup>G12V</sup>.GTP in 50 mM HEPES pH 7.0, 3 mM EGTA, 1 mM EDTA, 100 mM NaCl, 5 mM MgCl<sub>2</sub>, 3 mM DTT, and 390  $\mu$ M CHAPS at 30 °C for 30 minutes. The reaction was initiated by addition of the PLC $\epsilon$  variant protein, incubated at 30 °C for 8 minutes, and quenched by the addition of 10% ice-cold trichloroacetic acid and 10 mg/mL BSA. All assays were performed in duplicate with protein from at least two independent purifications.

### 3.5.6 AlphaScreen Binding Assay

GST-tagged Rap1A<sup>G12V</sup>.GTP and His-tagged PLC $\epsilon$  PH-COOH, or PH-COOH point mutants were immobilized on AlphaScreen glutathione donor beads (PerkinElmer, cat no. 6765301) and nickel chelate AlphaLISA acceptor beads (PerkinElmer, cat no. AL108C), respectively. Binding between Rap1A<sup>G12V</sup>.GTP and the PLC $\epsilon$  variant brings the beads into close proximity, resulting in fluorescence. Addition of untagged Rap1A<sup>G12V</sup>.GTP then competes for binding to the PLC $\epsilon$  variant, decreasing the maximum fluorescence signal. Reactions were carried out in white 384-well ProxiPlates (PerkinElmer) using 20 mM HEPES pH 8, 50 mM NaCl, 2 mM DTT, 0.1 mM EDTA, 0.1 mM EGTA, 1 mM MgCl<sub>2</sub>, 0.5 mM CaCl<sub>2</sub>, 40  $\mu$ M GTP, ~0.02% CHAPS. 500 nM GST-Rap1A<sup>G12V</sup>.GTP was preincubated with serial dilutions of untagged Rap1A<sup>G12V</sup>.GTP (0 - 10  $\mu$ M) and 50 nM PLC $\epsilon$  variant on ice for 1 hour. 20  $\mu$ g/mL of nickel chelate AlphaLISA acceptor beads were added to each well and incubated for 1 hour in the dark and room temperature. 20  $\mu$ g/mL of the AlphaScreen glutathione donor beads were then added to each well and incubated for an additional 1 hour in the dark. Assay plates were read in an EnVision™ plate reader (PerkinElmer) and analyzed using GraphPad Prism v.8.0.1. Wells lacking GST- Rap1A<sup>G12V</sup>.GTP and untagged Rap1A<sup>G12V</sup>.GTP represented the negative control and wells lacking untagged Rap1A<sup>G12V</sup>.GTP represented the positive control. All curves shown were normalized by setting the negative control to 0% and the positive control to 100%. All assays were performed in duplicate with protein from at least two independent purifications.

### 3.5.7 Formation and Isolation of the Rap1A<sup>G12V</sup>.GTP-EF3-COOH Complex

A 1:3 molar ratio of purified PLC $\epsilon$  EF3-COOH and Rap1A<sup>G12V</sup>.GTP containing 0.5 mM CaCl<sub>2</sub> was incubated on ice for 30 minutes. The complex was resolved over a Superdex 200 column pre-equilibrated with complex S200 buffer (20 mM HEPES pH 8, 50 mM NaCl, 2 mM DTT, 0.1 mM EDTA, 0.1 mM EGTA, 1 mM MgCl<sub>2</sub>, 0.5 mM CaCl<sub>2</sub> and 40  $\mu$ M GTP). Fractions containing the purified complex were confirmed by SDS-PAGE, pooled, and concentrated for use in SAXS experiments.

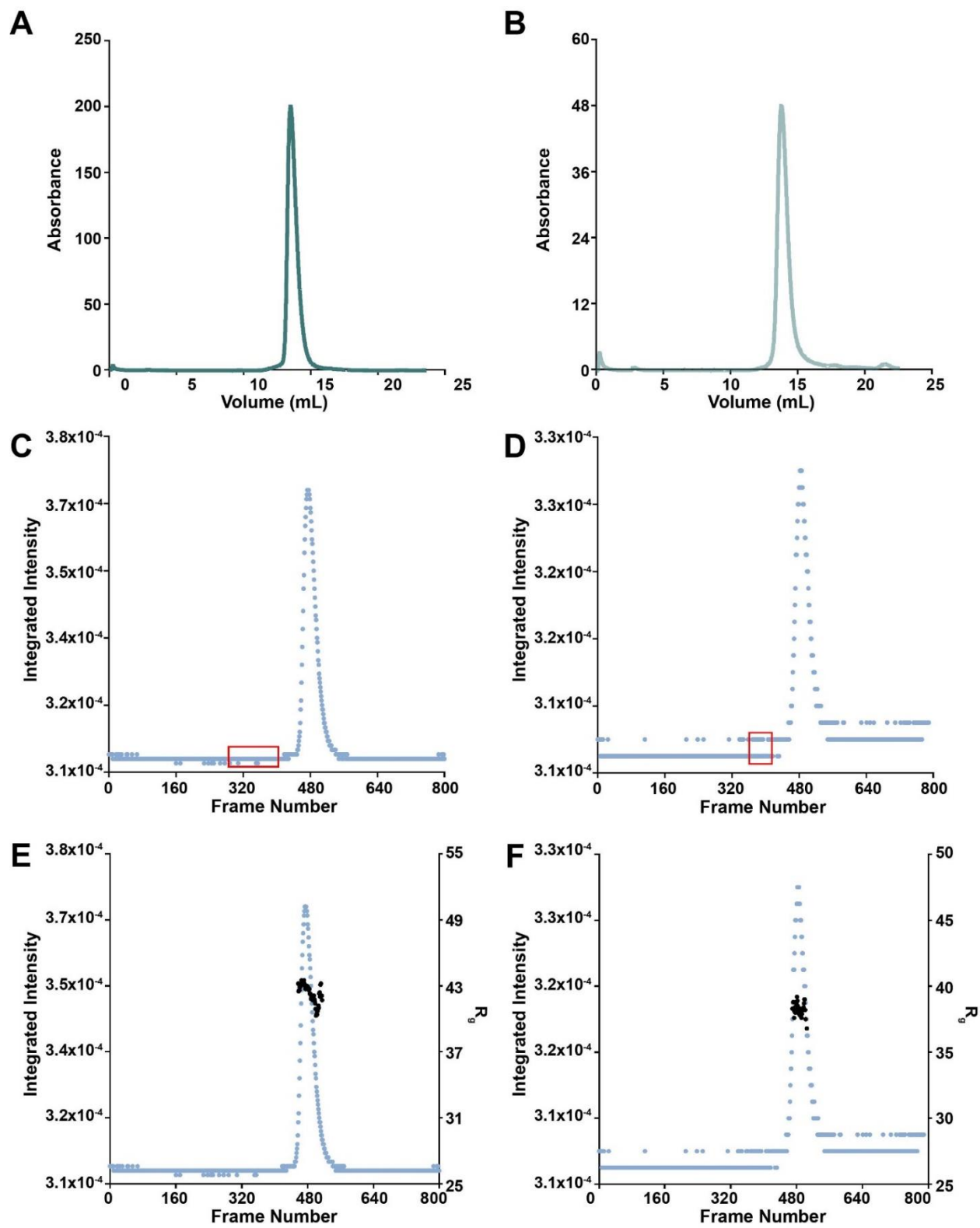
### 3.5.8 SAXS Data Collection and Analysis

Size exclusion chromatography (SEC)-SAXS was performed at BioCAT Advanced Photon Source (Sector 18) using an ÄKTA Pure FPLC (GE Healthcare) and a Pilatus3 1M detector (Dectris) with a beam size of 160  $\mu$ m x 75  $\mu$ m (Table 3.4). PLC $\epsilon$  EF3-COOH and Rap1A<sup>G12V</sup>.GTP-EF3-COOH were diluted to a final concentration of 2-3 mg/mL in S200 buffer and complex S200 buffer, respectively, and centrifuged at 16,000 x g for 5 min at 4 °C prior to data collection. Protein samples were eluted on a Superdex 200 Increase 10/300 GL column (GE Healthcare) at a flow rate of 0.5 mL/min (Figure 3.8). The eluate passed through a UV monitor followed by a SAXS flow cell consisting of a 1.5 mM ID quartz capillary with 10  $\mu$ m walls. Scattering intensity was recorded using Pilatus3 1M detector placed 3.5 m from the sample ( $q$ -range = 0.004  $\text{\AA}^{-1}$  to 0.4  $\text{\AA}^{-1}$ ) with a 12 KeV X-ray (1.033  $\text{\AA}$  wavelength). Data was collected every 2 s with 0.5 s exposure times. Regions flanking the elution peak were averaged to create buffer blanks which were subsequently subtracted from exposures selected from the elution peak to create log(I) vs  $q$  curves (Figure 3.6A). BioXTAS RAW 1.4.0 (39) was used for data processing and analysis. The  $R_g$  of individual frames were plotted with the “scattering chromatograms” (integrated intensity of individual exposures vs frame number) (Figure 3.8). PRIMUS (40) was used to calculate the  $R_g$ ,  $I_{(0)}$ , and  $D_{\max}$  for both samples. 10-15 *ab initio* models were calculated using DAMMIF (EF3-COOH NSD:  $0.940 \pm 0.018$ ; Rap1A<sup>G12V</sup>.GTP-EF3-COOH NSD:  $0.971 \pm 0.057$ ) (41), aligned and averaged with DAMAVER and final *ab initio* envelope structures were generated using DAMMIN (42,43). Graphical plots were generated from buffer-subtracted averaged data (raw scattering and Guinier plots) (44) or averaged envelope data ( $P(r)$  plots) and plotted using GraphPad Prism v.8.0.1.

Table 3.4. SAXS Data Collection and Analysis Parameters

<i>(a)</i> SAXS data collection parameters	
Instrument	BioCAT facility at the Advanced Photon Source beamline 18ID with Pilatus3 1M (Dectris) detector
Wavelength (Å)	1.033
Beam size (μm <sup>2</sup> )	160 (h) x 75 (v)
Camera length (m)	3.5
<i>q</i> -measurement range (Å <sup>-1</sup> )	0.004-0.4
Absolute scaling method	N/A
Basis for normalization to constant counts	To incident intensity, by ion chamber counter
Method for monitoring radiation damage	Automated frame-by-frame comparison of relevant regions
Exposure time, number of exposures	0.5 s exposure time with 2 s exposure period of entire SEC elution
Sample configuration	SEC-SAXS. Separation by size using ÄKTA Pure with a Superdex 200 Increase 10/300 GL column. SAXS data measured in a 1.5 mm ID quartz capillary
Sample temperature (°C)	20
<i>(b)</i> Software employed for SAXS data reduction, analysis, and interpretation	
SAXS data reduction	Radial averaging; BioXTAS RAW 1.4.0 (39) and ATSAS (44) used for frame comparison, averaging, and subtraction
Basic analysis: Guinier, M.W., P(r)	BioXTAS RAW 1.4.0 (39) used for Guinier fit and molecular weight; GNOM (43) used for P(r) function

Figure 3.8 Representative UV, size exclusion chromatography (SEC)-SAXS scattering and integrated intensity and  $R_g$  as a function of individual frames chromatograms for PLC $\epsilon$  EF3-COOH and the Rap1A<sup>G12V</sup>.GTP-EF3-COOH complex. (A) EF3-COOH and (B) Rap1A<sup>G12V</sup>.GTP-EF3-COOH complex UV chromatograms were obtained from SEC-SAXS experiments. Integrated intensity as a function of frame number for (C) EF3-COOH and (D) Rap1A<sup>G12V</sup>.GTP-EF3-COOH. Regions boxed in red were averaged and used for buffer subtraction. Integrated intensity and  $R_g$  (black) as a function of frame number is shown for (E) EF3-COOH and (F) Rap1A<sup>G12V</sup>.GTP-EF3-COOH.



### 3.5.9 Statistical Methods.

GraphPad Prism v.8.0.1 was used to generate all plots. One-way ANOVA was performed with Prism v.8.0.1 followed by Dunnett's post-hoc multiple comparisons vs. the PH-COOH variant as noted in figure captions. All error bars represent standard deviation.

### 3.6 Acknowledgments

This work is supported by an American Heart Association Predoctoral Fellowship Grant 18PRE33990057 (M.S.), American Heart Association Scientist Development Grant 16SDG29920017 (A.M.L.), Cancer Society Institutional Research Grant (IRG-14-190-56) to the Purdue University Center for Cancer Research (A.M.L.), and NIH 1R01HL141076-01 (A.M.L.). Use of the Advanced Photon Source, an Office of Science User Facility operated for the U. S. Department of Energy (DOE) Office of Science by Argonne National Laboratory, was supported by the U.S. DOE under Contract Number DE-AC02-06CH11357. This project was supported by grant 9 P41 GM103622 from the National Institute of General Medical Sciences of the National Institutes of Health. Use of the Pilatus 3 1M detector was provided by grant 1S10OD018090-01 from NIGMS. The content is solely the responsibility of the authors and does not necessarily represent the official views of the National Institute of General Medical Sciences or the National Institutes of Health.

### 3.7 Conflict of Interest

The authors declare that they have no conflicts of interest with the contents of this article.

### 3.8 Author Contributions

M.S. and A.M.L. designed the experimental approach. M.S., E.E.G.-K, A.S., and A.M. cloned, expressed, and purified all PLC $\epsilon$  and Rap1A proteins. M.S. and E.E.G.-K. performed DSF and activity assays. M.S. isolated Rap1A-PLC $\epsilon$  complexes and performed SAXS and direct binding experiments. M.S. and A.M.L. wrote the manuscript.

### 3.9 References

1. Rhee, S.G. (2001). Regulation of Phosphoinositide-Specific Phospholipase C. *Annu Rev Biochem.*, **70**, 281-312.

2. Bunney, T.D., Katan, M. (2011). PLC regulation: emerging pictures for molecular mechanisms. *Cell Press*, **36**(2), 88-96.
3. Smrcka, A.V., Brown, J.H., & Holz, G.G. (2012). Role of phospholipase C $\epsilon$  in physiological phosphoinositide signaling networks. *Cell Signal.*, **24**(6), 1333–1343.
4. Gresset, A., Sondek, J., Harden, T.K. (2012). The phospholipase C isozymes and their regulation. *Subcell Biochem.*, **58**, 61-94.
5. Kadamur, G., Ross, E.M. (2013). Mammalian Phospholipase C. *Annu Rev Physiol.*, **75**, 127-154.
6. Nakamura, Y., Fukami, K. (2017). Regulation and physiological functions of mammalian phospholipase C *J Biochem.*, **161**(4), 315-321.
7. Yang, Y.R., Follo, M.Y., Cocco, L., Suh, P. (2013). The physiological roles of primary phospholipase C. *Adv Biol Regul.*, **53**, 232-241.
8. Zhang, L. et al. (2013). Phospholipase C epsilon hydrolyzes perinuclear phosphatidylinositol 4-phosphate to regulate cardiac hypertrophy. *Cell*, **153**, 216-27.
9. Shibatohe, M., Kariya, K., Liao, Y., Hu, C., Watari, Y., Goshima, M., Shima, F., Kataoka, T. (1998). Identification of PLC210, a *Caenorhabditis elegans* Phospholipase C, as a putative effector of Ras. *J Biol Chem.*, **273**(11), 6218-6222.
10. Wing, M.R., Bourdon, D.M., Harden, T.K. (2003). PLC- $\epsilon$ : A Shared Effector Protein in Ras-, Rho-, and G $\alpha\beta\gamma$ -Mediated Signaling. *Mol. Interventions*, **3**(5), 273-280.
11. Dusaban, S.S., Brown, J.H. (2015). PLC $\epsilon$  mediated sustained signaling pathways. *Adv Biol Regul.*, **57**, 17-23.
12. Jin, T., Satoh, T., Liao, Y., Song, C., Gao, X., Kariya, K., Hu, C., Kataoka, T. (2001). Role of the CDC25 homology domain of phospholipase C $\epsilon$  in amplification of Rap1-dependent signaling. *J Biol Chem.*, **276**(32), 30301-30307.
13. Satoh, T., Edamatsu, H., Kataoka, T. (2006). Phospholipase C $\epsilon$  guanine nucleotide exchange factor activity and activation of Rap1. *Methods Enzymol.*, **407**, 281-290.
14. Dusaban, S.S., Kunkel, M.T., Smrcka, A.V. & Brown, J.H. (2015). Thrombin Promotes Sustained Signaling and Inflammatory Gene Expression through the CDC25 and Ras Associating Domains of Phospholipase C-epsilon. *J Biol Chem.*, **290**, 26776-83.
15. Seifert, J.P., Wing, M.R., Snyder, J.T., Gershburg, S., Sondek, J., Harden, T. K. (2004). RhoA activates purified phospholipase C $\epsilon$  by a guanine nucleotide-dependent mechanism. *J Biol Chem.*, **279**(46), 47992-47997.

16. Seifert, J.P., Synder, J.T., Sondek, J., Harden, T.K. (2006). Direct activation of purified phospholipase C epsilon by RhoA studied in reconstituted phospholipid vesicles. *Methods Enzymol.*, **406**, 260-271.
17. Seifert, J.P., Zhou, Y., Hicks, S.N., Sondek, J., Harden, T.K. (2008). Dual activation of phospholipase C-ε by Rho and Ras GTPases. *J Biol Chem.*, **283**(44), 29690-29698.
18. Edamatsu H, Satoh T, Kataoka T. (2006). Ras and Rap1 activation of PLCepsilon lipase activity. *Methods Enzymol.*, **407**, 99-107.
19. Song, C., Satoh, T., Edamatsu, H., Wu, D., Tadano, M., Gao, X., Kataoka, T. (2002). Differential roles of Ras and Rap1 in growth factor-dependent activation of phospholipase C epsilon. *Oncogene*, **21**, 8105-8113.
20. Kelley, G.G., Reks, S.E., Ondrako, J.M. & Smrcka, A.V. (2001). Phospholipase Cε: a novel Ras effector. *EMBO J.*, **20**, 743-54.
21. Zhang, L., Malik, S., Kelley, G.G., Kapiloff, M.S., Smrcka, A.V. (2011). Phospholipase Ce scaffolds to muscle-specific A kinase anchoring protein (mAKAPb) and integrates multiple hypertrophic stimuli in cardiac myocytes. *J Biol Chem.*, **286**(26), 23012-23021.
22. Kelley, G.G., Reks, S.E. & Smrcka, A.V. (2004). Hormonal regulation of phospholipase Cε through distinct and overlapping pathways involving G<sub>12</sub> and Ras family G-proteins. *Biochem J.*, **378**, 129-39.
23. Oestreich, E.A. et al. (2009). Epac and phospholipase C ε regulate Ca<sup>2+</sup> release in the heart by activation of protein kinase C and calcium-calmodulin kinase II. *J Biol Chem.*, **284**, 1514-22.
24. Oestreich, E.A. et al. (2007). Epac-mediated activation of phospholipase C ε plays a critical role in beta-adrenergic receptor-dependent enhancement of Ca<sup>2+</sup> mobilization in cardiac myocytes. *J Biol Chem.*, **282**, 5488-95.
25. Wang, H. et al. (2005). Phospholipase C ε modulates β-adrenergic receptor-dependent cardiac contraction and inhibits cardiac hypertrophy. *Circ Res.*, **97**, 1305-13.
26. Nash, C.A., Brown, L.M., Malik, S., Cheng, X., Smrcka, A.V. (2018). Compartmentalized cyclic nucleotides have opposing effects on regulation of hypertrophic phospholipase Ce signaling in cardiac myocytes. *J Mol Cell Cardiol.*, **7**(121), 51-59.
27. Rubio, R.G., Ransom, R.F., Malik, S., Yule, D.I., Anantharam, A., Smrcka, A.V. (2018). Phosphatidylinositol 4-phosphate is a major source of GPCR-stimulated phosphoinositide production. *Sci Signal.*, **11**(547), 1-11.
28. Smrcka, A.V. (2015). Regulation of phosphatidylinositol-specific phospholipase C at the nuclear envelope in cardiac myocytes. *J Cardiovasc Pharmacol.*, **65**, 203-10.

29. Bunney, T.D., Harris, R., Gandarillas, N.L., Josephs, M.B., Roe, S.M., Sorli, S.C., Paterson, H.F., Rodrigues-Lima, F., Esposito, D., Ponting, C.P., Gierschik, P., Pearl, L.H., Driscoll, P.C., Katan, M. (2006). Structural and mechanistic insights into ras association domains of phospholipase C epsilon. *Molecular Cell*, **21**, 495-507.
30. Garland-Kuntz, E.E., Vago, F.S., Sieng, M., Van Camp, M., Chakravarthy, S., Blaine, A., Corpstein, C., Jiang, W., Lyon, A.M. (2018). Direct observation of conformational dynamics of the PH domain in phospholipase C $\epsilon$  and  $\beta$  may contribute to subfamily-specific roles in regulation. *J Biol Chem.*, **293**(45), 17477-17490.
31. Mezzasalma, T.M. et al. (2007). Enhancing recombinant protein quality and yield by protein stability profiling. *J Biomol Screen.*, **12**, 418-28.
32. Ghosh, M., Smrcka, A.V. (2004). Assay for G protein-dependent activation of phospholipase C beta using purified protein components. *Methods Mol Biol.*, **237**, 67-75.
33. Lyon, A.M., Begley, J.A., Manett, T.D. & Tesmer, J.J. (2014). Molecular Mechanisms of Phospholipase C beta3 Autoinhibition. *Structure*, **22**, 1844-1854.
34. Nassar, N., Horn, G., Herrmann, C., Scherer, A., McCormick, F., Wittinghofer, A. (1995). The 2.2 Å crystal structure of the Ras-binding domain of the serine/threonine kinase c-Raf1 in complex with Rap1A and a GTP analog. *Nature*, **375**(6532), 554-60.
35. Khrenova, M.G., Mironov, V.A., Grigorenko, B.L., Nemukhin, A.V. (2014). Modeling the role of G12V and G13V Ras mutations in the Ras-GAP-catalyzing hydrolysis reaction of guanosine triphosphate. *Biochemistry*, **53**(45), 7093-9.
36. Skou, S., Gillilan, R.E., and Ando, N. (2014). Synchrotron-based small-angle X-ray scattering of proteins in solution. *Nat Protoc.*, **9**, 1727-1739.
37. Korasick, D.A., and Tanner, J.J. (2018). Determination of protein oligomeric structure from small-angle X-ray scattering. *Protein science: a publication of the Protein Society*, **27**, 814-824.
38. Mylonas, E., and Svergun, D. I. (2007). Accuracy of molecular mass determination of proteins by small-angle X-ray scattering. *J App Crystallogr.*, **40**, s245249.
39. Hopkins, J.B., Gillilan, R.E., Skou, S. (2017). *BioXTAS RAW*: improvements to a free open-source program for small-angle X-ray scattering data reduction and analysis. *J Appl Crystallogr.*, **50**, 1545-1553.
40. Konarev, P.V., Volkov, V.V., Sokolova, A.V., Koch, M.H.J., and Svergun, D.I. (2003). PRIMUS: a Windows PC-based system for small-angle scattering data analysis. *J Appl Crystallogr.*, **36**, 1277-1282.
41. Kozin, M.B., Svergun, D.I. (2001). Automated matching of high- and low- resolution structural models. *J Appl Crystallogr.*, **34**, 33-41.

42. Volkov, V.V., and Svergun, D.I. (2003). Uniqueness of ab initio shape determination in small-angle scattering. *J Appl Crystallogr.*, **36**, 860-864.
43. Svergun, D.I. (1999). Restoring low-resolution structure of biological macromolecules from solution scattering using simulated annealing. *Biophys J.*, **77**, 2896-2896.
44. Franke, D., Petoukhov, M.V., Konarev, P.V., Panjkovich, A., Tuukkanen, A., Mertens, H.D. T., Kikhney, A.G., Hajizadeh, N.R., Franklin, J.M., Jeffries, C.M., and Svergun, D.I. (2017). ATSAS 2.8: a comprehensive data analysis suite for small-angle scattering from macromolecular solutions. *J Appl Crystallogr.*, **50**, 1212-1225.

## CHAPTER 4. CONCLUSIONS AND FUTURE PERSPECTIVES

### 4.1 Conclusions

The work presented in this dissertation focus on understanding the molecular mechanisms regulating proteins downstream of GPCRs. Dysregulation of these enzymes has been implicated in a wide range of diseases and cancers. Therefore, understanding how these proteins are regulated structurally and biochemically can allow for the development of new therapeutic approaches. In Chapter 2, the binding of  $\text{Ca}^{2+}$  to RGS17 was characterized, and the role of this interaction in RGS17 activity and  $\text{G}\alpha$  binding was investigated. In Chapter 3, the molecular mechanism of Rap1A-dependent activation of  $\text{PLC}\epsilon$  was found to involve a conformational change in which conserved, hydrophobic residues in the RA2 domain surface of  $\text{PLC}\epsilon$  may be involved in mediating intramolecular interactions to stimulate lipid hydrolysis.

#### 4.1.1 $\text{Ca}^{2+}$ is a Positive Regulator of RGS17

In Chapter 2 of this work, the crystal structure of RGS17 bound to  $\text{Ca}^{2+}$  was solved to 1.53 Å. RGS17 crystallized as a dimer with strong electron density for four well-resolved  $\text{Ca}^{2+}$  ions. There are two  $\text{Ca}^{2+}$  ions bound to each chain in the asymmetric unit. One of the  $\text{Ca}^{2+}$  sites is formed by the backbone carbonyl of Tyr106 and the side chain of Glu109. This is located on the same face of the protein as the predicted  $\text{G}\alpha$  binding surface, and in close proximity to the residue responsible for GAP activity, Ser150. RGS17 bound to  $\text{Ca}^{2+}$  with a 50-fold greater affinity than  $\text{Mg}^{2+}$  in solution and  $\text{Ca}^{2+}$  bound RGS17 with greater affinity than other related RGS proteins (RGS4 and RGS2). Although  $\text{Ca}^{2+}$  did not have an impact on the thermal stability of RGS17, it did enhance the interaction between RGS17 and  $\text{G}\alpha_o$  and increased the GTPase activity of RGS17 towards  $\text{G}\alpha_o$ . These findings suggest that  $\text{Ca}^{2+}$  is a positive regulator of RGS17 activity and could represent a mechanism of feedback inhibition where elevated  $\text{Ca}^{2+}$  promotes RGS17– $\text{G}\alpha$  interactions to terminate  $\text{G}\alpha$  signaling.

#### 4.1.2 Rap1A Allosterically Regulates $\text{PLC}\epsilon$ Activity

In Chapter 3 of this work, biochemical and structural studies were used to investigate Rap1A-dependent activation of  $\text{PLC}\epsilon$ . Using a domain deletion approach, the RA1 domain of

PLC $\epsilon$  was found to be important for thermal stability and basal activity, while the RA2 domain was dispensable for thermal stability and had a modest effect on basal activity. Further investigation of the RA2 domain identified four conserved, hydrophobic residues on the RA2 surface that could be involved in intramolecular interactions with the PLC $\epsilon$  core to modulate activity. Mutation of these residues did not impact thermal stability, basal activity, or binding to Rap1A, but completely eliminated Rap1A-dependent activation of PLC $\epsilon$ . This suggests these residues may contribute to intramolecular interactions to promote lipid hydrolysis upon binding of Rap1A. SAXS studies showed conformational changes in PLC $\epsilon$  upon binding to Rap1A based on the decreased  $R_g$  and  $D_{max}$  values of PLC $\epsilon$  alone and in complex with Rap1A. These studies support a model in which Rap1A allosterically regulates PLC $\epsilon$ . Binding of Rap1A to the PLC $\epsilon$  RA2 domain could induce conformational changes that allow the conserved, solvent-exposed hydrophobic residues in the RA2 domain to interact with the PLC $\epsilon$  core, increasing lipase activity. Mutation of the hydrophobic residues may decrease lipase activity through disruption of the intramolecular interactions that result from Rap1A binding.

## 4.2 Future Perspectives

Chapter 2 of this work identified Ca<sup>2+</sup> as a novel potentiator of RGS17 activity. This opens the door to future studies investigating the role of Ca<sup>2+</sup> in RGS signaling. Although this work is the first to show direct binding of Ca<sup>2+</sup> to an RGS protein, previous studies have reported Ca<sup>2+</sup>/calmodulin as a regulator of some RZ and R4 subfamily members. Therefore, it would be interesting to determine if Ca<sup>2+</sup>, alone or with calmodulin, is a general regulator of RZ RGS proteins. Furthermore, other groups are using high throughput fragment screening to identify compounds that bind to RGS17. Since the findings of this work have shown that Ca<sup>2+</sup> enhanced the interaction of RGS17 with G $\alpha_o$ , it would also be interesting to investigate the impact of Ca<sup>2+</sup> on previously identified compounds ability to bind to RGS17. Finally, incorporating Ca<sup>2+</sup> in the fragment screening process could potentially lead to the identification of novel compounds that bind to RGS17.

Chapter 3 of this work focused on determining the molecular mechanism of Rap1A-dependent activation of PLC $\epsilon$  using biochemical and low-resolution structural approaches. These findings suggest a model in which Rap1A allosterically regulates PLC $\epsilon$ , wherein four solvent-

exposed, conserved, hydrophobic residues on the RA2 surface are involved in intramolecular interactions that promote lipase activity. To confirm these findings, future studies that provide higher resolution insights into PLC $\epsilon$  alone and in complex with Rap1A are needed. Although the proposed model in this work involves Rap1A inducing a conformational change in PLC $\epsilon$ , it does not explain how the conformational change promotes lipase activity. It is possible that the conformational change relieves autoinhibition and/or increases interactions with the membrane. Also, the other domain/residues involved in the intramolecular interactions with the four conserved, hydrophobic residues in the RA2 surface have yet to be identified. Furthermore, the studies presented in this dissertation only investigated the role of the RA domains in Rap1A-dependent activation. It would be interesting to investigate the role of other domains such as the CDC25 and PH domain in this interaction.

## VITA

Monita Sieng was born in San Jose, CA to Meng Leang Yoa and Thoueth Sieng. She is the sixth child of ten children. She graduated from San Jose State University with honors in May 2010 with a B.S. in Chemistry, Concentration in Biochemistry and Minor in Biology. In 2015, Monita was admitted to the Chemistry Graduate Program at Purdue University where she joined the lab of Dr. Angeline M. Lyon. After her graduate work, Monita is relocating back to San Jose, CA, where she plans to begin a career in promoting drug discovery.

## PUBLICATION

JBC ARTICLE



## Direct observation of conformational dynamics of the PH domain in phospholipases C $\epsilon$ and $\beta$ may contribute to subfamily-specific roles in regulation

Received for publication, April 23, 2018, and in revised form, September 17, 2018. Published, Papers in Press, September 21, 2018, DOI 10.1074/jbc.RA118.003656

Elisabeth E. Garland-Kuntz<sup>‡</sup>, Frank S. Vago<sup>§</sup>, Monita Sieng<sup>‡</sup>, Michelle Van Camp<sup>‡</sup>, Srinivas Chakravarthy<sup>¶</sup>, Arryn Blaine<sup>‡</sup>, Clairissa Corpstein<sup>‡</sup>, Wen Jiang<sup>§</sup>, and Angeline M. Lyon<sup>‡§1</sup>

From the Departments of <sup>‡</sup>Chemistry and <sup>§</sup>Biological Sciences, Purdue University, West Lafayette, Indiana 47907 and the <sup>¶</sup>Biophysics Collaborative Access Team, Illinois Institute of Technology, Sector 18ID, Advanced Photon Source, Argonne National Laboratory, Lemont, Illinois 60439

Edited by Wolfgang Peti

Phospholipase C (PLC) enzymes produce second messengers that increase the intracellular Ca<sup>2+</sup> concentration and activate protein kinase C (PKC). These enzymes also share a highly conserved arrangement of core domains. However, the contributions of the individual domains to regulation are poorly understood, particularly in isoforms lacking high-resolution information, such as PLC $\epsilon$ . Here, we used small-angle X-ray scattering (SAXS), EM, and functional assays to gain insights into the molecular architecture of PLC $\epsilon$ , revealing that its PH domain is conformationally dynamic and essential for activity. We further demonstrate that the PH domain of PLC $\beta$  exhibits similar dynamics in solution that are substantially different from its conformation observed in multiple previously reported crystal structures. We propose that this conformational heterogeneity contributes to subfamily-specific differences in activity and regulation by extracellular signals.

Phospholipase C (PLC)<sup>2</sup> enzymes hydrolyze phosphatidylinositol lipids at cell membranes, producing inositol phosphates and diacylglycerol, which in turn promote the release of Ca<sup>2+</sup> from intracellular stores and activate protein kinase C (PKC) (1). Of the six PLC subfamilies, PLC $\beta$  and PLC $\epsilon$  are required for normal cardiovascular function, and dysregulation of their

expression and/or activity can result in cardiac hypertrophy and heart failure (2–6). The activity of these lipases is autoinhibited by various domains and structural elements but can be stimulated up to ~60-fold following activation of cell surface receptors (1). PLC $\beta$  is activated downstream of G protein-coupled receptors (GPCRs) primarily through direct interactions with the heterotrimeric G protein subunits G $\alpha_q$  and G $\beta\gamma$  (1, 7). PLC $\epsilon$  is also activated downstream of GPCRs by G $\beta\gamma$  (8, 9), by the small GTPases RhoA and Rap1A, and by Ras GTPases following receptor tyrosine kinase activation (10).

Although the structural and molecular mechanisms by which PLC $\beta$  is regulated have been characterized at high resolution (1, 7, 11–14), structural insights into PLC $\epsilon$  regulation are lacking. PLC $\beta$  and PLC $\epsilon$  both contain a pleckstrin homology (PH) domain, followed by four tandem EF-hand repeats (EF1–4), a TIM barrel that houses the active site, and a C2 domain (Fig. 1A) (1, 11). Additional domains that flank this core contribute to subfamily-specific regulation. PLC $\beta$  has a ~400-amino acid C-terminal extension involved in autoinhibition (14), G $\alpha_q$ -dependent activation (12), and membrane association (13, 15–18). PLC $\epsilon$  contains an N-terminal CDC25 domain with guanine nucleotide exchange activity for Rap1A (19) and two C-terminal Ras association (RA) domains that interact with scaffolding proteins (4) and small GTPases (20, 21).

Crystal structures of PLC $\beta$  alone (22), in complex with G protein activators (12, 13, 23, 24) and/or physiologically relevant small molecules (24) show that the PH, EF-hands, TIM barrel, and C2 domains consistently assemble into a compact, globular structure. Deletion of any of these individual domains eliminates basal activity, whereas the C-terminal extension is dispensable (7, 25). Thus, interdomain contacts between the core domains appear essential for function. However, this view is being challenged by studies suggesting that the PLC $\beta$  PH domain is flexibly connected to the rest of the core and that this flexibility may be essential for its regulation (26–28). In support of this hypothesis, the related PLC $\delta$  enzyme contains a PH domain that is flexibly connected to the core and dispensable for activity but increases processivity by binding PIP<sub>2</sub> at the membrane (29–31).

In contrast, relatively little is known about the structure and molecular regulation of PLC $\epsilon$ . The pathways leading to G protein-mediated activation of PLC $\epsilon$  have been characterized

This work was supported by National Institutes of Health Grant 1R01 HL141076-01, American Heart Association Scientist Development Grant 16SDG29920017, and American Cancer Society Institutional Research Grant IRG-14-190-56 to the Purdue University Center for Cancer Research (to A. M. L.). The authors declare that they have no conflicts of interest with the contents of this article. The content is solely the responsibility of the authors and does not necessarily represent the official views of the National Institutes of Health.

<sup>1</sup> To whom correspondence should be addressed: Depts. of Chemistry and Biological Sciences, Purdue University, 560 Oval Dr., West Lafayette, IN 47907. Tel.: 765-494-5291; E-mail: lyonam@purdue.edu.

<sup>2</sup> The abbreviations used are: PLC, phospholipase C; PIP<sub>2</sub>, phosphatidylinositol 4,5-bisphosphate; IP<sub>3</sub>, inositol 1,4,5-triphosphate; GPCR, G protein-coupled receptor; RTK, receptor tyrosine kinase(s); DSF, differential scanning fluorimetry; SAXS, small-angle X-ray scattering; MALS, multiangle light scattering; DLS, dynamic light scattering; PKC, protein kinase C; PH, pleckstrin homology; RA, Ras association; T<sub>m</sub>, melting temperature; SEC, size-exclusion chromatography; PDB, Protein Data Bank; NSD, normalized spatial discrepancy; 2D and 3D, two- and three-dimensional, respectively; CTD, C-terminal domain; PE, phosphatidylethanolamine; PDB, Protein Data Bank; FSC, Fourier shell correlation; ANOVA, analysis of variance; CTF, contrast transfer function.

ASBMB  
Published in the U.S.A.

J. Biol. Chem. (2018) 293(45) 17477–17490 17477

## Conformational dynamics of PLC enzymes

(5, 10, 20, 32–34), but the activator-binding sites on PLC $\epsilon$  are largely unknown. It is also not known how the accessory domains contribute to regulation, in part because soluble, catalytically active variants have not been available for study. The only structural information for this enzyme comes from NMR structures of its two RA domains and a crystal structure of the RA2 domain in complex with Ras GTPase (35). Biochemical studies of PLC $\epsilon$  have shown that its CDC25 and PH domains, its first two EF-hands, and its RA domains are dispensable for lipase activity (35–37). Thus, PLC $\epsilon$  appears more similar to PLC $\delta$  than PLC $\beta$  with respect to the requirement for its PH domain in lipase activity.

In this work, we used biochemical assays, small-angle X-ray scattering (SAXS), and negative stain EM to obtain structural insights into the solution architecture of PLC $\epsilon$  and probe the roles of its PH and RA domains in regulating basal activity. We show that the PH domain, likely together with the first two EF-hands (EF1/2), is conformationally heterogeneous with respect to the rest of the PLC core, which retains a compact structure. In addition, the PH and RA domains have opposing effects on the thermal stability of the enzyme that indicate that one or both RA domains are intimately associated with the core, but the PH domain is not. To compare these results with that of a structurally well-characterized PLC, we also examined the solution structure of the PLC $\beta$ 3 core domains. In contrast to the structures observed across multiple different crystal forms, we show that the PLC $\beta$  PH domain also adopts multiple conformations in solution. Using site-directed mutagenesis and disulfide bond engineering, we found that both the extended and closed conformational states of the PLC $\beta$  PH domain retain basal activity and adsorb to liposomes, suggesting that these conformational states are functionally relevant. Thus, it seems likely that all PLC enzymes containing PH domains may be inherently dynamic in solution and that these conformational states may underlie subfamily-specific differences in their autoregulation, their association with cell membranes, and their allosteric regulation by other signaling proteins.

## Results

### The PLC $\epsilon$ PH and RA domains have differential impacts on basal activity, thermal stability, and liposome binding

Given the lack of prior knowledge about the tertiary organization of PLC $\epsilon$ , we investigated the respective contributions of the PH domain and the two RA domains to basal activity, the structural integrity of the enzyme, and binding to model membranes. Because the full-length enzyme presents significant challenges in expression and purification, we expressed and purified three PLC $\epsilon$  domain deletion variants: PH-COOH, which retains the core domains and both RA domains (residues 837–2282); PH-C2, which lacks both RA domains (residues 837–1972); and EF-COOH, which lacks the PH domain (residues 1035–2282) (Fig. 1A) (1, 8). Using a [ $^3\text{H}$ ]PIP $_2$  liposome hydrolysis assay (24, 38, 39), we found that the PH-COOH variant has the highest basal activity (Fig. 1B;  $390 \pm 123$  nmol of IP $_3$ /min/nmol of PLC $\epsilon$  variant). Loss of the RA domains in PH-C2 decreased basal activity 6-fold ( $65 \pm 23$  nmol of IP $_3$ /min/nmol of PLC $\epsilon$  variant,  $p \leq 0.0001$ ), whereas loss of the PH

domain in EF-COOH decreases activity 15-fold ( $25 \pm 12$  nmol of IP $_3$ /min/nmol of PLC $\epsilon$  variant,  $p \leq 0.0001$ ) (Fig. 1B).

To test whether the loss in specific activity is due to protein destabilization, the melting temperature ( $T_m$ ) of each variant was determined using differential scanning fluorimetry (DSF) (40). The PH-COOH and EF-COOH variants have similar  $T_m$  values of  $51.3 \pm 0.7$  and  $50.6 \pm 1.6$  °C, respectively (Fig. 1C), but PH-C2 has a lower  $T_m$  ( $48.3 \pm 1.0$  °C,  $p \leq 0.005$ ). This suggests that one or both RA domains directly contribute to the thermal stability of the enzyme. The resulting destabilization of the PLC core may be sufficient to account for the decreased basal activity of this variant. We next tested whether differences in basal activity were due to changes in the ability of the variants to bind PIP $_2$ -containing liposomes using a pelleting assay (41). We hypothesized that PH-COOH and PH-C2 would show the greatest binding to liposomes, as they retain the PH domain. However, in the presence of liposomes, all three variants were present to similar extents in the pellet, suggesting that differences in activity are not due to differences in binding (Fig. 1, D and E).

### PLC $\epsilon$ variants have molecular envelopes distinct from those predicted from PLC $\beta$ crystal structures

The PLC $\epsilon$  PH domain increases basal activity, but has no effect on thermal stability. We therefore hypothesized that the PH domain may be flexibly attached to the rest of the core. If so, then its molecular envelope should be characteristically different from that predicted by the crystal structures of PLC $\beta$  (46% sequence identity for the region spanning EF3 through the C2 domain). We used small-angle X-ray scattering (SAXS) to determine low-resolution *ab initio* bead models for the PLC $\epsilon$  PH-COOH, EF-COOH, and PH-C2 variants (Fig. 2, Tables 1 and 2, and Figs. S1–S4) (42). Size-exclusion chromatography (SEC)-SAXS was used to ensure sample homogeneity (Figs. S1 and S2). The minimal variability of radius of gyration ( $R_g$ ) as determined by Guinier approximation using the SAXS data (Fig. S3) or molecular weights as determined by multi-angle light scattering (MALS) (Fig. S4) across the elution peaks indicates that the samples were monodisperse. Guinier plots for each variant were also consistent with the absence of aggregates. PH-COOH and PH-C2 have  $R_g$  values of  $43 \pm 0.54$  and  $40 \pm 0.48$  Å, respectively, whereas EF-COOH had an  $R_g$  of  $46 \pm 2.5$  Å (Fig. 2 (D–F) and Table 2). All three PLC $\epsilon$  variants also had pair distance distribution functions consistent with a predominantly compact shape, but with some extended conformational aspects. The maximal intramolecular dimension ( $D_{\text{max}}$ ) for each variant was determined, with values of  $\sim 162$ ,  $\sim 148$ , and  $\sim 161$  Å, for PH-COOH, PH-C2, and EF-COOH, respectively (Fig. 2, G–I). The SAXS data were also used to estimate the molecular masses of the variants using the volume of correlation ( $V_c$ ) and the Porod volume ( $V_p$ ) (43). PH-COOH had molecular masses of 118 kDa ( $V_c$ ) and 126 kDa ( $V_p$ ), lower than the calculated molecular mass of 165.5 kDa. As an additional control, MALS was used to independently validate the molecular mass of this variant at 168 kDa (Fig. S4). PH-C2 had estimated molecular masses of 123.6 kDa ( $V_c$ ) and 137 kDa ( $V_p$ ), comparable with its calculated molecular mass of 130.8 kDa. Finally, EF-COOH had estimated molecular masses of 143.9

## Conformational dynamics of PLC enzymes

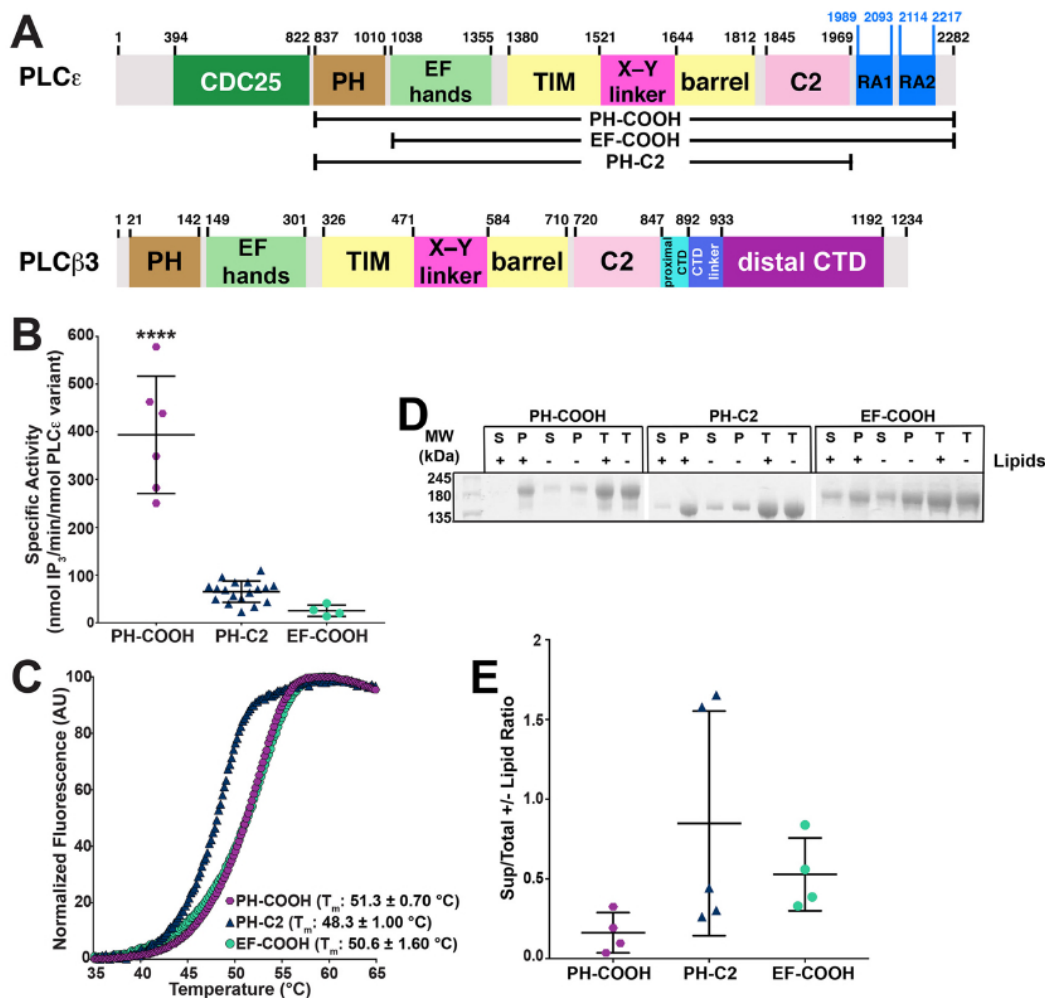


**Figure 1. Contributions of the PLC $\epsilon$  PH and RA domains to activity, stability, and liposome binding.** *A*, domain structure of *R. norvegicus* PLC $\epsilon$  and *Homo sapiens* PLC $\beta$ 3. The residue numbers above the diagrams correspond to predicted domain boundaries. PLC $\epsilon$  variants used in this study are depicted in brackets. *B*, deletion of RA domains (PH-C2) or PH domain (EF-COOH) decreases basal specific activity 6- and 15-fold relative to PH-COOH, respectively. Data represent at least four experiments performed in duplicate  $\pm$  S.D. (error bars) (\*\*\*\*,  $p \leq 0.0001$  based on one-way ANOVA followed by Tukey's multiple-comparison test). *C*, representative thermal melt curves of PH-COOH (purple hexagons), EF-COOH (green circles), and PH-C2 (blue triangles). Deletion of the RA domains decreases thermal stability by  $2.9 \pm 0.6$  °C, relative to PH-COOH. Data represent at least four experiments performed in duplicate  $\pm$  S.D. *D*, representative SDS-polyacrylamide gel of PLC $\epsilon$  variants following ultracentrifugation in the presence (+) or absence (-) of PE/PIP<sub>2</sub> liposomes. Total protein samples (T) contained protein incubated in the presence (+) or absence (-) of liposomes but were not subject to centrifugation. *E*, band density of PLC $\epsilon$  variants in the supernatant (S), pellet (P), and total protein (T) in the presence or absence of liposomes were quantified via ImageJ. The ratio of protein present in the supernatant samples versus the respective total protein control samples is shown. No significant differences in lipid binding for PLC $\epsilon$  variants were observed. Data represent at least three independent experiments.

kDa ( $V_p$ ) and 138.3 kDa ( $V_p$ ), again comparable with the calculated molecular mass of 143.4 kDa (44).

Comparison of the *ab initio* SAXS models of PH-COOH and PH-C2 reveals that they are very similar in overall shape (Fig. 2, J and K). PLC $\epsilon$  PH-COOH has a larger molecular volume ( $4.57 \times 10^5$  Å<sup>3</sup>) compared with PH-C2 ( $4.06 \times 10^5$  Å<sup>3</sup>), consistent with the presence of the RA domains in the PH-COOH variant (45). As a comparison, we fit the atomic structure of the

PLC $\beta$ 3 core within the density (including the PH-C2 domains from PDB entry 3OHH (12)), confirming that the PLC $\epsilon$  envelopes are substantially larger than would be predicted for PLC $\beta$ , which is consistent with their larger size (PLC $\beta$  PH-C2 is ~60 and ~77% of the total mass of PLC $\epsilon$  PH-COOH and PH-C2, respectively). Most interestingly, the SAXS envelopes of PH-COOH and PH-C2 both feature a well-defined, extended protrusion consistent with the extended tail observed in their pair

### Conformational dynamics of PLC enzymes

distance distribution functions (Fig. 2, G, H, J, and K). This feature is consistently observed in *ab initio* models of these variants, as evidenced by the normalized spatial discrepancy (NSD) values of  $0.968 \pm 0.032$  for PH-COOH and  $0.924 \pm$

$0.044$  for PH-C2 for 15 independently determined models (46). As this feature is observed in both PH-COOH and PH-C2, it cannot correspond to the RA domains (Figs. 1A and 2) and thus most likely represents the PH domain. The *ab initio* model of

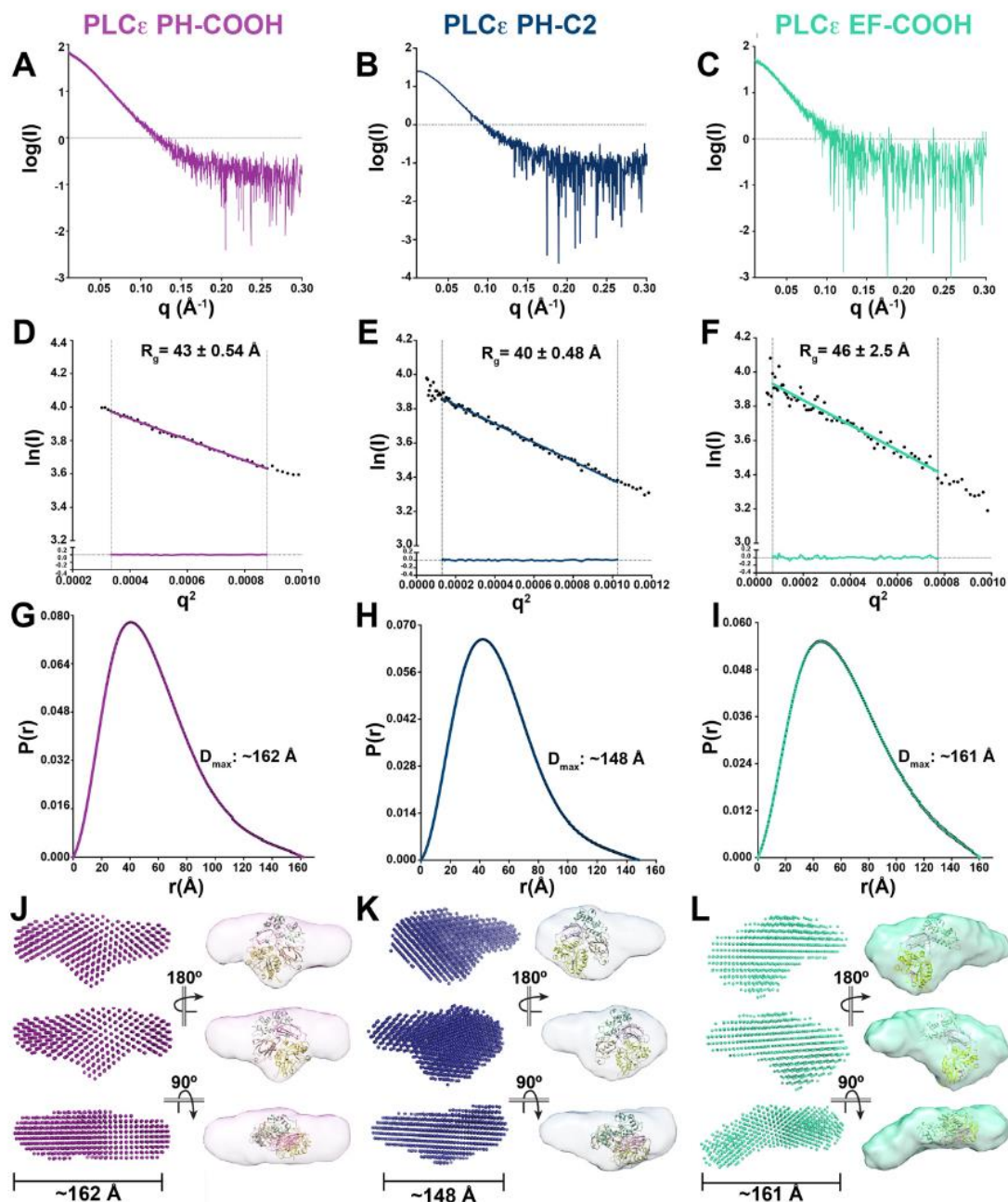


**Table 1**  
SAXS data collection and analysis parameters

SAS data collection parameters	
Instrument	BioCAT facility at the Advanced Photon Source beamline 18ID with Pilatus3 1M (Dectris) detector
Wavelength (Å)	1.033
Beam size (μm <sup>2</sup> )	160 (h) × 75 (v)
Camera length (m)	3.5
<i>q</i> measurement range (Å <sup>-1</sup> )	0.00365–0.383
Absolute scaling method	NA <sup>a</sup>
Basis for normalization to constant counts	To incident intensity, by ion chamber counter
Method for monitoring radiation damage	Automated frame-by-frame comparison of relevant regions
Exposure time, number of exposures	1-s exposure time with a 2-s total exposure period of entire SEC elution
Sample configuration	SEC-SAXS. Size separation by an ÅKTA Pure with a Superdex 200 Increase 10/300 GL column. SAXS data measured in a 1.5-mm inner diameter quartz capillary.
Sample temperature (°C)	20
Software employed for SAS data reduction, analysis, and interpretation	
SAXS data reduction	Radial averaging; frame comparison, averaging, and subtraction done using BioXTAS RAW 1.4.0 (55) and ATSAS (56)
Basic analysis: Guinier, molecular weight, <i>P</i> ( <i>r</i> )	Guinier fit and molecular weight using BioXTAS RAW 1.4.0 (55), <i>P</i> ( <i>r</i> ) function using GNOM (65)

<sup>a</sup> Not applicable.**Table 2**  
SAXS structural parameters of PLCε variants

	PLCε PH-COOH	PLCε PH-C2	PLCε EF-COOH
<b>Guinier analysis</b>			
<i>I</i> (0) (cm <sup>-1</sup> )	65.49 ± 0.27	51.1 ± 0.14	53.39 ± 0.48
<i>R</i> <sub>g</sub> (Å)	43.37 ± 0.54	40.46 ± 0.48	46.44 ± 2.51
<i>q</i> min (Å <sup>-1</sup> )	0.0183	0.0114	0.0083
<i>q</i> range (Å <sup>-1</sup> )	0.0183–0.0296	0.0114–0.0320	0.0083–0.0278
<b><i>P</i>(<i>r</i>) analysis</b>			
<i>I</i> (0) (cm <sup>-1</sup> )	65.77	51.20	54.47
<i>R</i> <sub>g</sub> (Å)	44.64	41.29	49.31
<i>D</i> <sub>max</sub> (Å)	162	148	161
Porod volume (Å <sup>-3</sup> )	213,000	213,000	277,000
<i>q</i> range (Å <sup>-1</sup> )	0.0183–0.184	0.0114–0.197	0.0083–0.172

the EF-COOH variant shares approximately the same long dimension as the PH-COOH variant. EF-COOH also contains a similar extended protrusion from the main body of the envelope, with an NSD of  $0.627 \pm 0.039$  for 10 independent models (Fig. 2 (F, I, and L) and Table 2). However, electron density appears to be lost both from the protrusion and from the center of the molecule, relative to the models of PH-COOH and PH-C2 (Fig. 2, J–L). This is supported by the decreased molecular volume of the EF-COOH variant ( $3.48 \times 10^5 \text{ Å}^3$ ) (45). These differences are most likely a direct consequence of deleting the PH domain in EF-COOH.

#### Negative stain EM reconstruction of PLCε variants

To obtain higher resolution and orthogonal structures of the PLCε variants, we used negative stain EM (Fig. 3 and Fig. S5) to calculate single-particle reconstructions. Preliminary analysis of the data sets revealed challenges in obtaining dominant 3D class averages for each set of particles. Together with the SAXS data, this is consistent with conformational heterogeneity in

the PLCε variants and necessitated a conservative approach to data processing and calculating 3D reconstructions (Fig. S5).

For the PH-COOH variant, 2D classes containing 34,155 particles were used to generate two initial 3D models, each of which was used to independently calculate two refined 25 Å 3D reconstructions (9,879 and 13,628 particles each) (Fig. 3 (A, D, G, and J) and Fig. S6). Similarly, for the PH-C2 variant, 92,982 particles from the 2D classes were used to generate two refined 20 Å 3D reconstructions (24,129 and 22,343 particles each) (Fig. 3 (B, E, H, and K) Fig. S6). These reconstructions confirm that PH-COOH and PH-C2 are monomeric. The two PH-COOH reconstructions have molecular volumes of  $2.92 \times 10^5$  and  $3.40 \times 10^5 \text{ Å}^3$ , respectively, and maximum diameters of ~116 Å. The two reconstructions of PH-C2 have molecular volumes of  $3.07 \times 10^5$  and  $2.78 \times 10^5 \text{ Å}^3$  and diameters of ~116 and ~124 Å (45). Overall, these reconstructions have smaller molecular volumes compared with the SAXS envelopes. This is most likely due to the dehydration and sample flattening that is common in negative stain (47). Although the PH-COOH variant retains the RA domains, there are no obvious differences compared with PH-C2, further supporting our hypothesis that one or both RA domains stably associate with the rest of the core under these experimental conditions (Figs. 1 and 3). Thus, distinctive features protruding from the main body of the reconstructions of both PH-COOH and PH-C2 likely reflect the conformational heterogeneity of the PH domain with respect to the PLCε core (Fig. 3 and Fig. S6).

Two refined 20 Å reconstructions of the EF-COOH variant (13,416 and 14,498 particles each) were likewise generated from 2D classes containing 53,028 particles (Fig. 3 (C, F, I, and L) and Fig. S6). Like the other PLCε variants, the EM analysis independently confirms that EF-COOH is monomeric. Similar to the

**Figure 2. SAXS envelopes reveal the solution architectures of PLCε variants.** A–C, raw scattering curves for PLCε PH-COOH (A), PH-C2 (B), and EF-COOH (C). D–F, Guinier analyses of low *q* values,  $\ln(I)$  (beam intensity) versus  $q^2$  (scattering angle) with *R*<sub>g</sub> of PH-COOH, PH-C2, and EF-COOH, respectively. Fitting of the linear regressions to the data is represented by residuals, shown at the bottom of the plots, demonstrating that the proteins are monomeric in solution. G–I, pair distance distribution functions (*P*(*r*)) indicating elongated envelopes for PH-COOH, PH-C2, and EF-COOH variants, respectively. Estimated maximum intramolecular distances (*D*<sub>max</sub>) are provided. *Ab initio* envelope models (left) and equivalent envelopes rendered as volumes (right) show protrusions in PH-COOH (J) and PH-C2 (K) and lack of density, likely corresponding to the missing RA domains in PH-C2. As a reference, the crystal structure of the PLCβ3 core (colored as in Fig. 1A; PDB entry 3OHH (12)) is fit within the SAXS-derived envelopes such that the PH domain is oriented toward the extended protrusion and the C2 domain toward the additional density on the opposite side of the envelope. In L (EF-COOH), the domain is extended similarly to PH-COOH, but electron density is lost from the protrusion and the center of the molecule due to loss of the PH domain. The PLCβ3 core lacking the PH domain is fit within the density as described for J and K.

## Conformational dynamics of PLC enzymes

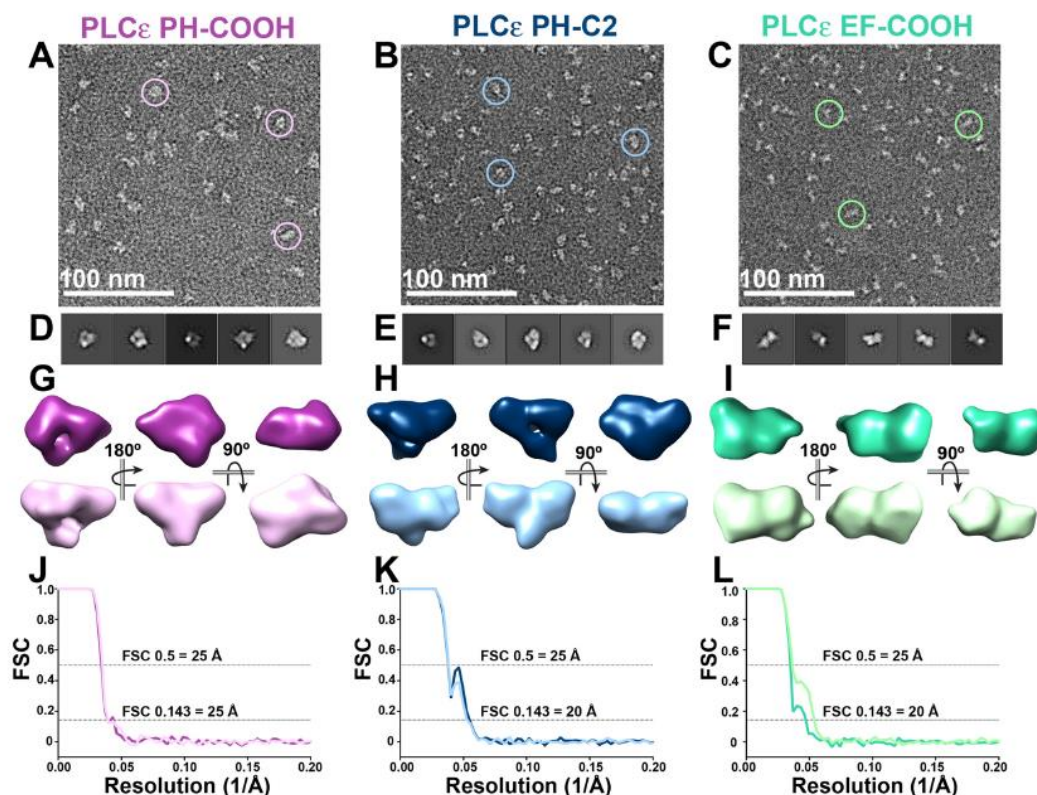


**Figure 3. Single-particle negative stain EM reconstructions confirm elongated conformations in PLCε variants.** A–C, raw, unadjusted micrograph field views with examples of picked particles (circles) for PLCε PH-COOH (A), PH-C2 (B), and EF-COOH (C). D–F, the top five reference-free 2D class averages for PH-COOH (D), PH-C2 (E), and EF-COOH (F) variants. G, two representative, refined 3D models of PH-COOH, with the top purple model generated from 9,879 particles and the bottom orchid model generated from 13,628 particles. H, representative models of PH-C2, with the top navy model generated from 24,129 particles and the bottom sky blue model generated from 22,343 particles. I, representative models of EF-COOH, with the top sea foam green model generated from 13,416 particles and the bottom lime green model generated from 14,498 particles. J–L, FSC curves for refined 3D models of PH-COOH, PH-C2, and EF-COOH, respectively. The gold-standard FSC (0.143) for all models indicates a final resolution of 25, 20, and 20 Å, respectively. FSC curves reflect the cross-correlation coefficient from aligning two independent half-maps. A representative workflow for the PLCε PH-COOH variant, containing A, D, and G, is shown in Fig. S5.

trends observed for the PH-COOH and PH-C2 variants, the reconstructions of EF-COOH are smaller overall than its SAXS envelopes. The EF-COOH reconstructions have molecular volumes of  $3.13 \times 10^5$  and  $3.67 \times 10^5 \text{ \AA}^3$  and maximum diameters of  $\sim 126$  and  $130 \text{ \AA}$  (Fig. 3, G–I) (45). Importantly, the EF-COOH reconstructions further confirm that this variant has a different molecular architecture compared with the PH-COOH and PH-C2 variants, due to deletion of the PH domain. This is consistent with the SAXS analysis of these variants (Fig. 2) and supports a model in which the PH domain adopts multiple conformations with respect to the rest of the PLC core.

#### The PLCβ3 PH domain is also conformationally dynamic

Because our data are consistent with the PH domain adopting multiple conformations in PLCε, we assessed the solution structure of the PLCβ3 core by performing SAXS on a variant that includes its PH, EF, TIM barrel, and C2 domains along with an autoinhibitory portion of its C-terminal domain (CTD), PLCβ3-Δ892 (Figs. 1A and 4).

We first compared the experimentally determined SAXS data for PLCβ3-Δ892 with the calculated SAXS data derived from the PLCβ3 crystal structure (containing the PH-proximal CTD domains from PDB entry 3OHM (12); Figs. 4 and 5, Tables 1 and 3, and Figs. S1–S3). The experimental and calculated Guinier plots for PLCβ3-Δ892 generated similar  $R_g$  values of 34 and 31 Å, with experimentally determined molecular masses of 87.9 kDa ( $V_c$ ) and 96.2 kDa ( $V_p$ ), comparable with the calculated molecular mass of 100.89 kDa. However, the Guinier plots for the two data sets have a  $\chi^2$  value of 7.8, indicating substantial divergence between the experimental and calculated data (Fig. 5B). The calculated pair distance distribution function for PLCβ3-Δ892 (Fig. 5C) is bell-shaped, as expected for the globular structure observed in crystal structures (Fig. 4A). However, the experimentally determined pair distance distribution function indicates the presence of extended features, as evidenced by the tail at high values of  $r$  (Fig. 5C). In addition, the calculated  $D_{\max}$  is 105 Å, compared with the experimentally determined

## Conformational dynamics of PLC enzymes

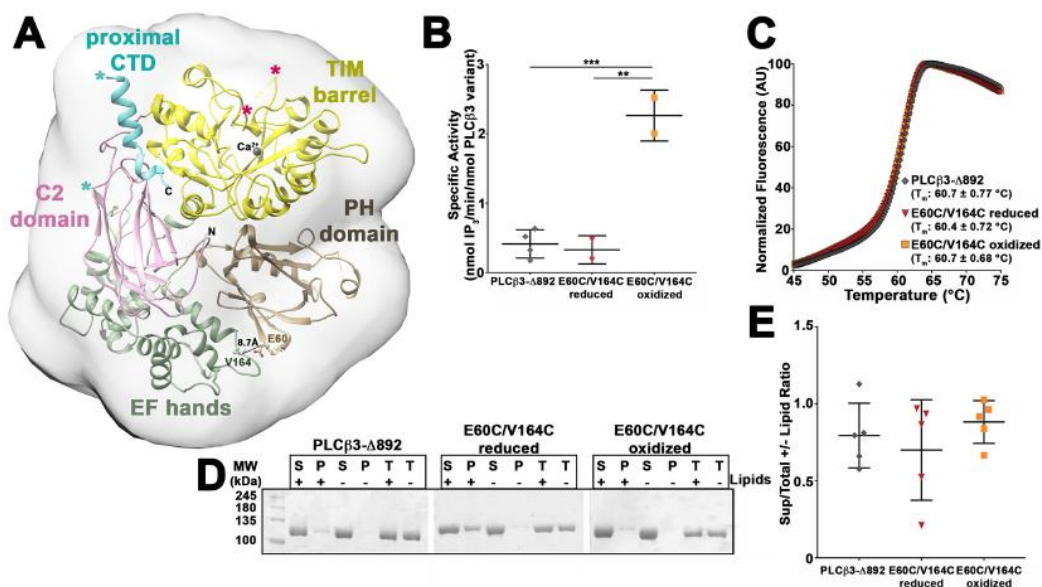


**Figure 4. Characterization of conformationally stabilized PLC $\beta$ 3- $\Delta$ 892 variants.** *A*, representative crystal structure of the PLC $\beta$ 3 core (PH-C2 domains) with the proximal CTD (PDB entry 3OHM (12)), with the domains labeled and colored as in Fig. 1A. The predicted SAXS envelope is shown as a gray 20-Å low-pass filter surrounding the crystal structure. Residues Glu-60 and Val-164 (shown in ball-and-stick representations) were mutated to cysteines for disulfide bond formation to restrict the motion of the PH domain. The X-Y linker and the loop connecting the C2 domain to the proximal CTD are disordered and omitted for clarity. The ends of the X-Y linker are denoted by hot pink asterisks, and the ends of the C2-proximal CTD are denoted by cyan asterisks (26). *B*, cysteine mutations in PLC $\beta$ 3- $\Delta$ 892 (E60C/V164C) alter basal specific activity only under oxidized conditions (\*\*\*,  $p \leq 0.001$ ; \*\*,  $p \leq 0.01$  based on one-way ANOVA followed by Tukey's multiple-comparison test). Basal specific activity data represents at least two experiments performed in duplicate  $\pm$  S.D. (error bars). *C*, cysteine mutations in PLC $\beta$ 3- $\Delta$ 892 (E60C/V164C) do not alter thermal stability under reducing or oxidizing conditions. Representative curves are shown for PLC $\beta$ 3- $\Delta$ 892 (gray diamonds), reduced E60C/V164C (red inverted triangles), and oxidized E60C/V164C (orange squares). Thermal stability data represent at least six experiments performed in triplicate  $\pm$  S.D. *D*, representative SDS-PAGE of PLC $\beta$ 3- $\Delta$ 892 variants following ultracentrifugation in the presence (+) or absence (-) of PE/PIP<sub>2</sub> liposomes. Total protein samples (T) contained protein incubated in the presence (+) or absence (-) of liposomes but were not subject to centrifugation. *E*, PLC $\beta$ 3- $\Delta$ 892 variants show minimal binding to liposomes. Gels were quantified as described in Fig. 1E, and no significant differences in liposome binding were observed for the PLC $\beta$ 3- $\Delta$ 892 variants. All data are mean  $\pm$  S.D. of at least four independent experiments and analyzed by one-way ANOVA followed by Tukey's multiple-comparison test.

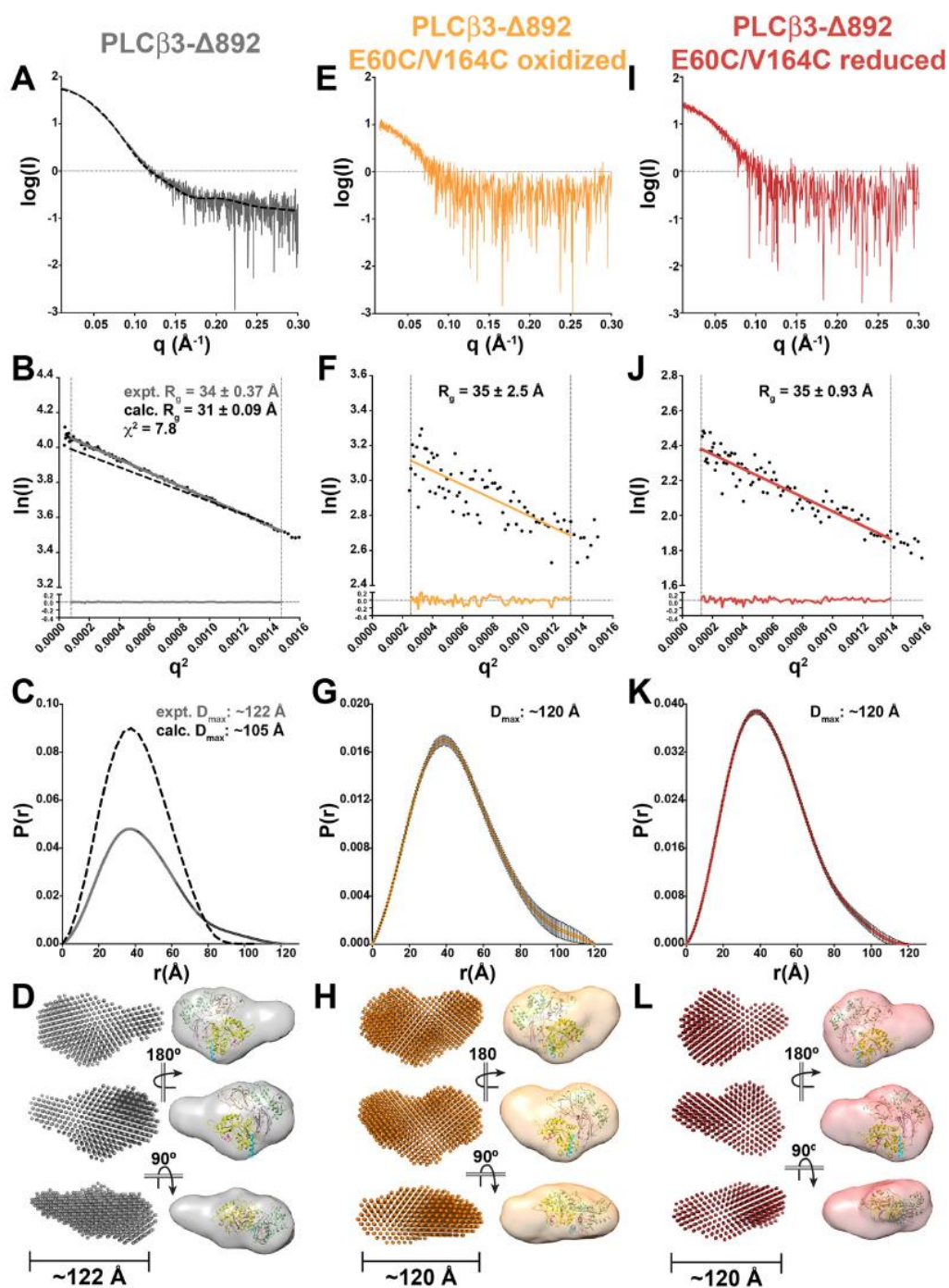
$D_{\max}$  of 122 Å. This is consistent with PLC $\beta$ 3- $\Delta$ 892 having a more extended structure in solution that is inconsistent with published crystal structures.

The volume of the *ab initio* envelope of PLC $\beta$ 3- $\Delta$ 892 encapsulates the crystal structure of PLC $\beta$ 3 but is more elongated and features a well-defined, extended protrusion (Fig. 5D). Thus, the overall shape of the PLC $\beta$ 3- $\Delta$ 892 SAXS envelope is more consistent with the SAXS envelopes and 3D reconstructions of PLC $\epsilon$  PH-COOH and PH-C2 than with the low-pass-filtered 20-Å envelope of the PLC $\beta$  3OHM crystal structure (Figs. 2, 3, and 4A). The compact portion of the PLC $\beta$ 3- $\Delta$ 892 SAXS envelope also shows additional density beyond the low-pass-filtered crystal structure (Fig. 5D). This most likely corresponds to disordered regions that are not observed in the crystal structure, such as the X-Y linker within the TIM barrel domain. In PLC $\beta$ 3, this linker is  $\sim$ 80 residues ( $\sim$ 9 kDa) and is disordered in all published structures (Fig. 4A).

To confirm that the extended protrusion observed in the experimentally determined PLC $\beta$ 3- $\Delta$ 892 envelope corresponds to the PH domain, we generated the E60C/V164C double mutant of PLC $\beta$ 3- $\Delta$ 892 (Fig. 4A). These two mutations, in combination with an exogenous bismaleimidoethane cross-linking reagent, were previously shown to restrict the motion of

the PH domain without impacting basal activity (26). Because the distance between the C $\beta$  atoms of these residues varies between crystal structures, we anticipated that they would be able to form a redox-dependent disulfide bond. Thus, we purified PLC $\beta$ 3- $\Delta$ 892 E60C/V164C under either oxidizing or reducing conditions. Using the [<sup>3</sup>H]PIP<sub>2</sub> hydrolysis activity assay, we found that reduced PLC $\beta$ 3- $\Delta$ 892 E60C/V164C had a specific activity of  $0.33 \pm 0.20$  nmol of IP<sub>3</sub>/min/nmol of PLC $\beta$ 3- $\Delta$ 892 variant, comparable with that of PLC $\beta$ 3- $\Delta$ 892 ( $0.41 \pm 0.20$  nmol of IP<sub>3</sub>/min/nmol of PLC $\beta$ 3- $\Delta$ 892 variant) (Fig. 4B). Oxidized PLC $\beta$ 3- $\Delta$ 892 E60C/V164C had a specific activity of  $2.3 \pm 0.37$  nmol of IP<sub>3</sub>/min/nmol of PLC $\beta$ 3- $\Delta$ 892 variant, significantly greater than that of PLC $\beta$ 3- $\Delta$ 892 ( $p \leq 0.001$ ) and reduced PLC $\beta$ 3- $\Delta$ 892 E60C/V164C ( $p \leq 0.01$ , Fig. 4B). However, all three PLC $\beta$ 3- $\Delta$ 892 variants had essentially identical  $T_m$  values as measured by DSF (Fig. 4C), and all variants bound similarly to PE/PIP<sub>2</sub> liposomes, as measured using the liposome pelleting assay (Fig. 4, D and E). The increased basal activity of oxidized PLC $\beta$ 3- $\Delta$ 892 E60C/V164C is in contrast to a recent report from Kadamur and Ross (26), who found no significant difference in basal activity when the PH domain was conformationally restricted by cross-linking. This difference is most likely due to the use of PLC $\beta$ 3- $\Delta$ 892 in this study as opposed to

## Conformational dynamics of PLC enzymes

Downloaded from <http://www.jbc.org/> at Purdue University Libraries on May 22, 2019

## Conformational dynamics of PLC enzymes

**Table 3**  
SAXS structural parameters of PLC $\beta$ 3- $\Delta$ 892 variants

	PLC $\beta$ 3- $\Delta$ 892	PLC $\beta$ 3- $\Delta$ 892 E60C/V164C (oxidized)	PLC $\beta$ 3- $\Delta$ 892 E60C/V164C (reduced)
<b>Guinier analysis</b>			
$I(0)$ ( $\text{cm}^{-1}$ )	59.44 $\pm$ 0.07	11.47 $\pm$ 0.34	25.33 $\pm$ 0.33
$R_g$ ( $\text{\AA}$ )	33.78 $\pm$ 0.37	35.13 $\pm$ 2.54	34.79 $\pm$ 0.93
$q$ min ( $\text{\AA}^{-1}$ )	0.0089	0.0159	0.0112
$q$ range ( $\text{\AA}^{-1}$ )	0.0089–0.0384	0.0159–0.0363	0.0112–0.0372
<b><math>P(r)</math> analysis</b>			
$I(0)$ ( $\text{cm}^{-1}$ )	59.76	11.36	25.28
$R_g$ ( $\text{\AA}$ )	34.43	35.81	35.12
$D_{\text{max}}$ ( $\text{\AA}$ )	122	120	120
Porod volume ( $\text{\AA}^{-3}$ )	165,000	166,000	164,000
$q$ range ( $\text{\AA}^{-1}$ )	0.0089–0.237	0.0159–0.227	0.0112–0.230

full-length PLC $\beta$ 3. Full-length PLC $\beta$ 3 retains the C-terminal extension and thus has increased membrane association and much higher basal activity (1, 7).

The oxidized and reduced PLC $\beta$ 3- $\Delta$ 892 E60C/V164C mutants were also analyzed by SAXS and were confirmed to be monomeric and monodisperse in solution (Fig. 5, Table 3, and Figs. S1–S4). Guinier plots of these variants generated  $R_g$  values of  $\sim$ 35  $\text{\AA}$  (Fig. 5, F and J). The experimentally determined molecular mass of oxidized PLC $\beta$ 3- $\Delta$ 892 E60C/V164C was found to be 71 kDa ( $V_c$ ) and 65.3 kDa ( $V_p$ ), and reduced PLC $\beta$ 3- $\Delta$ 892 E60C/V164C had molecular masses of 69 kDa ( $V_c$ ) and 53.3 kDa ( $V_p$ ), all of which are lower than the calculated molecular mass (100.6 kDa). The discrepancy in the SAXS-derived molecular masses versus the calculated molecular masses is likely due to the lower signal/noise ratio of these data sets. Thus, MALS was used to confirm the molecular masses of these variants in solution (Fig. S4). Finally, the pair distance distribution functions of these variants are similar, with  $D_{\text{max}}$  values of  $\sim$ 120  $\text{\AA}$  (Fig. 5, G and K). The *ab initio* envelopes of oxidized and reduced PLC $\beta$ 3- $\Delta$ 892 E60C/V164C were then compared with one another and PLC $\beta$ 3- $\Delta$ 892 (Fig. 5, D, H, and L). The oxidized PLC $\beta$ 3- $\Delta$ 892 E60C/V164C envelope has a more compact, globular structure as compared with the envelope of PLC $\beta$ 3- $\Delta$ 892 (Fig. 5, D and H). The molecular volume of the oxidized PLC $\beta$ 3- $\Delta$ 892 E60C/V164C envelope is  $3.42 \times 10^5 \text{\AA}^3$ , comparable with that of PLC $\beta$ 3- $\Delta$ 892 ( $3.44 \times 10^5 \text{\AA}^3$ ) (45). A similar result was obtained upon the addition of 15 mM excess bismaleimidoethane to PLC $\beta$ 3- $\Delta$ 892 E60C/V164C purified under reducing conditions. The resulting envelope again has a more compact shape than that of PLC $\beta$ 3- $\Delta$ 892, with a molecular volume of  $3.43 \times 10^5 \text{\AA}^3$  (Fig. S7 and Table S1). Thus, the disulfide bond between E60C and V164C limits the motion of PH domain similarly to the previously reported cross-linker (26). In contrast, the envelope for reduced PLC $\beta$ 3- $\Delta$ 892 E60C/

V164C is most similar to that of PLC $\beta$ 3- $\Delta$ 892, as it clearly features the extended protrusion (Fig. 5, D and L). It also shares a similar molecular volume as the other PLC $\beta$ 3- $\Delta$ 892 variants ( $3.49 \times 10^5 \text{\AA}^3$ ). Overall, these results are most consistent with the PLC $\beta$ 3 PH domain, likely together with EF1/2, adopting multiple conformations in solution that contribute to the final volume of the reconstruction.

## Discussion

PLC $\epsilon$  and PLC $\beta$  regulate the intracellular  $\text{Ca}^{2+}$  concentration and PKC activation downstream of GPCRs and, in the case of PLC $\epsilon$ , downstream of receptor tyrosine kinases (1, 10, 11). Numerous structures of PLC $\beta$  have been determined over the last 10 years (12–14, 18, 23, 24, 48), but the observed compactness of PLC $\beta$  in these structures appears to be misleading, given the growing evidence that its PH domain is conformationally dynamic (26–28), including in this study. Although PLC $\epsilon$  is anticipated to share a similar core architecture with PLC $\beta$  (46% sequence identity for the region including EF3-C2), it was not known whether its PH domain would be situated more similarly to crystal structures of PLC $\beta$  or PLC $\delta$  with respect to the core or how its C-terminal RA domains would influence the overall conformation of the protein.

Using biochemical assays, SAXS, and single-particle EM, we show that the PLC $\epsilon$  variants PH-COOH, PH-C2, and EF-COOH retain activity and have molecular architectures consisting of a compact core that features a well-defined protrusion (Figs. 1–3). As both PH-COOH and PH-C2 share this feature, this protrusion is highly unlikely to correspond to the RA domains and instead is most likely a core domain (Figs. 1–3) (9, 36). The loss of density on the opposite end of the SAXS envelope in PH-C2 relative to PH-COOH is consistent with deletion of the RA domains. However, fitting the structure of the PLC $\beta$ 3 core (PDB entry 3OHM (12)) in the PH-COOH and PH-C2 envelopes such that the C terminus of the C2 domain extends into the additional density also fails to account for the volume of the observed envelopes. Whereas PLC $\epsilon$  PH-C2 is  $\sim$ 35 kDa larger than PLC $\beta$ 3 PH-C2, this is largely due to insertions and a longer X-Y linker and is still insufficient to account for the total volume of the envelope, especially the extended protrusion. Thus, the large envelopes are most consistent with dynamic behavior at the N terminus of the PLC $\epsilon$  variants. This observation is consistent with the fact that deletion of the PH domain has no effect on thermal stability (Fig. 1C), indicating that interactions between this domain and the rest of the core are transient in nature. We propose that the PH domain in both PLC $\beta$ 3 and PLC $\epsilon$  is connected to the rest of the core via the

**Figure 5. PLC $\beta$ 3- $\Delta$ 892 SAXS analysis confirms conformational dynamics of its PH domain.** A and B, raw scattering curve (A) and Guinier analyses (B) of low  $q$  values,  $\ln(I)$  (beam intensity) versus  $q^2$  (scattering angle) with  $R_g$  for PLC $\beta$ 3- $\Delta$ 892 (gray line) and calculated from the PLC $\beta$ 3 crystal structure (dashed black line, PDB code 3OHM (12)). Fitting of the experimental linear regression to the experimental data is represented by residuals, as shown in the bottom tenth of the plot, and confirms that the proteins are monomeric in solution. C, pair distance distribution function  $P(r)$ , with maximum interparticle distance ( $D_{\text{max}}$ ) for the experimentally determined and calculated PLC $\beta$ 3- $\Delta$ 892 data shown as in B. D, *ab initio* “dummy atom” envelope models (left) and equivalent envelope rendered as volumes (right) for PLC $\beta$ 3- $\Delta$ 892. The PLC $\beta$ 3 crystal structure is fitted as a reference, with the PH domain oriented toward the extended protrusion and colored as in Fig. 1A. E–G, raw scattering curve (E), Guinier analysis (F), and pair distance distribution function (G) of oxidized PLC $\beta$ 3- $\Delta$ 892 E60C/V164C. H, *ab initio* “dummy atom” envelope models (left) and equivalent envelope rendered as volumes (right) of oxidized PLC $\beta$ 3- $\Delta$ 892 E60C/V164C, with the crystal structure fit as in D. I–K, raw scattering curve (I), Guinier analysis (J), and pair distance distribution function (K) of reduced PLC $\beta$ 3- $\Delta$ 892 E60C/V164C. L, *ab initio* “dummy atom” envelope models (left) and equivalent envelope rendered as volume (right) for reduced PLC $\beta$ 3- $\Delta$ 892 E60C/V164C, with the crystal structure fit as in D. PLC $\beta$ 3- $\Delta$ 892 and reduced PLC $\beta$ 3- $\Delta$ 892 E60C/V164C envelopes show similar protrusions, whereas oxidized PLC $\beta$ 3- $\Delta$ 892 E60C/V164C appears more compact.

## Conformational dynamics of PLC enzymes

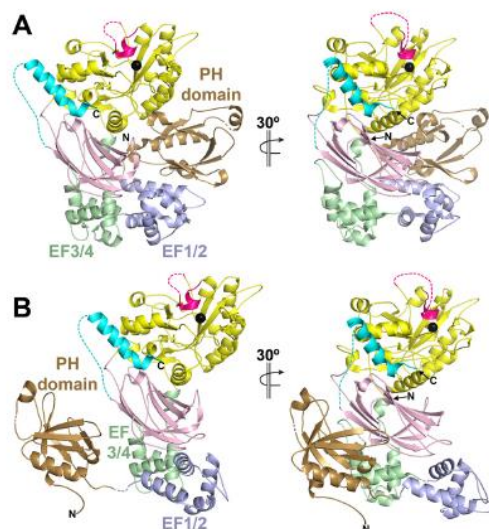


**Figure 6. A rigid-body ensemble model of PLC $\beta$ 3- $\Delta$ 892 is consistent with conformational heterogeneity of the PH domain and EF1/2.** *A*, crystal structures of the PLC $\beta$  subfamily reveal a compact structure, wherein the PH domain is in close proximity to the TIM barrel domain and EF-hands 1 and 2 (EF1/2). Domains are colored as in Fig. 1A, with the exception of EF1/2, which are shown in *periwinkle blue*. Dashed lines, regions disordered in the crystal structure, with the catalytic Ca<sup>2+</sup> ion shown as a *black sphere*. *B*, a rigid-body ensemble model that better fits the experimentally determined SAXS data was determined using SASREF ( $\chi^2$  of 1.67 (61)). In this model, the PH domain (residues 11–146), EF1/2 (residues 147–221), and the remaining domains of PLC $\beta$ 3- $\Delta$ 892 (residues 222–892) were treated as independent, rigid bodies. Additional restraints included restricting the PH domain C terminus to within 5 Å of the N terminus of EF1/2 and the C terminus of EF1/2 within 5 Å of the N terminus of EF3 and the rest of the enzyme. In the resulting model, the PH domain is translated by  $\sim 140^\circ$  and translated  $\sim 70$  Å from its position in the crystal structure. This large motion is facilitated by EF1/2, which is rotated by  $\sim 155^\circ$  and translated  $\sim 20$  Å from its position in the crystal structure. EF1/2 hands are weakly conserved compared with the rest of core domains across PLC enzymes and variably ordered in crystal structures of PLC $\beta$ . Finally, the residues linking EF2 and EF3 may serve as a hinge region, facilitating the rotation of EF1/2 and allowing the PH domain to sample multiple conformations.

weakly conserved EF1/2 hands and that a hinge between EF2 and EF3 allows the PH domain to adopt multiple conformations with respect to the core. In support of this hypothesis, we used ensemble rigid-body modeling to generate a model based on PLC $\beta$ 3- $\Delta$ 892 SAXS data (Figs. 5 and 6). In the resulting computational model, which fits the experimental data with a  $\chi^2$  of 1.67, the PH domain and EF1/2 are rotated away from the rest of the PLC core and from one another. The PH domain is rotated  $\sim 140^\circ$  from its position in the crystal structures and translated by  $\sim 70$  Å. EF1/2 is also rotated from its position in the crystal structure by  $\sim 155^\circ$  and translated by  $\sim 20$  Å (Fig. 6). This flexibility would therefore allow the PH domain and EF1/2 to adopt multiple conformational changes with respect to one another and to the rest of the PLC core. Although the current model is limited by the resolution of the SAXS envelopes and the EM reconstructions, it represents the simplest model of the data.

We also showed that the PLC $\epsilon$  PH domain is important for lipase activity (Fig. 1B). The C-terminal RA domains of PLC $\epsilon$  also make a substantial contribution to basal activity (Fig. 1B),

but because these domains contribute to stability as measured by DSF (Fig. 1C), the loss of activity is most simply explained by decreased structural integrity of the core. As the RA2 domain is the primary binding site for activators such as Rap1A and Ras (20, 21), this may provide a potential mechanism by which small GTPases could allosterically activate phosphatidylinositol hydrolysis. In future studies, the role of the N-terminal CDC25 domain will need to be similarly assessed.

Although the PLC $\beta$ 3 core is compact in crystal structures (Fig. 4) (12, 24), its SAXS envelope features a similar extended protrusion observed in the PLC $\epsilon$  PH-COOH and PH-C2 envelopes (Figs. 2, 3, and 5). To determine whether this extended protrusion is in fact the PH domain, we used SAXS to study the PLC $\beta$ 3- $\Delta$ 892 E60C/V164C variant under reducing and oxidizing conditions, which would restrain the motion of the PH domain (Fig. 5) (26). The molecular envelope of the reduced PLC $\beta$ 3- $\Delta$ 892 E60C/V164C mutant is most similar to that of PLC $\beta$ 3- $\Delta$ 892, whereas oxidation or cross-linking results in a more compact molecular envelope lacking a defined extended protrusion (Fig. 5 and Fig. S7). The more compact structures observed following oxidation or cross-linking are more consistent with the conformation of PLC $\beta$ 3 in crystal structures. Thus, we believe that these studies are the first to provide direct structural evidence for multiple conformations of the PLC $\beta$  PH domain and possibly EF1/2. However, the respective contributions of these conformational states to basal activity and membrane association require further study (26).

Extension of the PH domain from the catalytic core may be important for PLC $\beta$  and PLC $\epsilon$  regulation by G $\beta$  $\gamma$  subunits (8, 9, 49, 50). Despite multiple studies over several decades, the G $\beta$  $\gamma$ -binding site on PLC $\beta$  has remained elusive (27, 28, 51, 52). Previous studies have suggested that G $\beta$  $\gamma$ -dependent regulation of PLC $\beta$  is modulated by interactions between these two proteins and the membrane (28, 53). It is therefore possible that the PH domain is extended when PLC $\beta$  is in contact with membranes. Interdomain contacts between the PH domain and the other core domains, including their respective orientation at the membrane, may also contribute to regulation (28). More recently, the G $\beta$  $\gamma$ -binding site in PLC $\beta$  was proposed to be blocked in the closed conformation of the PH domain, suggesting that conformational flexibility of the domain is required for G $\beta$  $\gamma$  binding and activation (26). Our data are fully consistent with this model. The mechanism of G $\beta$  $\gamma$ -dependent activation of PLC $\epsilon$  is only beginning to be investigated (9), but because our data are consistent with PLC $\epsilon$  also containing a conformationally dynamic PH domain, we propose that it may likewise contribute to G $\beta$  $\gamma$ -dependent regulation.

### Experimental procedures

#### PLC $\epsilon$ and PLC $\beta$ expression and purification

cDNA encoding *Rattus norvegicus* PLC $\epsilon$  PH-COOH (residues 837–2282), PH-C2 (residues 832–1972), and EF-COOH (residues 1035–2282) were subcloned into the pFastBac-HTA vector (Invitrogen) and confirmed by sequencing over the entire coding region. Proteins were expressed in baculovirus-infected Sf9 cells, harvested 48–72 h postinfection, and flash-frozen. PLC $\beta$ 3- $\Delta$ 892 (residues 10–892) was expressed as

## Conformational dynamics of PLC enzymes

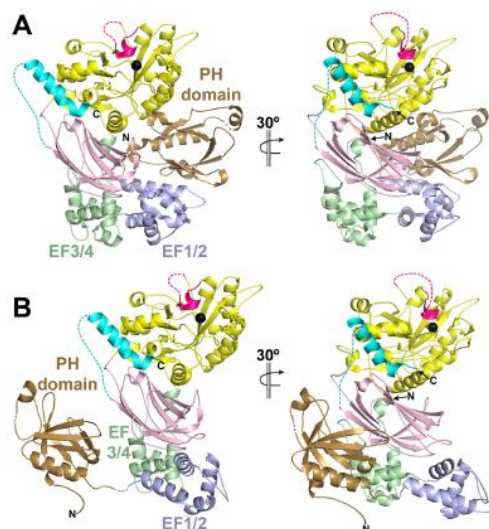


**Figure 6. A rigid-body ensemble model of PLC $\beta$ 3- $\Delta$ 892 is consistent with conformational heterogeneity of the PH domain and EF1/2.** *A*, crystal structures of the PLC $\beta$  subfamily reveal a compact structure, wherein the PH domain is in close proximity to the TIM barrel domain and EF-hands 1 and 2 (EF1/2). Domains are colored as in Fig. 1A, with the exception of EF1/2, which are shown in *periwinkle blue*. Dashed lines, regions disordered in the crystal structure, with the catalytic Ca<sup>2+</sup> ion shown as a *black sphere*. *B*, a rigid-body ensemble model that better fits the experimentally determined SAXS data was determined using SASREF ( $\chi^2$  of 1.67 (61)). In this model, the PH domain (residues 11–146), EF1/2 (residues 147–221), and the remaining domains of PLC $\beta$ 3- $\Delta$ 892 (residues 222–892) were treated as independent, rigid bodies. Additional restraints included restricting the PH domain C terminus to within 5 Å of the N terminus of EF1/2 and the C terminus of EF1/2 within 5 Å of the N terminus of EF3 and the rest of the enzyme. In the resulting model, the PH domain is translated by  $\sim$ 140° and translated  $\sim$ 70 Å from its position in the crystal structure. This large motion is facilitated by EF1/2, which is rotated by  $\sim$ 155° and translated  $\sim$ 20 Å from its position in the crystal structure. EF1/2 hands are weakly conserved compared with the rest of core domains across PLC enzymes and variably ordered in crystal structures of PLC $\beta$ . Finally, the residues linking EF2 and EF3 may serve as a hinge region, facilitating the rotation of EF1/2 and allowing the PH domain to sample multiple conformations.

weakly conserved EF1/2 hands and that a hinge between EF2 and EF3 allows the PH domain to adopt multiple conformations with respect to the core. In support of this hypothesis, we used ensemble rigid-body modeling to generate a model based on PLC $\beta$ 3- $\Delta$ 892 SAXS data (Figs. 5 and 6). In the resulting computational model, which fits the experimental data with a  $\chi^2$  of 1.67, the PH domain and EF1/2 are rotated away from the rest of the PLC core and from one another. The PH domain is rotated  $\sim$ 140° from its position in the crystal structures and translated by  $\sim$ 70 Å. EF1/2 is also rotated from its position in the crystal structure by  $\sim$ 155° and translated by  $\sim$ 20 Å (Fig. 6). This flexibility would therefore allow the PH domain and EF1/2 to adopt multiple conformational changes with respect to one another and to the rest of the PLC core. Although the current model is limited by the resolution of the SAXS envelopes and the EM reconstructions, it represents the simplest model of the data.

We also showed that the PLC $\epsilon$  PH domain is important for lipase activity (Fig. 1B). The C-terminal RA domains of PLC $\epsilon$  also make a substantial contribution to basal activity (Fig. 1B),

but because these domains contribute to stability as measured by DSF (Fig. 1C), the loss of activity is most simply explained by decreased structural integrity of the core. As the RA2 domain is the primary binding site for activators such as Rap1A and Ras (20, 21), this may provide a potential mechanism by which small GTPases could allosterically activate phosphatidylinositol hydrolysis. In future studies, the role of the N-terminal CDC25 domain will need to be similarly assessed.

Although the PLC $\beta$ 3 core is compact in crystal structures (Fig. 4) (12, 24), its SAXS envelope features a similar extended protrusion observed in the PLC $\epsilon$  PH-COOH and PH-C2 envelopes (Figs. 2, 3, and 5). To determine whether this extended protrusion is in fact the PH domain, we used SAXS to study the PLC $\beta$ 3- $\Delta$ 892 E60C/V164C variant under reducing and oxidizing conditions, which would restrain the motion of the PH domain (Fig. 5) (26). The molecular envelope of the reduced PLC $\beta$ 3- $\Delta$ 892 E60C/V164C mutant is most similar to that of PLC $\beta$ 3- $\Delta$ 892, whereas oxidation or cross-linking results in a more compact molecular envelope lacking a defined extended protrusion (Fig. 5 and Fig. S7). The more compact structures observed following oxidation or cross-linking are more consistent with the conformation of PLC $\beta$ 3 in crystal structures. Thus, we believe that these studies are the first to provide direct structural evidence for multiple conformations of the PLC $\beta$  PH domain and possibly EF1/2. However, the respective contributions of these conformational states to basal activity and membrane association require further study (26).

Extension of the PH domain from the catalytic core may be important for PLC $\beta$  and PLC $\epsilon$  regulation by G $\beta$  $\gamma$  subunits (8, 9, 49, 50). Despite multiple studies over several decades, the G $\beta$  $\gamma$ -binding site on PLC $\beta$  has remained elusive (27, 28, 51, 52). Previous studies have suggested that G $\beta$  $\gamma$ -dependent regulation of PLC $\beta$  is modulated by interactions between these two proteins and the membrane (28, 53). It is therefore possible that the PH domain is extended when PLC $\beta$  is in contact with membranes. Interdomain contacts between the PH domain and the other core domains, including their respective orientation at the membrane, may also contribute to regulation (28). More recently, the G $\beta$  $\gamma$ -binding site in PLC $\beta$  was proposed to be blocked in the closed conformation of the PH domain, suggesting that conformational flexibility of the domain is required for G $\beta$  $\gamma$  binding and activation (26). Our data are fully consistent with this model. The mechanism of G $\beta$  $\gamma$ -dependent activation of PLC $\epsilon$  is only beginning to be investigated (9), but because our data are consistent with PLC $\epsilon$  also containing a conformationally dynamic PH domain, we propose that it may likewise contribute to G $\beta$  $\gamma$ -dependent regulation.

## Experimental procedures

### PLC $\epsilon$ and PLC $\beta$ expression and purification

cDNA encoding *Rattus norvegicus* PLC $\epsilon$  PH-COOH (residues 837–2282), PH-C2 (residues 832–1972), and EF-COOH (residues 1035–2282) were subcloned into the pFastBac-HTA vector (Invitrogen) and confirmed by sequencing over the entire coding region. Proteins were expressed in baculovirus-infected Sf9 cells, harvested 48–72 h postinfection, and flash-frozen. PLC $\beta$ 3- $\Delta$ 892 (residues 10–892) was expressed as

## Conformational dynamics of PLC enzymes

described previously (14). PLC $\beta$ 3- $\Delta$ 892 E60C/V164C was generated using site-directed mutagenesis, confirmed by sequencing over the entire coding region, and expressed as described (14).

PLC $\epsilon$  variants were purified as described (9), with some modifications for proteins used in single-particle EM and liposome-pelleting assays. After lysis and ultracentrifugation, the supernatant was applied to a 5-ml HisTrap FF column (GE Healthcare) equilibrated with Buffer A (20 mM HEPES, pH 8, 300 or 500 mM NaCl, 20 mM imidazole, 10 mM  $\beta$ -mercaptoethanol, 0.1 mM EDTA, and 0.1 mM EGTA) and eluted with a gradient of 0–100% Buffer A supplemented with 500 mM imidazole pH 8. Fractions containing protein were pooled, buffer-exchanged with an equal volume of Buffer E (20 mM HEPES, pH 8, 50 mM NaCl, 2 mM DTT, 0.1 mM EDTA, and 0.1 mM EGTA), and loaded onto a 1-ml MonoQ 5/50 GL column (GE Healthcare) pre-equilibrated with Buffer E. Protein was eluted with a gradient of 0–100% MonoQ-S Buffer E containing 500 mM NaCl. Fractions containing protein were again pooled, buffer-exchanged, and concentrated as described above before loading on a 1-ml MonoS 5/50 GL column (GE Healthcare) pre-equilibrated with Buffer E. The protein was eluted, pooled, and concentrated as described above before final purification over tandem Superdex 200 Increase columns (GE Healthcare).

PLC $\beta$ 3- $\Delta$ 892 and reduced PLC $\beta$ 3- $\Delta$ 892 E60C/V164C were purified as described previously (54). Oxidized PLC $\beta$ 3- $\Delta$ 892 E60C/V164C was purified similarly, but reducing agents were omitted in each step.

### Differential scanning fluorimetry

DSF assays were carried out as described previously (40, 54), with minor modifications. Purified PLC $\epsilon$  (0.2–0.6 mg/ml) and PLC $\beta$  variants (0.5 mg/ml) were incubated with 5 $\times$  SYPRO orange dye in the presence of 5 mM CaCl<sub>2</sub>. All assays were performed in duplicate or triplicate with protein from at least two independent purifications.

### Basal activity assays

PLC $\epsilon$  and PLC $\beta$  activity was measured as described previously (24, 38, 54). The PLC $\epsilon$  PH-COOH variant was assayed at a final concentration of 0.075 ng/ $\mu$ l, PH-C2 at 0.1–1 ng/ $\mu$ l, and EF-COOH at 0.5 ng/ $\mu$ l. PLC $\beta$ 3- $\Delta$ 892 was assayed at a final concentration of 10 ng/ $\mu$ l, and PLC $\beta$ 3- $\Delta$ 892 E60C/V164C (oxidized or reduced) was assayed at 12 ng/ $\mu$ l. Oxidized PLC $\beta$ 3- $\Delta$ 892 E60C/V164C was assayed in the absence of reducing agents. All assays were performed at least in duplicate with protein from at least two independent purifications.

### SEC-SAXS/MALS-DLS data collection and analysis

SEC-SAXS was performed at BioCAT (Sector 18) Advanced Photon Source equipped with an ÅKTA Pure FPLC and a Pilatus3 1M detector (Dectris) with a beam size of 160  $\mu$ m  $\times$  75  $\mu$ m (Table 1). Data were collected at room temperature, with a 12-KeV X-ray (1.033-Å wavelength) and  $\sim$ 3.5-m sample-to-detector distance ( $q$  range = 0.00365 to 0.383 Å<sup>-1</sup>). All purified PLC $\epsilon$  and PLC $\beta$ 3- $\Delta$ 892 variants were diluted to a final concentration of 2–3 mg/ml in 20 mM HEPES, pH 8, 200 mM NaCl, 2 mM DTT, 0.1 mM EDTA, and 0.1 mM EGTA. Samples were

centrifuged at 16,000  $\times g$  for 5 min at 4 °C before data collection. Protein samples were eluted on a Superdex 200 Increase column (GE Healthcare; Figs. S1 and S2). The eluate was passed through the UV monitor and then the SAXS flow cell, which consists of a 1.5-mm quartz capillary with 10- $\mu$ m walls. Data were collected every 2 s with 1-s exposure times. For PLC $\epsilon$  PH-COOH, frames corresponding to the leading edge of the elution peak as opposed to the highest point of the peak were selected for SAXS analysis. The usual practice of averaging frames corresponding to the highest point in the peak manifested symptoms of aggregation in the Guinier analysis due to possible capillary fouling (Fig. S1A). For all other PLC $\epsilon$  and all PLC $\beta$ 3- $\Delta$ 892 variants, frames corresponding to the protein peak were used for SAXS analysis (Fig. S1, B–F). A buffer file was generated for all samples by averaging exposures flanking the elution peak and was used for background subtraction (Fig. S1).

Raw scattering data were reduced using BioXTAS RAW 1.4.0 (55) and ATSAS (56). The low variability in the distribution of  $R_g$  corresponding to the individual frames as seen plotted with the “scattering chromatograms” (integrated intensity of individual exposures plotted against frame number) demonstrates the monodisperse nature of the samples (Fig. S3). For oxidized PLC $\beta$ 3- $\Delta$ 892 E60C/V164C, automated Guinier approximation for individual frames was not possible due to low signal to noise, and we therefore used averaged frames 188–193 to enable reliable Guinier approximation and calculation of the  $R_g$ . We used MALS data and the molecular mass distribution across the elution peak to confirm the monodisperse nature of PLC $\epsilon$  PH-COOH, oxidized PLC $\beta$ 3- $\Delta$ 892 E60C/V164C, and reduced PLC $\beta$ 3- $\Delta$ 892 E60C/V164C (Fig. S4). For the SEC-MALS-DLS (dynamic light scattering) experiments, the samples were loaded on the SEC column with an exclusion limit of 1.25 MDa (WTC-030S5, Wyatt Technologies), which was followed by a UV detector, a MALS detector, and a DLS detector (DAWN Helios II, Wyatt Technologies). This experiment enabled us to not only establish that the samples were monodisperse but also to acquire a more reliable estimate for the molecular mass of samples analyzed using the ASTRA software (Wyatt Technologies) that were ambiguous with SAXS.  $I(q)$  versus  $q$  curves generated after buffer subtraction and averaging selected exposures were used for more detailed analyses of the SAXS data.  $R_g$ ,  $I(0)$ , and  $D_{\max}$  for each protein were obtained using PRIMUS (57). 10–15 *ab initio* models were calculated using DAMMIF, and then aligned and averaged with DAMAVER (58). For all PLC $\epsilon$  and PLC $\beta$ 3- $\Delta$ 892 variants, the mean NSD for all calculated models ranged from 0.560  $\pm$  0.018 to 0.968  $\pm$  0.032. One *ab initio* model was excluded from both the PLC $\epsilon$  EF-COOH and oxidized PLC $\beta$ 3- $\Delta$ 892 E60C/V164C data sets (discard criteria NSD > mean + 2  $\times$  S.D.). Final *ab initio* envelope structures were generated using DAMMIN (59). Plots were generated from buffer-subtracted averaged data (raw scattering and Guinier plots) or pair distance distribution ( $P(r)$  plots) and plotted using GraphPad Prism version 7.0.

Theoretical SAXS data for the PLC $\beta$ 3 core crystal structure was generated using its coordinate file (PDB entry 3OHM (12)). CRY SOL3.0 (56, 60) was used to compare the calculated SAXS data with the experimentally determined data for PLC $\beta$ 3- $\Delta$ 892.

## Conformational dynamics of PLC enzymes

SASREF (61) was used to generate a computational model that fit the empirical SAXS data. For this model, the following inter-domain distance restraints were placed. The C terminus of the PH domain (residues 10–146) was within 5 Å of the N terminus of the EF1/2 hands (residues 147–221), and the C terminus of the EF1/2 hands was within 5 Å of EF3-proximal CTD (residues 222–892). The theoretical SAXS scattering curve was then compared with the empirically determined data. Plots were generated from buffer-subtracted averaged data (raw scattering and Guinier plots) or averaged envelope data ( $P(r)$  plots) and plotted using GraphPad Prism version 7.0.

### Negative stain EM sample preparation and imaging

For each PLC $\epsilon$  variant, 3  $\mu$ l of freshly purified protein (0.015–0.018 mg/ml) was applied to glow-discharged carbon-coated 400-mesh copper grids (Electron Microscopy Sciences) and stained with 0.75% uranyl formate (47). Samples were imaged with a CM200 field electron gun transmission electron microscope (Phillips) operated at 200 kV. Micrographs were collected with a US4000 4k  $\times$  4k CCD camera (Gatan), using a 1-s exposure time, defocus range of 5  $\mu$ m, and at a nominal magnification of 50,000 $\times$ , resulting in a sampling of 2.31 Å/pixel at the specimen level.

### Single-particle 3D EM reconstructions

Data were processed with a beta release of RELION 2.1 (62). Raw micrographs were CTF-corrected, and particles were autopicked before reference-free 2D class averaging. For PLC $\epsilon$  PH-COOH, 47,300 particles were extracted, and the 2D classes contained 34,155 particles. For PLC $\epsilon$  PH-C2, 124,747 particles were extracted, and the 2D classes contained 91,982 particles. For PLC $\epsilon$  EF-COOH, 58,549 particles were extracted, and the 2D classes contained 53,028 particles. To minimize any potential model bias, *de novo* initial models were generated for PH-COOH, PH-C2, and EF-COOH from their respective 2D class averages. From the respective selected 2D classes for each variant, we generated two particle subsets containing  $\sim$ 100 particles per 2D class to build *de novo* initial models with the RELION-2.1b1 stochastic gradient descent method. One initial model per subset was chosen at random and used as a reference for 3D class averaging of particles from the best 2D classes. Four 3D classes were generated per initial model. When possible, the dominant 3D class from each of the two sets of four 3D classes was chosen for 3D auto-refinement, resulting in two final, refined structures. The representative workflow is shown in Fig. S5. Fourier shell correlation (FSC) curves corresponding to refined models were calculated using standard methods (63).

### Liposome pelleting assays

200  $\mu$ M hen egg white phosphatidylethanolamine and 100  $\mu$ M porcine brain phosphatidylinositol 4,5-bisphosphate (Avanti Polar Lipids) were mixed and dried under  $N_2$ . Lipids were resuspended in sonication buffer (50 mM HEPES, pH 7, 80 mM KCl, 3 mM EGTA, and 2 mM DTT) and sonicated in two 30-s bursts (14, 38). For oxidized PLC $\beta$ 3- $\Delta$ 892 E60C/V164C, DTT was omitted from the sonication buffer. Liposomes (65  $\mu$ l) were combined with either 2  $\mu$ g of total PLC $\epsilon$  variant (0.15 nmol of PLC $\epsilon$  PH-COOH, 0.19 nmol of PLC $\epsilon$  PH-C2, 0.17 nmol

of PLC $\epsilon$  EF-COOH) or 1  $\mu$ g of total PLC $\beta$ 3- $\Delta$ 892 variant (0.125 nmol) and sonication buffer to a final volume of 100  $\mu$ l. Control binding reactions contained protein and buffer only, and total protein controls were incubated with liposomes or buffer. All samples were incubated for 1 h on ice. All samples, excluding total protein control samples, were then centrifuged at 119,000  $\times$  g for 1 h. Total protein control samples were incubated on ice for the duration of the ultracentrifugation. For centrifuged samples, the supernatant was removed, and the pellet was resuspended in 100  $\mu$ l of sonication buffer. The PLC $\epsilon$  pellets were also subjected to sonication to resuspend the pellet. For analysis by SDS-PAGE and ImageJ, 16  $\mu$ l of the supernatant, resuspended pellet, or total protein control was denatured with 4  $\mu$ l of 5 $\times$  SDS loading dye, and 5  $\mu$ l of the total sample was analyzed by SDS-PAGE. All gels were stained with Bio-Safe Coomassie Blue (Bio-Rad), and band density was quantified with ImageJ.

### Statistical methods

All plots were generated using GraphPad Prism version 7.0. One-way ANOVA was performed with Prism 7.0 and followed by Tukey post hoc multiple comparisons as noted in the figure legends. All error bars represent S.D.

### Figure creation

Single-particle EM 3D envelopes were rendered with UCSF Chimera (45). SAXS molecular envelopes were generated from dummy atom coordinate files with *e2pdb2mrc.py* (64) using a low-pass filter to 20 Å and rendered in Chimera. All ribbon diagrams and dummy atom models were generated using PyMOL (Schrodinger, LLC, New York). Figures were created using Adobe Illustrator and Photoshop.

**Author contributions**—A. M. L. designed the overall experimental approach. E. E. G.-K., M. S., M. V. C., and C. C. cloned, expressed, and purified all PLC $\beta$  and PLC $\epsilon$  proteins. S. C., E. E. G.-K., M. V. C., and M. S. carried out all SAXS experiments, and E. E. G.-K., M. V. C., and M. S. performed DSF and activity assays. E. E. G.-K., M. V. C., and A. B. carried out liposome pelleting assays. E. E. G.-K., F. S. V., W. J., and A. M. L. designed and carried out all electron microscopy studies. A. M. L., E. E. G.-K., F. S. V., M. S., and M. V. C. wrote the manuscript.

**Acknowledgments**—We thank A. V. Smrcka (University of Michigan) for the *R. norvegicus* PLC $\epsilon$  cDNA and technical and editorial advice. We thank J. Tesmer (Purdue University) and M. Tantama (Purdue University) for helpful discussions. This research used resources of the Advanced Photon Source, a United States Department of Energy (DOE) Office of Science User Facility operated for the DOE Office of Science by Argonne National Laboratory under Contract DE-AC02-06CH11357. This project was supported by NIGMS, National Institutes of Health (NIH), Grant 9 P41 GM103622. Use of the Pilatus 3 1M detector was provided by NIGMS, NIH, Grant 1S10OD018090-01.

### References

1. Kadamur, G., and Ross, E. M. (2013) Mammalian phospholipase C. *Annu. Rev. Physiol.* 75, 127–154 [CrossRef Medline](#)

## Conformational dynamics of PLC enzymes

2. Filtz, T. M., Grubb, D. R., McLeod-Dryden, T. J., Luo, J., and Woodcock, E. A. (2009)  $G_q$ -initiated cardiomyocyte hypertrophy is mediated by phospholipase  $C\beta 1$ . *FASEB J.* **23**, 3564–3570 [CrossRef Medline](#)
3. Grubb, D. R., Crook, B., Ma, Y., Luo, J., Qian, H. W., Gao, X. M., Kiriazis, H., Du, X. J., Gregorevic, P., and Woodcock, E. A. (2015) The atypical 'b' splice variant of phospholipase  $C\beta 1$  promotes cardiac contractile dysfunction. *J. Mol. Cell Cardiol.* **84**, 95–103 [CrossRef Medline](#)
4. Zhang, L., Malik, S., Kelley, G. G., Kapiloff, M. S., and Smrcka, A. V. (2011) Phospholipase  $C\epsilon$  scaffolds to muscle-specific A kinase anchoring protein (mAKAP $\beta$ ) and integrates multiple hypertrophic stimuli in cardiac myocytes. *J. Biol. Chem.* **286**, 23012–23021 [CrossRef Medline](#)
5. Zhang, L., Malik, S., Pang, J., Wang, H., Park, K. M., Yule, D. I., Blaxall, B. C., and Smrcka, A. V. (2013) Phospholipase  $C\epsilon$  hydrolyzes perinuclear phosphatidylinositol 4-phosphate to regulate cardiac hypertrophy. *Cell* **153**, 216–227 [CrossRef Medline](#)
6. Smrcka, A. V. (2015) Regulation of phosphatidylinositol-specific phospholipase C at the nuclear envelope in cardiac myocytes. *J. Cardiovasc. Pharmacol.* **65**, 203–210 [CrossRef Medline](#)
7. Lyon, A. M., and Tesmer, J. J. (2013) Structural insights into phospholipase  $C-\beta$  function. *Mol. Pharmacol.* **84**, 488–500 [CrossRef Medline](#)
8. Wing, M. R., Houston, D., Kelley, G. G., Der, C. J., Siderovski, D. P., and Harden, T. K. (2001) Activation of phospholipase  $C-\epsilon$  by heterotrimeric G protein  $\beta\gamma$ -subunits. *J. Biol. Chem.* **276**, 48257–48261 [CrossRef Medline](#)
9. Madukwe, J. C., Garland-Kuntz, E. E., Lyon, A. M., and Smrcka, A. V. (2018) G protein  $\beta\gamma$  subunits directly interact with and activate phospholipase  $C\epsilon$ . *J. Biol. Chem.* **293**, 6387–6397 [CrossRef Medline](#)
10. Smrcka, A. V., Brown, J. H., and Holz, G. G. (2012) Role of phospholipase  $C\epsilon$  in physiological phosphoinositide signaling networks. *Cell. Signal.* **24**, 1333–1343 [CrossRef Medline](#)
11. Gresset, A., Sondek, J., and Harden, T. K. (2012) The phospholipase C isozymes and their regulation. *Subcell. Biochem.* **58**, 61–94 [CrossRef Medline](#)
12. Waldo, G. L., Ricks, T. K., Hicks, S. N., Cheever, M. L., Kawano, T., Tsuboi, K., Wang, X., Montell, C., Kozasa, T., Sondek, J., and Harden, T. K. (2010) Kinetic scaffolding mediated by a phospholipase  $C-\beta$  and  $G_q$  signaling complex. *Science* **330**, 974–980 [CrossRef Medline](#)
13. Lyon, A. M., Dutta, S., Boguth, C. A., Skiniotis, G., and Tesmer, J. J. (2013) Full-length  $G\alpha_q$ -phospholipase  $C-\beta 3$  structure reveals interfaces of the C-terminal coiled-coil domain. *Nat. Struct. Mol. Biol.* **20**, 355–362 [CrossRef Medline](#)
14. Lyon, A. M., Tesmer, V. M., Dhamsania, V. D., Thal, D. M., Gutierrez, J., Chowdhury, S., Suddala, K. C., Northup, J. K., and Tesmer, J. J. (2011) An autoinhibitory helix in the C-terminal region of phospholipase  $C-\beta$  mediates  $G\alpha_q$  activation. *Nat. Struct. Mol. Biol.* **18**, 999–1005 [CrossRef Medline](#)
15. Park, D., Jhon, D. Y., Lee, C. W., Ryu, S. H., and Rhee, S. G. (1993) Removal of the carboxyl-terminal region of phospholipase  $C-\beta 1$  by calpain abolishes activation by  $G\alpha_q$ . *J. Biol. Chem.* **268**, 3710–3714 [Medline](#)
16. Kim, C. G., Park, D., and Rhee, S. G. (1996) The role of carboxyl-terminal basic amino acids in  $G_q$ -dependent activation, particulate association, and nuclear localization of phospholipase  $C-\beta 1$ . *J. Biol. Chem.* **271**, 21187–21192 [CrossRef Medline](#)
17. Ilkaeva, O., Kinch, L. N., Paulsen, R. H., and Ross, E. M. (2002) Mutations in the carboxyl-terminal domain of phospholipase  $C\beta 1$  delineate the dimer interface and a potential  $G\alpha_q$  interaction site. *J. Biol. Chem.* **277**, 4294–4300 [CrossRef Medline](#)
18. Singer, A. U., Waldo, G. L., Harden, T. K., and Sondek, J. (2002) A unique fold of phospholipase  $C-\beta$  mediates dimerization and interaction with  $G\alpha_q$ . *Nat. Struct. Mol. Biol.* **9**, 32–36 [CrossRef Medline](#)
19. Jin, T. G., Satoh, T., Liao, Y., Song, C., Gao, X., Kariya, K., Hu, C. D., and Kataoka, T. (2001) Role of the CDC25 homology domain of phospholipase  $C\epsilon$  in amplification of Rap1-dependent signaling. *J. Biol. Chem.* **276**, 30301–30307 [CrossRef Medline](#)
20. Kelley, G. G., Reks, S. E., Ondrako, J. M., and Smrcka, A. V. (2001) Phospholipase  $C\epsilon$ : a novel Ras effector. *EMBO J.* **20**, 743–754 [CrossRef Medline](#)
21. Kelley, G. G., Reks, S. E., and Smrcka, A. V. (2004) Hormonal regulation of phospholipase  $C\epsilon$  through distinct and overlapping pathways involving  $G_{12}$  and Ras family G-proteins. *Biochem. J.* **378**, 129–139 [CrossRef Medline](#)
22. Hicks, S. N., Jezyk, M. R., Gershburg, S., Seifert, J. P., Harden, T. K., and Sondek, J. (2008) General and versatile autoinhibition of PLC isozymes. *Mol. Cell* **31**, 383–394 [CrossRef Medline](#)
23. Jezyk, M. R., Snyder, J. T., Gershberg, S., Worthyake, D. K., Harden, T. K., and Sondek, J. (2006) Crystal structure of Rac1 bound to its effector phospholipase  $C-\beta 2$ . *Nat. Struct. Mol. Biol.* **13**, 1135–1140 [CrossRef Medline](#)
24. Lyon, A. M., Begley, J. A., Manett, T. D., and Tesmer, J. J. (2014) Molecular Mechanisms of phospholipase  $C\beta 3$  autoinhibition. *Structure* **22**, 1844–1854 [CrossRef Medline](#)
25. Zhang, W., and Neer, E. J. (2001) Reassembly of phospholipase  $C-\beta 2$  from separated domains: analysis of basal and G protein-stimulated activities. *J. Biol. Chem.* **276**, 2503–2508 [CrossRef Medline](#)
26. Kadampur, G., and Ross, E. M. (2016) Intrinsic pleckstrin homology (PH) domain motion in phospholipase  $C-\beta$  exposes a  $G\beta\gamma$  protein binding site. *J. Biol. Chem.* **291**, 11394–11406 [CrossRef Medline](#)
27. Drin, G., Douguet, D., and Scarlata, S. (2006) The pleckstrin homology domain of phospholipase  $C\beta$  transmits enzymatic activation through modulation of the membrane-domain orientation. *Biochemistry* **45**, 5712–5724 [CrossRef Medline](#)
28. Han, D. S., Golebiewska, U., Stolzenberg, S., Scarlata, S. F., and Weinstein, H. (2011) A dynamic model of membrane-bound phospholipase  $C\beta 2$  activation by  $G\beta\gamma$  subunits. *Mol. Pharmacol.* **80**, 434–445 [CrossRef Medline](#)
29. Garcia, P., Gupta, R., Shah, S., Morris, A. J., Rudge, S. A., Scarlata, S., Petrova, V., McLaughlin, S., and Rebecchi, M. J. (1995) The pleckstrin homology domain of phospholipase  $C-\delta 1$  binds with high affinity to phosphatidylinositol 4,5-bisphosphate in bilayer membranes. *Biochemistry* **34**, 16228–16234 [CrossRef Medline](#)
30. Cifuentes, M. E., Honkanen, L., and Rebecchi, M. J. (1993) Proteolytic fragments of phosphoinositide-specific phospholipase  $C-\delta 1$ : catalytic and membrane binding properties. *J. Biol. Chem.* **268**, 11586–11593 [Medline](#)
31. Essen, L. O., Perisic, O., Cheung, R., Katan, M., and Williams, R. L. (1996) Crystal structure of a mammalian phosphoinositide-specific phospholipase  $C\delta$ . *Nature* **380**, 595–602 [CrossRef Medline](#)
32. Oestreich, E. A., Malik, S., Goonasekera, S. A., Blaxall, B. C., Kelley, G. G., Dirksen, R. T., and Smrcka, A. V. (2009) Epac and phospholipase  $C\epsilon$  regulate  $Ca^{2+}$  release in the heart by activation of protein kinase  $C\epsilon$  and calcium-calmodulin kinase II. *J. Biol. Chem.* **284**, 1514–1522 [CrossRef Medline](#)
33. Oestreich, E. A., Wang, H., Malik, S., Kaproth-Joslin, K. A., Blaxall, B. C., Kelley, G. G., Dirksen, R. T., and Smrcka, A. V. (2007) Epac-mediated activation of phospholipase  $C\epsilon$  plays a critical role in  $\beta$ -adrenergic receptor-dependent enhancement of  $Ca^{2+}$  mobilization in cardiac myocytes. *J. Biol. Chem.* **282**, 5488–5495 [CrossRef Medline](#)
34. Dusaban, S. S., Purcell, N. H., Rockenstein, E., Maslah, E., Cho, M. K., Smrcka, A. V., and Brown, J. H. (2013) Phospholipase  $C\epsilon$  links G protein-coupled receptor activation to inflammatory astrocytic responses. *Proc. Natl. Acad. Sci. U.S.A.* **110**, 3609–3614 [CrossRef Medline](#)
35. Bunney, T. D., Harris, R., Gandarillas, N. L., Josephs, M. B., Roe, S. M., Sorli, S. C., Paterson, H. F., Rodrigues-Lima, F., Esposito, D., Ponting, C. P., Gierschik, P., Pearl, L. H., Driscoll, P. C., and Katan, M. (2006) Structural and mechanistic insights into ras association domains of phospholipase  $C\epsilon$ . *Mol. Cell.* **21**, 495–507 [CrossRef Medline](#)
36. Seifert, J. P., Wing, M. R., Snyder, J. T., Gershburg, S., Sondek, J., and Harden, T. K. (2004) RhoA activates purified phospholipase  $C-\epsilon$  by a guanine nucleotide-dependent mechanism. *J. Biol. Chem.* **279**, 47992–47997 [CrossRef Medline](#)
37. Seifert, J. P., Zhou, Y., Hicks, S. N., Sondek, J., and Harden, T. K. (2008) Dual activation of phospholipase  $C-\epsilon$  by Rho and Ras GTPases. *J. Biol. Chem.* **283**, 29690–29698 [CrossRef Medline](#)
38. Ghosh, M., and Smrcka, A. V. (2004) Assay for G protein-dependent activation of phospholipase  $C\beta$  using purified protein components. *Methods Mol. Biol.* **237**, 67–75 [Medline](#)
39. Seifert, J. P., Snyder, J. T., Sondek, J., and Harden, T. K. (2006) Direct activation of purified phospholipase  $C\epsilon$  by RhoA studied in reconstituted phospholipid vesicles. *Methods Enzymol.* **406**, 260–271 [CrossRef Medline](#)

## Conformational dynamics of PLC enzymes

40. Mezzasalma, T. M., Kranz, J. K., Chan, W., Struble, G. T., Schalk-Hihi, C., Deckman, I. C., Springer, B. A., and Todd, M. J. (2007) Enhancing recombinant protein quality and yield by protein stability profiling. *J. Biomol. Screen* **12**, 418–428 [CrossRef Medline](#)
41. Glukhova, A., Hinkovska-Galcheva, V., Kelly, R., Abe, A., Shayman, J. A., and Tesmer, J. J. (2015) Structure and function of lysosomal phospholipase A2 and lecithin:cholesterol acyltransferase. *Nat. Commun.* **6**, 6250 [CrossRef Medline](#)
42. Skou, S., Gillilan, R. E., and Ando, N. (2014) Synchrotron-based small-angle X-ray scattering of proteins in solution. *Nat. Protoc.* **9**, 1727–1739 [CrossRef Medline](#)
43. Korasick, D. A., and Tanner, J. J. (2018) Determination of protein oligomeric structure from small-angle X-ray scattering. *Protein Sci.* **27**, 814–824 [CrossRef Medline](#)
44. Mylonas, E., and Svergun, D. I. (2007) Accuracy of molecular mass determination of proteins by small-angle X-ray scattering. *J. Appl. Crystallogr.* **40**, s245–s249 [CrossRef](#)
45. Pettersen, E. F., Goddard, T. D., Huang, C. C., Couch, G. S., Greenblatt, D. M., Meng, E. C., and Ferrin, T. E. (2004) UCSF Chimera—a visualization system for exploratory research and analysis. *J. Comput. Chem.* **25**, 1605–1612 [CrossRef Medline](#)
46. Trewthella, J., Duff, A. P., Durand, D., Gabel, F., Guss, J. M., Hendrickson, W. A., Hura, G. L., Jacques, D. A., Kirby, N. M., Kwan, A. H., Perez, J., Pollack, L., Ryan, T. M., Sali, A., Schneidman-Duhovny, D., et al. (2017) 2017 publication guidelines for structural modelling of small-angle scattering data from biomolecules in solution: an update. *Acta Crystallogr. D Struct. Biol.* **73**, 710–728 [CrossRef Medline](#)
47. Ohi, M., Li, Y., Cheng, Y., and Walz, T. (2004) Negative staining and image classification: powerful tools in modern electron microscopy. *Biol. Proced. Online* **6**, 23–34 [CrossRef Medline](#)
48. Harden, T. K., Hicks, S. N., and Sondek, J. (2009) Phospholipase C isozymes as effectors of Ras superfamily GTPases. *J. Lipid Res.* **50**, S243–S248 [CrossRef Medline](#)
49. Camps, M., Hou, C., Sidiropoulos, D., Stock, J. B., Jakobs, K. H., and Gierschik, P. (1992) Stimulation of phospholipase C by guanine-nucleotide-binding protein  $\beta\gamma$  subunits. *Eur. J. Biochem.* **206**, 821–831 [CrossRef Medline](#)
50. Smrcka, A. V., and Sternweis, P. C. (1993) Regulation of purified subtypes of phosphatidylinositol-specific phospholipase C $\beta$  by G protein  $\alpha$  and  $\beta\gamma$  subunits. *J. Biol. Chem.* **268**, 9667–9674 [Medline](#)
51. Feng, J., Roberts, M. F., Drin, G., and Scarlata, S. (2005) Dissection of the steps of phospholipase C $\beta$  2 activity that are enhanced by G $\beta\gamma$  subunits. *Biochemistry* **44**, 2577–2584 [CrossRef Medline](#)
52. Guo, Y., Philip, F., and Scarlata, S. (2003) The pleckstrin homology domains of phospholipases C- $\beta$  and - $\delta$  confer activation through a common site. *J. Biol. Chem.* **278**, 29995–30004 [CrossRef Medline](#)
53. Runnels, L. W., Jenco, J., Morris, A., and Scarlata, S. (1996) Membrane binding of phospholipases C- $\beta$ 1 and C- $\beta$ 2 is independent of phosphatidylinositol 4,5-bisphosphate and the  $\alpha$  and  $\beta\gamma$  subunits of G proteins. *Biochemistry* **35**, 16824–16832 [CrossRef Medline](#)
54. Hudson, B. N., Hyun, S. H., Thompson, D. H., and Lyon, A. M. (2017) Phospholipase C $\beta$ 3 membrane adsorption and activation are regulated by its C-terminal domains and phosphatidylinositol 4,5-bisphosphate. *Biochemistry* **56**, 5604–5614 [CrossRef Medline](#)
55. Hopkins, J. B., Gillilan, R. E., and Skou, S. (2017) BioXTAS RAW: improvements to a free open-source program for small-angle X-ray scattering data reduction and analysis. *J. Appl. Crystallogr.* **50**, 1545–1553 [CrossRef Medline](#)
56. Franke, D., Petoukhov, M. V., Konarev, P. V., Panjkovich, A., Tuukkanen, A., Mertens, H. D. T., Kikhney, A. G., Hajizadeh, N. R., Franklin, J. M., Jeffries, C. M., and Svergun, D. I. (2017) ATSAS 2.8: a comprehensive data analysis suite for small-angle scattering from macromolecular solutions. *J. Appl. Crystallogr.* **50**, 1212–1225 [CrossRef Medline](#)
57. Konarev, P. V., Volkov, V. V., Sokolova, A. V., Koch, M. H. J., and Svergun, D. I. (2003) PRIMUS: a Windows PC-based system for small-angle scattering data analysis. *J. Appl. Crystallogr.* **36**, 1277–1282 [CrossRef](#)
58. Volkov, V. V., and Svergun, D. I. (2003) Uniqueness of *ab initio* shape determination in small-angle scattering. *J. Appl. Crystallogr.* **36**, 860–864 [CrossRef](#)
59. Svergun, D. I. (1999) Restoring low resolution structure of biological macromolecules from solution scattering using simulated annealing. *Biophys. J.* **76**, 2879. Correction (1999) *Biophys. J.* **77**, 2896 [CrossRef](#) [CrossRef Medline](#)
60. Svergun, D., Barberato, C., and Koch, M. H. J. (1995) CRY SOL: a program to evaluate x-ray solution scattering of biological macromolecules from atomic coordinates. *J. Appl. Crystallogr.* **28**, 768–773 [CrossRef](#)
61. Petoukhov, M. V., and Svergun, D. I. (2005) Global rigid body modeling of macromolecular complexes against small-angle scattering data. *Biophys. J.* **89**, 1237–1250 [CrossRef Medline](#)
62. Kimanius, D., Forsberg, B. O., Scheres, S. H., and Lindahl, E. (2016) Accelerated cryo-EM structure determination with parallelisation using GPUs in RELION-2. *Elife* **5**, e18722 [CrossRef Medline](#)
63. Scheres, S. H. (2016) Processing of structurally heterogeneous cryo-EM data in RELION. *Methods Enzymol.* **579**, 125–157 [CrossRef Medline](#)
64. Tang, G., Peng, L., Baldwin, P. R., Mann, D. S., Jiang, W., Rees, I., and Ludtke, S. J. (2007) EMAN2: an extensible image processing suite for electron microscopy. *J. Struct. Biol.* **157**, 38–46 [CrossRef Medline](#)
65. Svergun, D. I. (1992) Determination of the regularization parameter in indirect-transform methods using perceptual criteria. *J. Appl. Crystallogr.* **25**, 495–503 [CrossRef](#)

**Direct observation of conformational dynamics of the PH domain in phospholipases C? and may contribute to subfamily-specific roles in regulation**

Elisabeth E. Garland-Kuntz, Frank S. Vago, Monita Sieng, Michelle Van Camp, Srinivas Chakravarthy, Arryn Blaine, Clairissa Corpstein, Wen Jiang and Angeline M. Lyon

*J. Biol. Chem.* 2018, 293:17477-17490.

doi: 10.1074/jbc.RA118.003656 originally published online September 21, 2018

---

Access the most updated version of this article at doi: [10.1074/jbc.RA118.003656](https://doi.org/10.1074/jbc.RA118.003656)

Alerts:

- [When this article is cited](#)
- [When a correction for this article is posted](#)

[Click here](#) to choose from all of JBC's e-mail alerts

This article cites 65 references, 23 of which can be accessed free at <http://www.jbc.org/content/293/45/17477.full.html#ref-list-1>

**Supporting Information for**

Direct observation of conformational dynamics of the PH domain in phospholipases C $\epsilon$  and  $\beta$  may contribute to subfamily-specific roles in regulation

**Elisabeth E. Garland-Kuntz<sup>1</sup>, Frank S. Vago<sup>2</sup>, Monita Sieng<sup>1</sup>, Michelle Van Camp<sup>1</sup>,  
Srinivas Chakravarthy<sup>3</sup>, Arryn Blaine<sup>1</sup>, Clairissa Corpstein<sup>1</sup>, Wen Jiang<sup>2</sup>, and Angeline M.  
Lyon<sup>1,2\*</sup>**

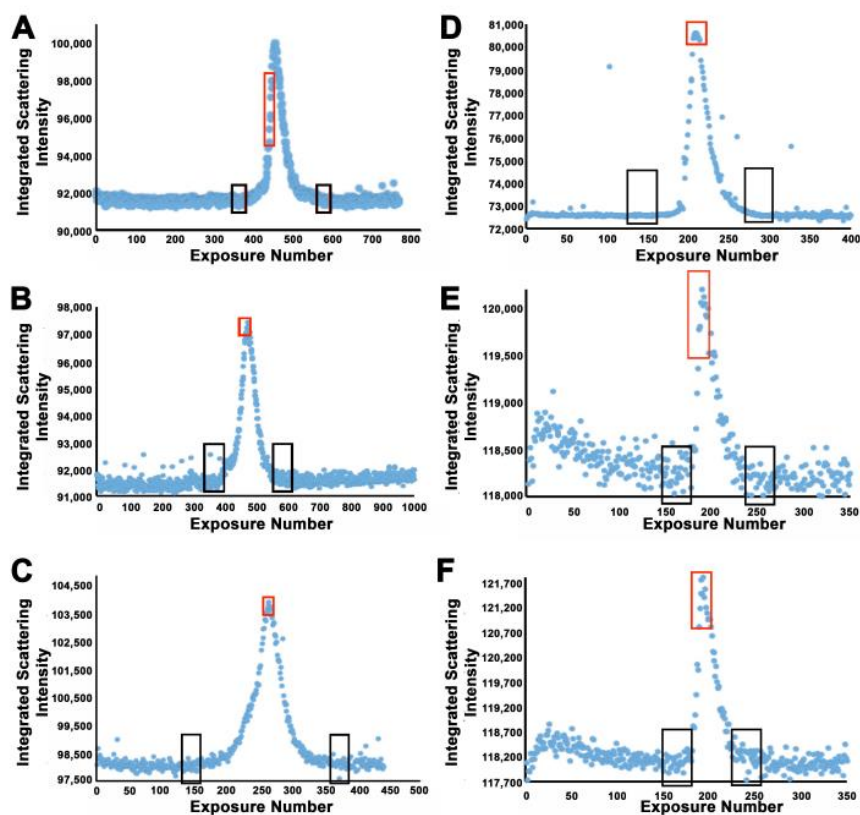
From the <sup>1</sup>Department of Chemistry, Purdue University, West Lafayette, IN 47907 <sup>2</sup>Department of Biological Sciences, Purdue University, West Lafayette, IN 47907 <sup>3</sup>Biophysics Collaborative Access Team, Illinois Institute of Technology, Sector 18ID, Advanced Photon Source, Argonne National Laboratory, Lemont, IL 60439

Running title: *Conformational dynamics of PLC enzymes*

\*To whom correspondence should be addressed: Angeline M. Lyon, Departments of Chemistry and Biological Sciences, Purdue University, 560 Oval Drive, West Lafayette, Indiana 47907, Telephone: (765)-494-5291; email: lyonam@purdue.edu

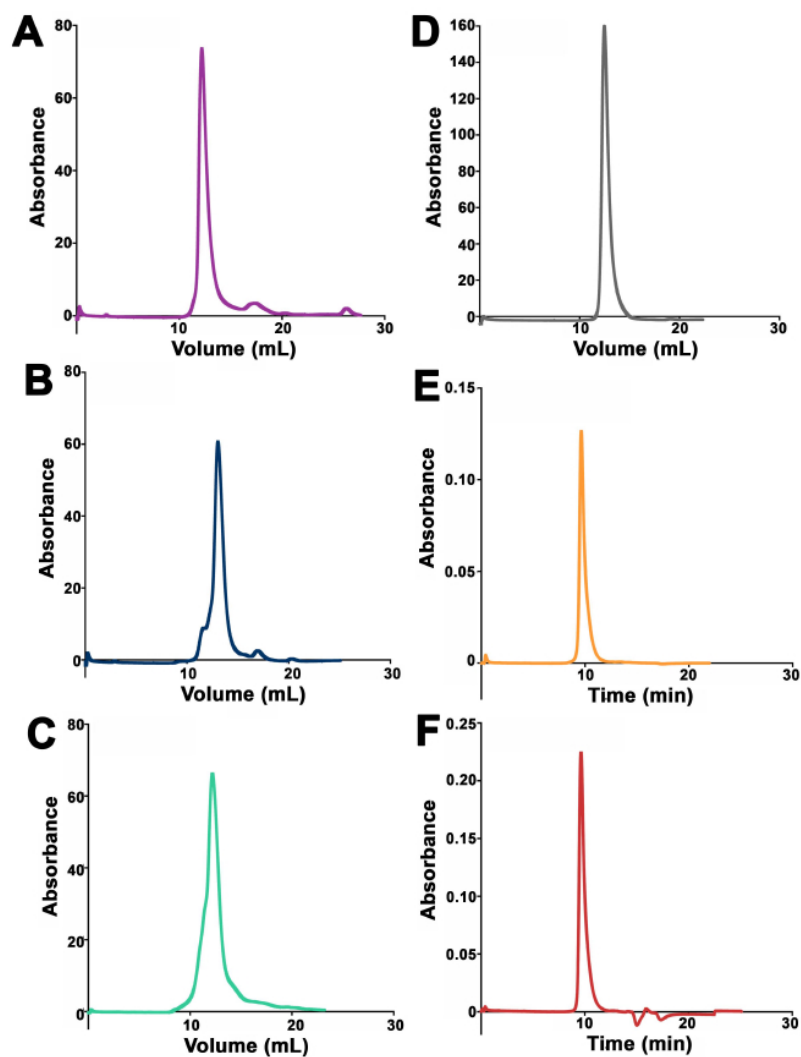
**Supporting Table 1. SAXS structural parameters of PLC $\beta$ 3- $\Delta$ 892 E60C/V164C treated with 15 mM excess BMOE.**

PLC $\beta$ 3- $\Delta$ 892 E60C/V164C +15 mM excess BMOE	
<i>Guinier analysis</i>	
$I(0)$ (cm $^{-1}$ )	25.57 $\pm$ 0.30
$R_g$ (Å)	34.8 $\pm$ 1.54
$q$ min (Å $^{-1}$ )	0.0109
$q$ range (Å $^{-1}$ )	0.0109-0.0369
<i>P(r) analysis</i>	
$I(0)$ (cm $^{-1}$ )	23.57
$R_g$ (Å)	35.37
$D_{max}$ (Å)	120
Porod volume (Å $^{-3}$ )	153,000
$q$ range (Å $^{-1}$ )	0.0109-0.230



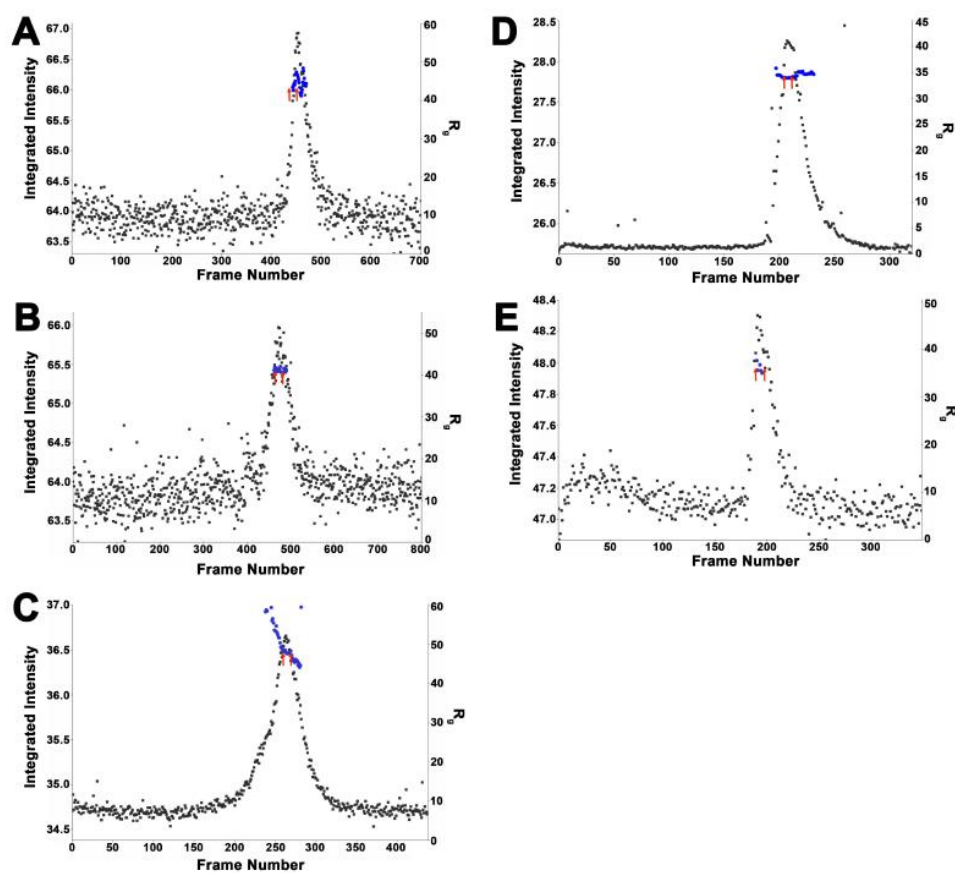
**Supporting Figure 1. Size exclusion chromatography (SEC)-SAXS scattering**

**chromatograms for PLC $\epsilon$  and PLC $\beta$ 3- $\Delta$ 892 variants.** Each chromatogram shows the integrated scattering intensity as a function of exposure number for all PLC variants characterized in this study. Regions boxed in red correspond to data used for SAXS analysis, regions boxed in black were averaged and used for the buffer blanks. (A) PLC $\epsilon$  PH-COOH, (B) PLC $\epsilon$  PH-C2, (C) PLC $\epsilon$  EF-COOH, (D) PLC $\beta$ 3- $\Delta$ 892, (E) oxidized PLC $\beta$ 3- $\Delta$ 892 E60C/V164C oxidized, and (F) reduced PLC $\beta$ 3- $\Delta$ 892 E60C/V164C.

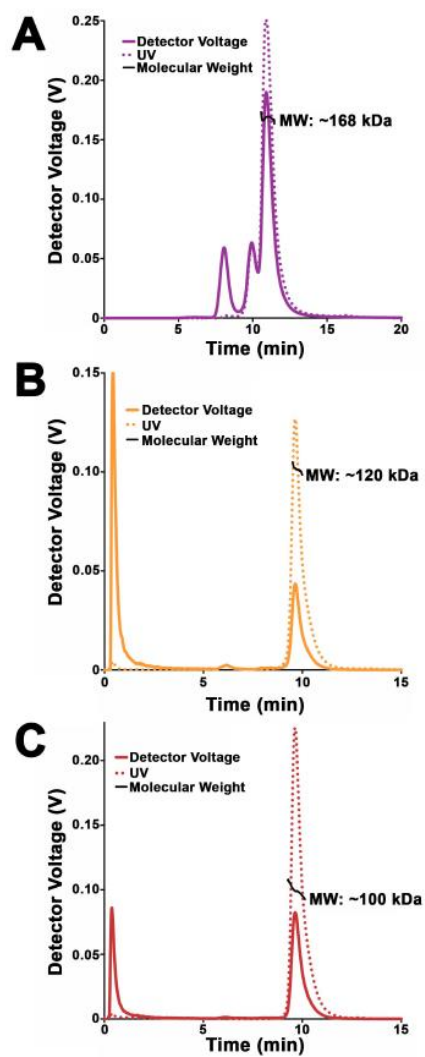


**Supporting Figure 2. Representative UV chromatograms for PLC $\epsilon$  and PLC $\beta$ 3- $\Delta$ 892 variants.** (A) PLC $\epsilon$  PH-COOH, (B) PLC $\epsilon$  PH-C2, (C) PLC $\epsilon$  EF-COOH, and (D) PLC $\beta$ 3- $\Delta$ 892 UV chromatograms were obtained from SEC-SAXS experiments, while (E) oxidized PLC $\beta$ 3-

$\Delta 892$  E60C/V164C oxidized and (F) reduced PLC $\beta$ 3- $\Delta 892$  E60C/V164C UV chromatograms were obtained during SEC-MALS-SAXS experiments.

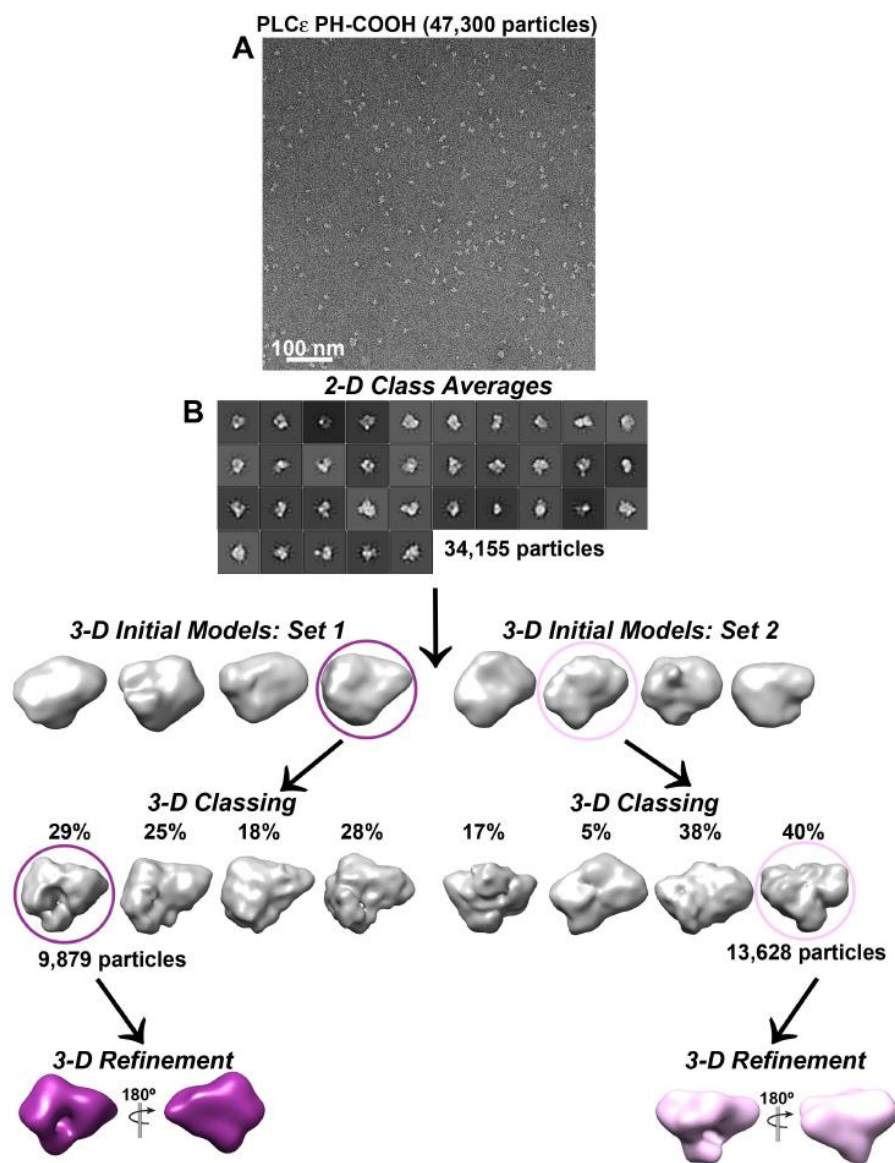


**Supporting Figure 3. Integrated scattering intensity and  $R_g$  values.** The integrated scattering intensity and  $R_g$  as a function of individual frames is shown for (A) PLC $\epsilon$  PH-COOH, (B) PLC $\epsilon$  PH-C2, (C) PLC $\epsilon$  EF-COOH, (D) PLC $\beta$ 3- $\Delta$ 892, and (E) reduced PLC $\beta$ 3- $\Delta$ 892 E60C/V164C. Red lines correspond to the frames used in the data analysis. Oxidized PLC $\beta$ 3- $\Delta$ 892 E60C/V164C is not shown, as the signal to noise for this sample required averaging frames for the Guinier approximation and calculation of the  $R_g$ .



Supporting Figure 4. Multi-angle light scattering (MALS) confirms the molecular weights of PLC $\epsilon$  PH-COOH, oxidized PLC $\beta$ 3- $\Delta$ 892 E60C/V164C, and reduced PLC $\beta$ 3- $\Delta$ 892 E60C/V164C. SEC-MALS was used to validate the molecular weight and monodispersity of (A) PLC $\epsilon$  PH-COOH in solution. SEC-MALS-SAXS was used to confirm the molecular weights and

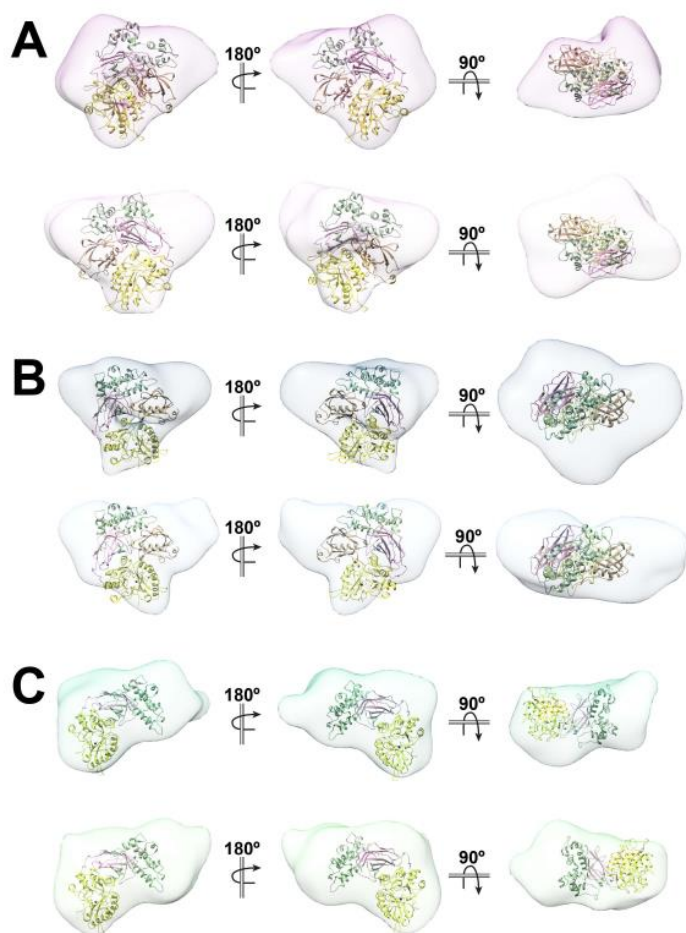
monodispersity of (B) oxidized PLC $\beta$ 3- $\Delta$ 892 E60C/V164C, and (C) reduced PLC $\beta$ 3- $\Delta$ 892 E60C/V164C.



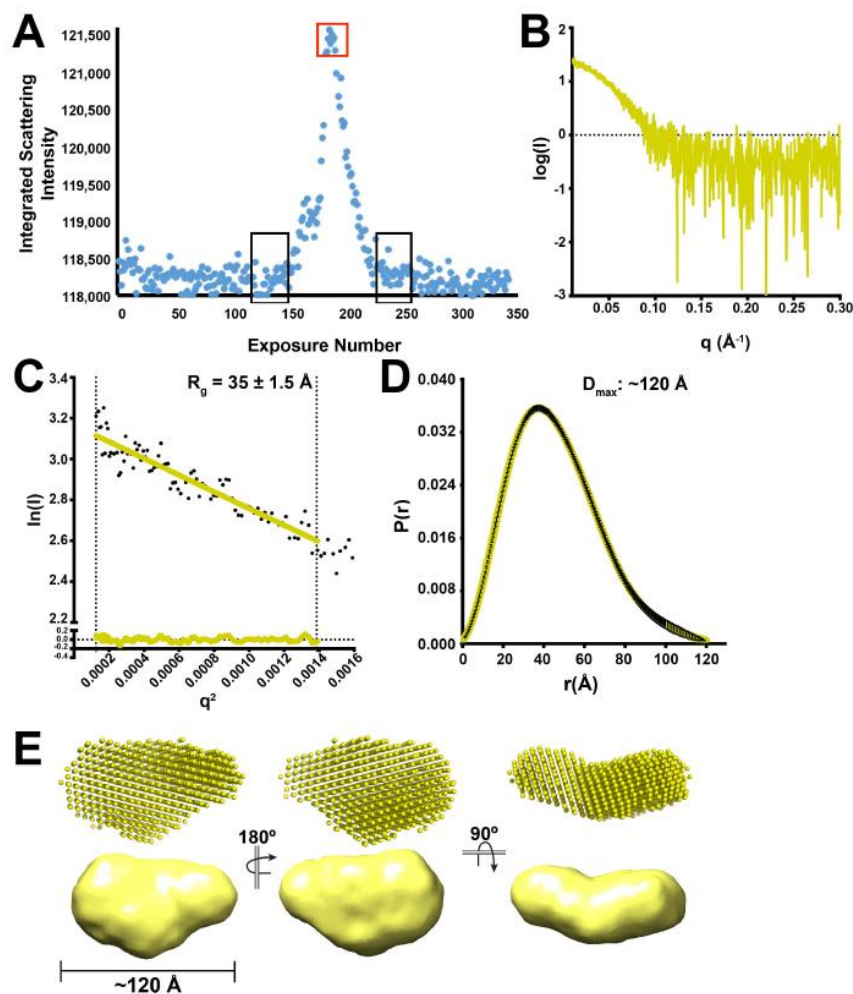
Supporting Figure 5. Example RELION-2.1 workflow for PLC $\epsilon$  PH-COOH

reconstruction. (A) Representative, unadjusted micrograph showing a field view of uranyl formate-stained particles. (B) RELION-2.1 workflow, starting with selected classes from

reference-free 2-D classification. To validate *de novo* initial models, two sets of particles containing ~100 particles per 2-D class were separately selected and used to generate each set of 3-D initial models. One model was chosen at random and subjected to 3-D classification. Due to apparent conformational heterogeneity of the particles on the grid, 3-D class distributions did not result in a distinct dominant class in most cases for all PLC $\epsilon$  variants in this study (e.g., 29%, 25%, and 28%), but 3-D refinement was performed with the most dominant class whenever possible. Panels A, B, and the final 3-D reconstructions are also shown in Figure 3 in the main text.



**Supporting Figure 6. Fitted 3-D EM reconstructions of PLC $\epsilon$ .** Two reconstructions of (A) PLC $\epsilon$  PH-COOH, (B) PLC $\epsilon$  PH-C2, and (C) PLC $\epsilon$  EF-COOH with the PLC $\beta$ 3 core crystal structure fit as a reference (colored as in Fig. 1A and including the PH-C2 domains from PDB ID 3OHH (12)). In the PH-COOH and EF-COOH reconstructions, the C-terminus of the C2 domain is oriented towards the additional density observed in these envelopes relative to PH-C2, which likely corresponds to the RA domains. For the EF-COOH reconstructions, the PLC $\beta$ 3 core structure fit in the density lacks the PH domain.



**Supporting Figure 7. Crosslinking of reduced PLC $\beta$ 3- $\Delta$ 892 E60C/V164C restricts motion of the PH domain.** Reduced PLC $\beta$ 3- $\Delta$ 892 E60C/V164C was incubated with 15 mM excess bismaleimidoethane (BMOE) to crosslink the PH domain and EF1/2. (A) SEC-SAXS chromatogram of integrated scattering intensity versus exposure number. Regions boxed in red correspond to exposures used in SAXS analysis, and regions boxed in black were averaged for

the buffer blank. (B) Raw scattering curve, (C) Guinier analyses of low  $q$  values,  $\ln(I)$  (beam intensity) vs.  $q^2$  (scattering angle) with radius of gyration ( $R_g$ ), and (D) Pair-distance distribution function of the BMOE-treated PLC $\beta$ 3- $\Delta$ 892 E60C/V164C. (E) *Ab initio* envelope models (top) and equivalent envelopes rendered as volumes (bottom). The envelopes are most consistent with the oxidized PLC $\beta$ 3-D892 E60C/V164C variant, suggesting that crosslinking is sufficient to restrict the motion of the PH domain.